Conceptual design of a breed & burn molten salt reactor

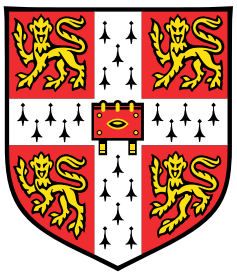

Alisha Ana Kasam

Supervisor: Dr Eugene Shwageraus

Department of Engineering
University of Cambridge

This dissertation is submitted for the degree of
Doctor of Philosophy

Churchill College November 2018

Declaration

This dissertation is the result of my own work and includes nothing which is the outcome of work done in collaboration except as specified in the text. It is not substantially the same as any that I have submitted, or, is being concurrently submitted for a degree or diploma or other qualification at the University of Cambridge or any other University or similar institution. I further state that no substantial part of my dissertation has already been submitted, or, is being concurrently submitted for any such degree, diploma or other qualification at the University of Cambridge or any other University or similar institution. This dissertation contains fewer than 65,000 words including appendices, bibliography, footnotes, tables and equations and has fewer than 150 figures.

Alisha Ana Kasam
November 2018

Acknowledgements

I am extremely grateful to my supervisor, Dr Eugene Shwageraus, who has been an incredible source of knowledge, enthusiasm, and patient guidance. Many thanks also to Professor Jeong Ik Lee of KAIST, who became like a co-supervisor to me during his time in Cambridge. He has been very generous with his time and expertise, and many sections of this thesis resulted from long and fruitful conversations with him.

Mr Tony Roulstone, Professor Epominondas Mastorakos, and Professor Stewart Cant have provided invaluable advice, teaching, and support during my graduate studies at Cambridge. I gratefully acknowledge Dr Ian Scott of Moltex Energy for his support of my research topic and advice on molten salt reactor chemistry. I am also thankful to Dr Andrea Giusti and Xinyu Zhao for their help with OpenFOAM.

I thank Professor Dan Kotlyar, now of Georgia Tech, and Dr Ben Lindley of Wood Group for their friendship and advice on many topics. Each of my colleagues in BS3-05 has been a source of help or camaraderie during my PhD, and the kind and wonderful Joanne Boyle is the glue holding all of us together.

Looking back to my undergraduate years at Georgia Tech, I cannot adequately express my thanks to Professor Chris Paredis and Dr Karen Adams for teaching me the confidence and skills that carried me all the way to Cambridge and eventually to the end of a PhD.

Thank you to my family for encouraging, challenging, and supporting me throughout my life and education. Special thanks also to my in-laws for being on my team from day one and welcoming me into their lovely family. My amazing husband and best friend, Kent, deserves an award for cheerfully supporting me throughout the many highs and lows of my PhD. Above all, I thank him for always seeing the best in me.

I gratefully acknowledge financial support from the Winston Churchill Foundation of the United States, Cambridge International Trust, and Churchill Pochobradsky Scholarship.

Abstract

A breed-and-burn molten salt reactor (BBMSR) concept is proposed to address the Generation IV fuel cycle sustainability objective in a once-through cycle with low enrichment and no reprocessing. The BBMSR uses separate fuel and coolant molten salts, with the fuel contained in assemblies of individual tubes that can be shuffled and reclad periodically to enable high burnup. In this dual-salt configuration, the BBMSR may overcome several limitations of previous breed-and-burn (B&B) designs to achieve high uranium utilisation with a simple, passively safe design.

A central challenge in design of the BBMSR fuel is balancing the neutronic requirement of large fuel volume fraction for B&B mode with the thermal–hydraulic requirements for safe and economically competitive reactor operation. Natural convection of liquid fuel within the tubes aids heat transfer to the coolant, and a systematic approach is developed to efficiently model this complex effect. Computational fluid dynamics modelling is performed to characterise the unique physics of the system and produce a new heat transfer correlation, which is used alongside established correlations in a numerical model. A design framework is built around this numerical model to iteratively search for the limiting power density of a given fuel and channel geometry, applying several defined temperature and operational constraints. It is found that the trade-offs between power density, core pressure drop, and pumping power are lessened by directing the flow of coolant downwards through the channel.

Fuel configurations that satisfy both neutronic and thermal–hydraulic objectives are identified for natural, 5% enriched, and 20% enriched uranium feed fuel. B&B operation is achievable in the natural and 5% enriched versions, with power densities of 73 W/cm^3 and 86 W/cm^3, and theoretical uranium utilisations of 300 MWd/kgU$_{\mathrm{NAT}}$ and 25.5 MWd/kgU$_{\mathrm{NAT}}$, respectively. Using 20% enriched feed fuel relaxes neutronic constraints so a wider range of fuel configurations can be considered, but there is a strong inverse correlation between power density and uranium utilisation. The fuel design study demonstrates the flexibility of the BBMSR concept to operate along a spectrum of modes ranging from high fuel utilisation at moderate power density using natural uranium feed fuel, to high power density and moderate utilisation using 20% uranium enrichment.

Table of contents

List of figures

List of tables

Nomenclature

Roman Symbols

A	Area
B	Discharge burnup
c_P	Specific heat capacity
D	Hydraulic diameter
d	Hydraulic diameter of section
dz	Node height
f	Friction factor
g	Acceleration due to gravity
Gr	Grashof number
h	Heat transfer coefficient
k_{eff}	Effective multiplication factor
k_∞	Infinite multiplication factor
L	Length
L_e	Extrapolation length
$\dot{m}$	Mass flow rate
mol%	Mole percent
N	Number of nodes

Nu	Nusselt number
p	Pressure
P/D	Pitch-to-diameter ratio
Pr	Prandtl number
q	Energy
q''	Heat flux
q'''	Volumetric heat generation rate
r	Radius
R	Thermal resistance
Re	Reynolds number
T	Temperature
u	x-velocity
U	Uranium utilisation
V	Node volume
v	y-velocity
x	Distance from vertical axis of parallel channel
y	Distance from lower end of parallel channel
z	Distance from lower end of cylinder

Greek Symbols

α	Thermal diffusivity
β	Volumetric coefficient of thermal expansion
ε	Concentric fuel geometry ratio
η	Reproduction factor

κ	Thermal conductivity
μ	Dynamic viscosity
ν	Kinematic viscosity
Ω	IHG-flux number
ρ	Density
Σ_c	Macroscopic capture cross-section
Σ_f	Macroscopic fission cross-section

Subscripts

0	Property at the reference temperature
A	Section A
B	Section B
ci	Cladding inner surface
f	Frictional
g	Gravitational
i	Node index
in	Inlet
m	Bulk
out	Outlet
w	Inner wall

Acronyms / Abbreviations

ARE	Aircraft Reactor Experiment
B&B	Breed-and-Burn
BBMSR	Breed-and-Burn Molten Salt Reactor

BBSFR Breed-and-Burn Sodium Fast Reactor

CFD Computational Fluid Dynamics

DMSR Denatured Molten Salt Reactor

DNP Delayed Neutron Precursor

DPA Displacements Per Atom

FDM Finite-Difference Model

FHR Fluoride salt-cooled High-temperature Reactor

FIMA Fission per Initial heavy-Metal Atom

GFR Gas-cooled Fast Reactor

GIF Generation IV International Forum

IHG Internal Heat Generation

LEU Low-Enriched Uranium

LFR Lead-cooled Fast Reactor

LRM Linear Reactivity Model

LWR Light Water Reactor

MCFBR Molten-Chloride Fast-Breeder Reactor

MCFR Molten Chloride Fast Reactor

MHT Mixed Heat Transfer

MOX Mixed Oxide

MSBR Molten Salt Breeder Reactor

MSFR Molten Salt Fast Reactor

MSR Molten Salt Reactor

MSRE Molten Salt Reactor Experiment

SFR Sodium-cooled Fast Reactor

SNF Spent Nuclear Fuel

SS310 Stainless Steel type 310

SSR Stable Salt Reactor

TRISO Tri-Structural Isotropic

TRU Transuranics

TWR Traveling-Wave Reactor

USFR Uranium-Start-up Fast Reactor

Chapter 1

Introduction

The existing global nuclear framework is dominated by light water reactors (LWRs) using a once-through open fuel cycle. In the once-through LWR fuel cycle, less than 1% of mined uranium is fissioned, while the remainder is lost in the enrichment process or disposed of as spent fuel [35]. Since spent LWR fuel has a high residual energy content, a small number of LWRs are operated in a partially closed fuel cycle, with reprocessing limited to once-through plutonium recycling as mixed oxide (MOX) fuel. MOX fabrication is estimated to cost $1700 to $3700 more per kilogram than conventional uranium oxide fuel fabrication, roughly an order of magnitude increase, and results in only about 15% uranium savings [71, 35].

The economic and environmental sustainability of the current nuclear fuel cycle could be considerably improved. The 2014 Red Book publication by the Organisation for Economic Co-operation and Development estimates that total identified uranium reserves are sufficient to power the global nuclear reactor fleet for over 120 years at current use rates [47]. A survey of uranium price elasticity models indicates that the once-through LWR fuel cycle can remain economically competitive at least until the middle of the century [35]. However, given that modern LWRs have an operating lifetime of 60 years or more, development of alternative fuel cycles is already needed to ensure the economic sustainability of nuclear energy into the future. In addition, environmental impacts of the current nuclear fuel cycle include the effects of ore extraction and the generation of waste in each stage of the fuel cycle. Disposal of wastes from enrichment, fabrication, reprocessing, and spent fuel requires costly geological repositories that can ensure security against proliferation and safely contain radioactive isotopes as they decay over hundreds of thousands of years [45]. While strategies for permanent disposal are technologically robust, lack of public acceptance has prevented the siting of such facilities.

The Generation IV International Forum (GIF) has defined sustainability, safety and reliability, economic competitiveness, and proliferation resistance as the four goal areas for the next generation of nuclear energy [46]. Fast reactors operating within a closed fuel cycle address long-term sustainability concerns by improving resource utilisation and reducing waste from spent nuclear fuel; however, fuel reprocessing is opposed in the United States and other countries due to its economic cost and present-day risks, including proliferation concerns. Breed-and-burn (B&B) fast reactors operating with a once-through fuel cycle may be able to realise high fuel utilisation without fuel reprocessing. Further investigations are needed to enable the minimum fuel burnup required to sustain B&B operation without exceeding the radiation damage limits of known cladding materials.

This thesis describes the conceptual design of a breed-and-burn molten salt reactor (BBMSR) using separate fuel and coolant molten salts, which is proposed to overcome several limitations of previous solid-fuelled B&B designs. The BBMSR is a new concept that combines the advantages of B&B and molten salt reactor technologies with an emphasis on the Generation IV objective of improved fuel cycle sustainability.

1.1 Fast Reactors

Four out of six of the official Generation IV technologies selected by GIF are fast reactors that would address the sustainability goal by closing the fuel cycle. In the closed fast reactor fuel cycle, chemical reprocessing and partitioning separates plutonium and other transuranics (TRUs) from spent nuclear fuel (SNF). The recovered TRUs are transmuted in a fast reactor, which reduces the volume, long-term radioactivity and radiotoxicity, and heat generation of the final waste stream, making its disposal less costly and complex.

Fast reactors require an initial supply of fissile fuel for start-up, but since they breed more fissile material than they consume, their SNF can be recycled indefinitely. With the LWR once-through fuel cycle, known uranium reserves can generate a quantity of energy comparable to combustion of known oil reserves; fast breeders can extend this supply to an estimated 40 times more energy than all the world's fossil fuels [34]. SNF recycling has been demonstrated at the laboratory scale and in test reactors, such as Phénix and Superphénix in France. While the closed fuel cycle offers future benefits, the immediate costs and risks of reprocessing must be weighed. Separation of fission products from SNF introduces the potential for proliferation and worker radiation exposure risks. In addition, the high plutonium content and quality in fast reactor SNF makes the plutonium cheaper to recover in reprocessing, which also increases its attractiveness for weapons use [81]. Whereas the

once-through LWR fuel cycle poses long-term sustainability risks, the closed fast reactor fuel cycle shifts some of those risks to the present.

Design of fast reactors involves reactor physics considerations that differ from those of LWRs. A hard spectrum is achieved in fast reactors by decreasing moderation for a given enrichment. The rate of breeding is improved in the fast spectrum since more neutrons are produced per neutron absorbed, a value known as the reproduction factor η,

$$\eta = \frac{\bar{\nu}\sigma_f}{(\sigma_f + \sigma_c)} \tag{1.1}$$

where $\bar{\nu}$ is the average number of neutrons liberated in a fission, and σ_f and σ_c are the microscopic fission and capture cross-sections, respectively, of a particular isotope. In the fissile isotopes ^{233}U, ^{235}U, and ^{239}Pu, η varies with neutron energy as shown in Figure 1.1.

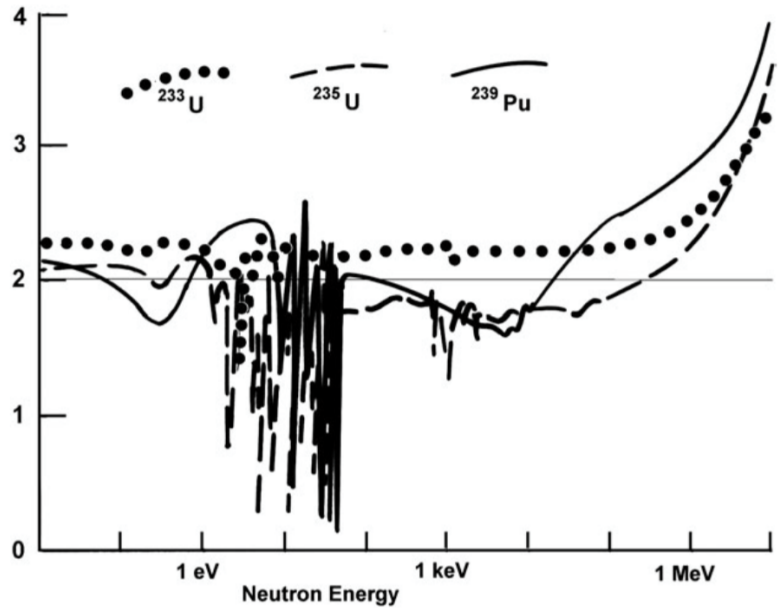

Fig. 1.1 Reproduction factor η for ^{233}U, ^{235}U, and ^{239}Pu [34]

In the U–Pu fuel cycle, as η increases, more excess neutrons are available for absorption in fertile ^{238}U to breed fissile ^{239}Pu, so the breeding ratio (fissile material produced divided by fissile material consumed) can improve. However, high heavy metal density is needed to compensate for the smaller fission cross-sections in the fast spectrum compared to the thermal spectrum. Whereas LWR fuel uses up to 5% enrichment in ^{235}U, the fraction of fissile material in fast reactor fuel is typically 20–30% [34]. Reactor coolant moderates the neutrons in the system to some degree, so fast reactor cores typically feature a small coolant

volume fraction and high power density as a result. The reduction of moderation by coolant is constrained by heat removal requirements, and while a higher coolant flow rate can be used to compensate for a smaller volume of coolant, it is limited by the available pumping power. High thermal conductivities in fast reactor fuel and coolant are therefore desirable for maintaining good heat transfer and avoiding fuel temperature peaking [81].

Metallic fuel is commonly used in fast reactors due to its high heavy metal density and relative ease of reprocessing. Although it has excellent thermal conductivity and high transient temperature limits, pure uranium metal undergoes phase transitions as its temperature increases, which can lead to contact between fuel and cladding [34]. Under certain conditions the fuel and cladding form a eutectic with a melting temperature as low as 700°C. Alloying uranium metal with a small concentration of zirconium can improve its phase stability so that swelling effects are significantly reduced. In addition, the fuel smear density is commonly reduced to safely allow space for fission gas accumulation, another mechanism that can lead to swelling if uncontrolled. Alloyed metallic fuel can have a melting temperature up to about 1000°C [34].

Reactivity control can be challenging in fast reactors because of fast spectrum effects and a high concentration of actinides in the system. Coolant voiding and thermal expansion result in reduced moderation. Whereas spectrum hardening in LWRs leads to parasitic resonance capture of neutrons, increasing neutron energy in the fast spectrum increases the fission cross-section as well as neutron yield per fission of some higher actinides. Fast reactor cores have more neutron leakage than LWR cores because of the increased neutron diffusion length with reduced moderation, as well as typically smaller geometry due to high power density. The high leakage rate somewhat counteracts the spectrum hardening effect, since the diffusion length and corresponding leakage rate are increased [34]. Many fast reactors are designed with a "pancake" core shape, referring to a relatively short aspect ratio, to intentionally increase axial leakage for improved negative reactivity feedback. In breeder reactors with a large fertile fuel mass, Doppler broadening increases capture in ^{238}U and contributes strongly negative reactivity feedback, but the Doppler effect is smaller in burners with a small fertile mass. The small delayed neutron fraction of the higher actinides reduces the effectiveness of control rods and results in fast transients, making reactivity control more challenging [76]. Complex control mechanisms may be needed to ensure negative reactivity feedback in fast reactors.

The four fast reactor systems officially selected by GIF include the sodium-cooled fast reactor (SFR), lead-cooled fast reactor (LFR), molten salt fast reactor (MSFR), and gas-cooled fast reactor (GFR). Generation IV reactors must meet the stated GIF goals of

sustainability, economics, safety and reliability, and proliferation resistance [46]. The SFR is the most developed fast reactor concept to date because of its attractiveness for breeding, with a breeding ratio of up to 1.3, and for high power density due to the superior thermal conductivity of sodium. Its drawbacks include high capital cost to mitigate the risk arising from sodium's flammability in air and reactivity with water, and the difficulty of reactor maintenance due to sodium's optical opacity. Lead coolant has extremely low moderating power and can produce a very hard spectrum, but its aggressive corrosive behaviour is difficult to manage, and it is also opaque. Helium gas coolant is optically transparent, chemically inert, and nontoxic, but requires high pressures due to its low heat capacity, which also results in fast transients and difficulty of passive decay heat removal in loss-of-coolant accidents. Molten salts have the advantages of optical transparency, high boiling point, and high heat capacity; but chemical compatibility of salts with structural materials is an area of ongoing investigation [75].

Fast reactors are under development in some countries but are not yet economically competitive with LWRs, so they have not been deployed commercially [35]. Even if capital costs can be reduced, the availability of LWR SNF and the high cost of reprocessing its plutonium for start-up fuel would still limit the rate of fast reactor deployment. Eventually fast reactor SNF can be recycled back into fast reactors, which is expected to remain more economic than reprocessing LWR SNF because of the higher plutonium content and quality of the former.

1.2 Breed-and-burn

Alternative advanced reactor technologies are being developed to extend uranium resources and minimise waste while addressing some disadvantages of the fast reactor closed cycle. The breed-and-burn (B&B) concept is a fast reactor variant that uses natural or depleted uranium feed fuel in a once-through fuel cycle with in-situ breeding and burning [12]. In a B&B reactor, fertile fuel absorbs excess neutrons from the driver regions, breeding fissile material. The partially burned assemblies are then moved to driver regions, where they sustain the chain reaction by supplying excess neutrons to regions of fresh fertile feed fuel.

B&B SNF is disposed of directly as waste, so after initial start-up, no reprocessing or enrichment is needed for the entire operating life of the reactor. Fuel cycle costs and environmental impact are predicted to be low due to the reduction of processing stages [53]. Proliferation concerns are also minimised by avoiding generation of high-grade fissile material outside the core during enrichment or reprocessing. SNF disposal shifts some

uncertain risks to the future, but the immediate fuel cycle risks are minimised while extending uranium availability by orders of magnitude compared to the LWR fuel cycle. The B&B fuel cycle ultimately has the potential to be closed by recycling its SNF, which has value due to its relatively high plutonium content, to start up a replacement B&B reactor [19].

Whereas reactivity-limited burnup corresponds to a maximum limit in conventional reactors, B&B reactors have a reactivity-limited *minimum* burnup required to sustain the B&B mode of operation. Minimum burnup is typically on the order of 20–30% FIMA (fission per initial heavy-metal atom, i.e., fraction of theoretical uranium burnup), which is similar to uranium utilisation in the fast reactor closed cycle. A hard spectrum, high heavy metal density, and low leakage rate are necessary for B&B operation to maximise neutron economy and promote efficient breeding, which reduces the minimum burnup. In addition, fast fission of ^{238}U contributes significant reactivity to the system.

The primary limitation for B&B technology is the lack of fuel and cladding materials that can survive the high required minimum burnup and fast neutron fluence. For presently available metallic fuel and stainless steel claddings that are compatible with liquid metal coolants, the established radiation-induced neutron damage limit is 200 displacements per atom (DPA), corresponding to around 10% FIMA [76, 51]. Softening the neutron spectrum could extend the cladding life somewhat by reducing fast fluence damage, but would also worsen the breeding performance of the system and increase the minimum burnup requirement.

The melt-refining process developed and demonstrated for metallic fuel in the Experimental Breeder Reactor II project has been proposed as a potential solution to allow high fuel burnup in a once-through cycle [24]. The partially burned fuel is declad and melted, gaseous and volatile fission products are released, and the fuel is refabricated with new cladding. This process relieves fission gas pressure and removes radiation-induced defects in the fuel. It excludes chemical separation of actinides and most fission products, which makes the process simpler and more proliferation-resistant than conventional chemical reprocessing methods, in which separate streams of fissile uranium and weapons-grade plutonium are generated [50].

Another option to extend burnup is vented fuel technology, which was developed to allow increased fuel burnup in fast reactors by releasing fission gases from the fuel element. Creep damage to cladding is induced by mechanical stress from internal fission gas pressure, elevated temperatures, and irradiation effects [78]. Gaseous fission products can also accelerate corrosion of the cladding. Venting reduces the cladding creep damage rate, allowing a higher cladding performance-limited burnup, and possibly also allowing thinner cladding, which

can improve neutron economy to allow lower enrichment or higher reactivity-limited burnup. However, by releasing fission products to the primary coolant, the first containment barrier in a reactor is lost, so additional safety precautions may be required. Some experience with venting was obtained with the Dounreay Fast Reactor in the 1960s, and the technology has been developed further and included in numerous reactor designs since then [31, 78].

Several distinctive features of the B&B system require special design considerations. Long fuel residence times in the B&B system challenge traditional fuel cycle economics because the fuel must be manufactured and loaded in the reactor long before it begins to generate significant power [82]. The large area reserved for low-power fertile fuel in the B&B reactor decreases the overall core power density. However, less shielding is needed at the edges of the core because the fertile fuel captures most leaking neutrons. Unlike conventional fast reactors, which deliberately allow high leakage to contribute negative reactivity feedback, leakage from the reactor must be minimised in B&B reactors and therefore alternative forms of reactivity control may be needed. Nonlinear reactivity–burnup behaviour and relatively large cycle reactivity swing resulting from breeding requires careful fuel management, which may include complex shuffling and zoning schemes.

Axial burnup peaking in B&B fuel may be pronounced because the typical cosine power shape increases the breeding of plutonium at the axial midplane, which then further concentrates the flux and increases burnup and accumulation of fission products at the midplane. Highly non-uniform axial burnup increases the required average minimum burnup of the fuel batch and exacerbates axial power peaking, which decreases the average allowable power density [50]. Since B&B reactors use natural or depleted uranium, enrichment zoning is not an option, but fuel density zoning may be an alternative approach for power shaping [21]. The melt-refining process, in which the fuel is melted and reformed between burnup cycles, also returns the fuel to a uniform composition [24].

The B&B concept was first proposed by Feinberg in 1958 [12], followed by investigations of sodium-, gas-, and lead-cooled B&B designs at Brookhaven National Laboratory and Oak Ridge National Laboratory in the United States between the 1970s and 1990s. The CANDLE reactor was proposed in the 2000s, featuring a core that requires neither refuelling nor shuffling, so that the breed–burn wave travels through the fuel [64]. While simpler, an unshuffled core compromises neutron economy because many neutrons are absorbed in already-burned fuel. Historically, B&B research has focused on sodium-cooled designs, since the excellent thermal properties of sodium allow a high fuel volume fraction, resulting in strong breeding performance with a minimum burnup around 20% FIMA. In lead-cooled reactors, the coolant flow rate is limited because of lead's corrosive behaviour, so the fuel pin

pitch must be expanded to satisfy cooling requirements, leading to minimum burnup around 30% FIMA [23]. The achievable fuel volume fraction is also relatively limited in gas-cooled B&B reactors due to cooling considerations. Advanced, high-density fuel materials or an inverted tube-in-duct fuel assembly design may be used to increase heavy metal density in these reactor systems. The use of LEU feed fuel has also been explored to relax the neutronic constraints in a gas-cooled B&B reactor [82].

In 2006, TerraPower launched an effort to develop the sodium-cooled Traveling-Wave Reactor (TWR), which uses uranium–zirconium metal alloy fuel, ferritic–martensitic steel cladding, and fission gas venting technology. A thin steel wire is helically wrapped around each fuel pin to separate it from the other pins in the assembly, allowing for cooling by sodium flowing through the assemblies. Resistance orifices at the bases of the assemblies control coolant flow in order to compensate for power differences in the central driver region and outer fertile region. Control rods are used to offset the small initial excess core reactivity and for shutdown, and to partially compensate for positive coolant temperature coefficients [10]. Other forms of active reactivity control may be needed to ensure negative reactivity feedback. The minimum burnup limit of the present TWR configuration requires an estimated 240 to 350 DPA, but 200 DPA is the currently known limit for metallic fuel and stainless steels. Until these materials challenges can be resolved, a limited-separations process (similar to the melt-refining process described earlier in this section) is proposed to allow the required minimum burnup in the TWR.

More recently, the feasibility of B&B operation in molten salt reactors (MSRs) has been the subject of several studies exploring the effect of fuel composition and reflector materials on the required core volume and minimum burnup [42, 26, 20]. These studies assume a pool-type MSR configuration, which contains a homogeneous mixture of fuel at all burnup stages. Discharged fuel streams therefore contain the average fuel mixture, so it may be more challenging to achieve high burnup without discrete fuel units and traditional fuel management [26]. In 2016, TerraPower announced development of a second B&B reactor project, the Molten Chloride Fast Reactor (MCFR) [70]. The MCFR is a pool-type MSR designed to operate at high temperatures, with the aim to supply energy for industrial applications and other markets beyond electricity. The MCFR was awarded $40 million in research and development funding by the U.S. Department of Energy, initiating a partnership between TerraPower, the utility Southern Company, Oak Ridge National Laboratory, the Electric Power Research Institute, and Vanderbilt University. An 1100 MWth prototype reactor is planned by 2030.

1.3 Molten Salt Reactors

MSRs may use a molten salt as the reactor coolant with solid fuel, or as a liquid fuel. The chemical and thermophysical properties of molten salts combined with their low absorption cross-sections produce attractive cooling performance. Common salts are relatively inert, nontoxic, and not flammable or explosive, making them safe and economic to handle and circulate in a reactor coolant system. Since they are radiation-resistant, with regular purification they can be used repeatedly in the reactor. Their optical transparency, shown in Figure 1.2, may also make reactor maintenance easier than with some opaque coolants such as sodium and lead.

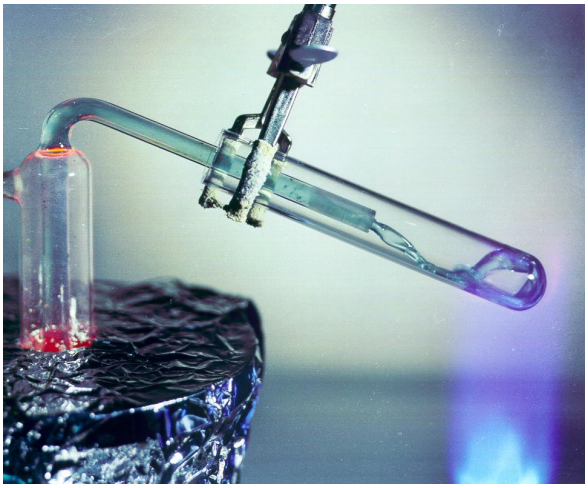

Fig. 1.2 Molten salt [17]

Molten salts have excellent heat capacities and thermal conductivities similar to that of water. Relatively high melting temperatures and viscosities may impose limits on the design of the coolant system, so a salt with a manageable combination of properties should be selected. FLiBe, a mixture of lithium fluoride (LiF) and beryllium fluoride (BeF_2), is a popular molten salt for engineering applications because of its relatively low viscosity and low melting point. MSRs often require auxiliary heating to melt the salt at start-up and in case of freezing during operation, and structural materials must be selected that can withstand high temperature operation. The low vapour pressure of molten salts allows high temperature operation with near-atmospheric pressures, which offers the potential for high thermodynamic efficiency and process heat applications. Low pressure operation reduces the cost and complexity of the reactor system, as well as the risk of radionuclide release in an accident.

Molten salts may be used as fuels that require no fabrication, given the high solubility of actinides and some fission products in fluoride and chloride salts. Strong thermal expansion of molten salt fuel produces negative fuel temperature coefficients, even in the fast spectrum [37]. Liquid-fuelled MSRs can be designed to use either the uranium–plutonium or thorium fuel cycle, and a large number of candidate fluoride and chloride salt compositions exist. The flexibility of the fuel composition allows MSRs to be designed as thermal, epithermal, or fast reactors, and they may be configured for breeding or burning [37].

In liquid-fuelled pool-type MSRs the molten salt acts as both fuel and coolant, so cladding is eliminated and neutron economy is improved due to reduced capture in structural materials. The ease of regular online refuelling and online or batch reprocessing can also improve neutron economy as well as reactor availability. Online refuelling allows low excess reactivity to be maintained, which may reduce the source term for improvement of the safety case, but the technology is not mature. Pool-type MSRs with negative reactivity feedback cannot "melt down", and high solubility to actinides and fission products combined with high melting and boiling points provides an effective containment mechanism.

Significant remaining technical challenges for MSRs include corrosion and irradiation damage to structural materials in contact with fuelled salt; production of radioactive tritium from neutron absorption in lithium and beryllium in FLiBe; demonstration of online reprocessing methods for liquid fuel; and development of simulation capabilities. The coupling between neutronic, thermal–hydraulic, and chemical behaviour of the fuel salts must be thoroughly investigated [65].

1.3.1 Thorium

Molten salt-fuelled reactors are particularly attractive reactor concepts for the thorium fuel cycle, which has been proposed to meet the Generation IV objectives of sustainability and proliferation resistance. In a thorium-fuelled MSR, use of liquid fuel could avoid numerous issues related to the lack of experience with thorium fuel fabrication and the difficulty of reprocessing thorium fuels, and ^{232}Th–^{233}U breeding can be realised in the thermal spectrum [13]. Thorium fast reactors have also been considered due to the possibility of a negative coolant temperature coefficient in the fast spectrum, because of the relatively low probability of fast fission in ^{232}Th and the smaller η value of ^{233}U compared to ^{239}Pu [40]. Thorium-fuelled B&B reactors have been studied, but the low neutron yield of the bred ^{233}U in the fast spectrum (shown in Figure 1.1) makes B&B operation difficult to sustain [43].

Thorium is briefly investigated in this thesis to assess its suitability for B&B operation in the proposed MSR configuration.

1.3.2 Early MSR development

The first liquid-fuelled reactor built in Oak Ridge National Laboratory's molten salt program of the 1950s was the Aircraft Reactor Experiment (ARE). A molten uranium fluoride salt was contained in holes bored into hexagonal BeO blocks, with sodium coolant pumped through the interstices between blocks [6]. Thermal expansion of the salt upwards into a boron carbide slab could quickly control the reactivity, but thermal conductivity of the stagnant fuel was not sufficient to maintain safe fuel temperatures except at very low power, and the effects of natural convection were neglected. In the next design iteration, the fuel was circulated through serpentine passages in the core and through a finned heat exchanger, but this configuration could not be quickly drained for emergency shutdown and maintenance.

The molten salt reactor experiment (MSRE) was developed in the 1960s. In the two-fluid MSRE design, concentric spheres are divided by a barrier of Hastelloy N, a high-temperature nickel alloy; the inner core contains fissile ^{233}U-carrying fluoride salt while the blanket salt contains fertile ^{232}Th. Graphite's limited lifetime under irradiation proved to be a major weakness of the two-fluid design, requiring regular replacement of the components. The two-fluid design was therefore abandoned for the neutronically inferior but simpler single-fluid MSRE, which achieves a breeding ratio of 1.06 and was operated from 1965 to 1969 [49, 65]. A preliminary design for a molten salt breeder reactor (MSBR) was also completed in the late 1960s, but it was never built. The MSBR is a thermal spectrum thorium-fuelled reactor that contains a single molten salt separated into two distinct spectral zones to produce effective core and blanket regions [49].

Further work on MSRs was consolidated in the 1970s when the United States focused on SFR technology as higher priority due to its high breeding ratio and the perceived shortage of uranium at the time. Limited MSR research in the 1970s included a denatured molten salt reactor (DMSR) that was developed to be proliferation-resistant. The DMSR is initially fuelled with 19.75% enriched uranium and sufficient ^{238}U and ^{232}Th to denature the salt, in a FLiBe mixture [11]. With an online chemical reprocessing facility to remove the fission product poisons krypton and xenon, a breeding ratio of 1.0 is achieved.

While the American MSR program focused on thermal MSRs using fluoride salts, fast MSRs using chloride salts have been investigated in Switzerland since the 1970s. Taube and Ligou designed an 800 MWe molten-chloride fast-breeder reactor (MCFBR) with fuel

salt consisting of 16 mol% $PuCl_3$ and 84 mol% NaCl, and fertile coolant salt consisting of 65 mol% $^{238}UCl_3$ and 35 mol% NaCl [69]. The coolant blanket surrounds a contiguous core, circulates through serpentine tubes inside the core, and passes through external heat exchangers. An overflow tank allows thermal expansion of the fissile core salt to ensure a strongly negative temperature coefficient of reactivity. In addition to negative reactivity feedback, high heat capacity and small temperature gradients in both the fuel and coolant salts ensure strong thermal and reactivity stability. However, at the designed power density, a high coolant velocity is needed, which increases the required pumping power and can result in erosion of the structural materials. Continuous removal of fission products keeps the required plutonium inventory low and decreases corrosion of the structural materials, but corrosion remains the biggest disadvantage of this system. A molybdenum alloy is the best corrosion-resistant candidate for the system, but the high absorption cross-section of molybdenum may impose a prohibitive reactivity penalty.

These early MSR concepts illustrate the difficulty of achieving high breeding ratios using fluoride salt fuel, and the relative complexity of previous dual-salt configurations that rely on forced convection. Most modern MSR designs feature a single-fluid pool-type configuration using pumps to circulate the fuel salt.

1.3.3 Molten Salt Fast Reactor

The Molten Salt Fast Reactor (MSFR), shown in Figure 1.3, is the Generation IV reference MSR concept [46]. The main fuel loop contains a lithium fluoride salt with a mixture of thorium, plutonium, and ^{233}U, and a radial blanket contains a fertile salt of $LiF–ThF_4$. The axial reflectors are made of nickel-based alloy [57]. Thorium use in an MSR with online reprocessing reduces the challenge associated with low maturity of the thorium fuel cycle infrastructure. MSFR reprocessing can be performed online or in batches, and the rate of reprocessing controls the equilibrium reactivity by removing fission products and replacing them with an equivalent mass of thorium [13].

Since the goal of the MSFR is consumption of legacy LWR wastes, the low breeding potential of thorium in the fast spectrum is acceptable. The MSFR has a significantly softer spectrum than a fast LFR or SFR, resulting from elastic scattering resonances in fluorine and lithium in the salt. As a result, the MSFR actually has better breeding performance from thorium fuel than it would with uranium. Doppler and salt thermal expansion effects yield strongly negative reactivity feedback, but care must be taken to avoid overcooling transients.

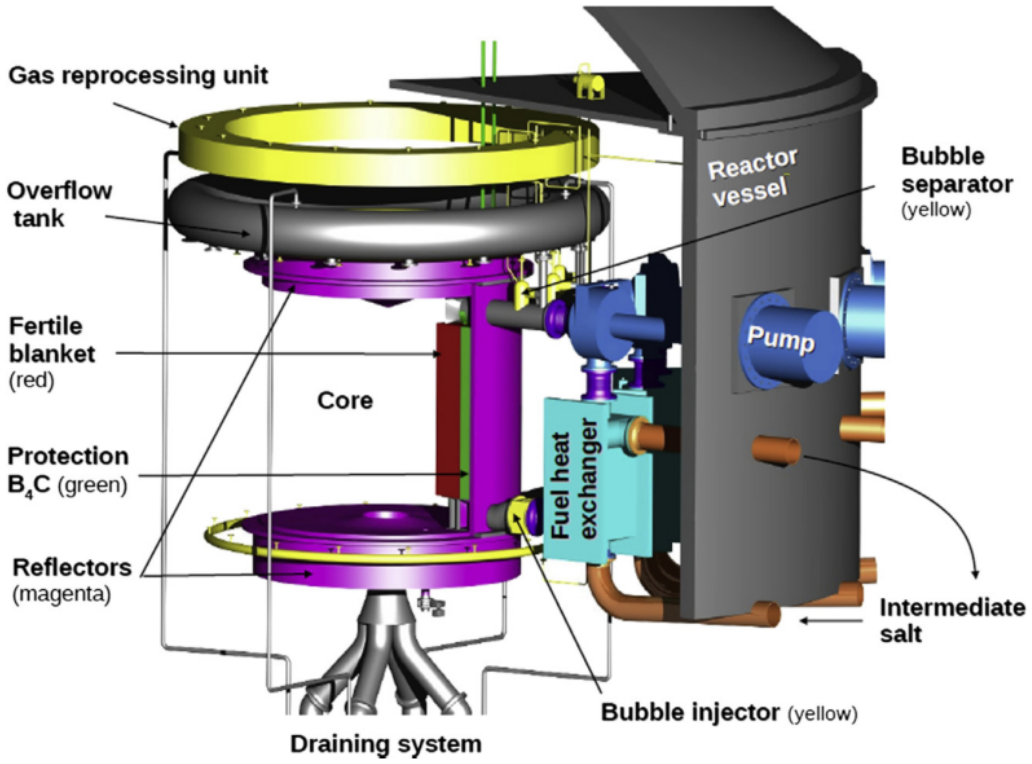

Fig. 1.3 MSFR design [13]

1.3.4 Fluoride salt-cooled high-temperature reactor

A solid-fuelled MSR variant that emerged in the 1970s is now known as the fluoride salt-cooled high-temperature reactor (FHR). The FHR is viewed as a relatively near-term application of molten salt technology that can pave the way for later introduction of molten-fuelled MSRs [46]. A major advantage of using a separate, sealed fuel form is that maintaining clean coolant salt results in significantly less corrosion to structural materials and coolant pumps than with fuelled salt. A key feature of modern FHRs is tri-structural isotropic (TRISO) fuel technology, developed for use in high-temperature gas-cooled reactors, but able to achieve much higher power densities when paired with molten salt coolant. TRISO fuel, depicted in Figure 1.4, consists of SiC-coated fuel microspheres embedded in a graphite matrix. It has excellent safety characteristics both during irradiation and in long-term storage as SNF, due to the radiation resistance and fission-product containment by the SiC coating on the fuel particles. It is also highly proliferation resistant due to the strength of the SiC and incorporation of graphite moderator into the fuel form, which reduces the density of fissile material [16]. A disadvantage of these features is the likely high cost of fabrication and

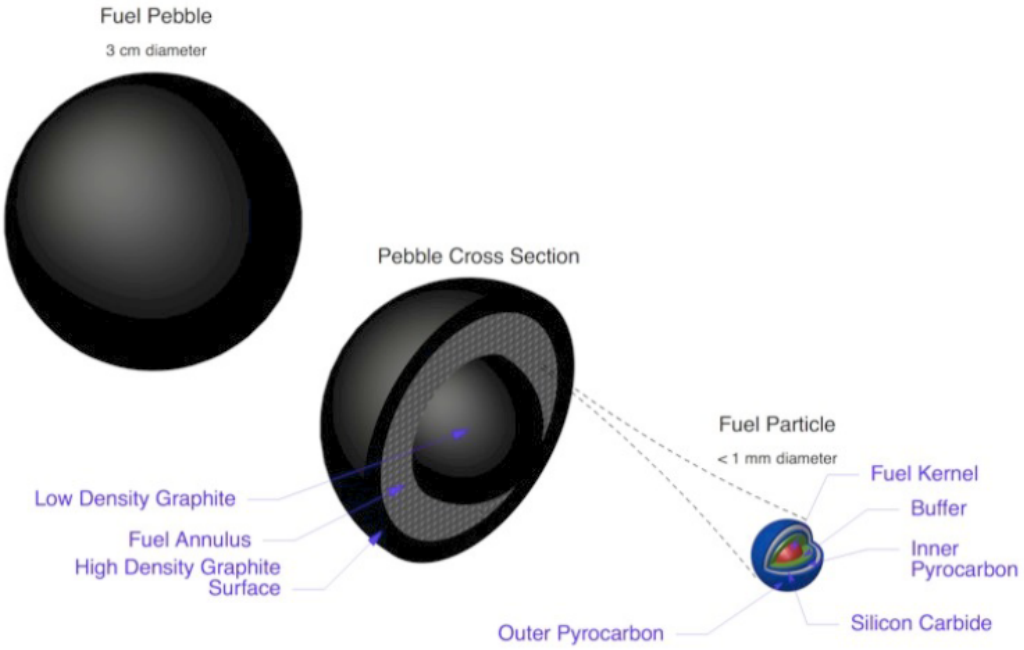

Fig. 1.4 TRISO fuel pebble [2]

difficulty of reprocessing. Various TRISO fuel forms are being explored for FHRs, including cylindrical pins, annular cylinders, plate-type fuel, and fuel pebbles [79, 15].

A significant neutronic weakness of TRISO fuel designs is the near-homogeneous mixing of fuel and moderator due to the distribution of fuel particles within the moderating graphite [56]. This configuration minimises spatial self-shielding, so as the neutrons are moderated within the fuel form, many are lost to resonance absorption in ^{238}U. To compensate for this negative effect on neutron economy, enrichment near 20% and a high packing fraction of TRISO particles may be needed, and achievable burnup is relatively low. The initial cost of TRISO fuel is expected to be much higher than traditional LWR fuel, and the cost savings of scaling up production cannot yet be reliably predicted. The need to use higher enrichment than LWRs will also incur high up-front costs because, in the existing fuel manufacturing infrastructure, most suppliers are licensed and equipped only to produce up to 5% enriched uranium [65]. TRISO fuel satisfies safety and nonproliferation goals, but economics and resource sustainability remain open questions. Another important challenge in FHR development is management of the tritium produced by neutron absorption in the lithium and beryllium of FLiBe coolant. Tritium is a highly radioactive isotope that at high temperatures can diffuse through heat exchangers to be released to the environment [16].

1.3.5 Flexible conversion ratio salt-cooled reactor

A fast reactor with solid metallic fuel and molten salt coolant was designed as one part of a larger study of flexible conversion ratio fast reactors. The core was designed for conversion ratios of zero and one, with a power rating of 2400 MWth. Numerous chloride and fluoride coolant salt candidates were screened for neutronic and thermal–hydraulic characteristics, and the ternary chloride eutectic NaCl–KCl–$MgCl_2$ (30–20–50 mol%) was chosen for having relatively low melting point, viscosity, thermal expansion, and moderating power. Still, thermal expansion of the coolant produces a large positive coolant temperature reactivity coefficient [66]. This effect is mitigated somewhat by reducing the coolant fraction in a tight hexagonal fuel lattice with wire-wrapped fuel pins. However, the coolant fraction cannot be reduced sufficiently to meet reactivity feedback requirements without severely compromising thermal–hydraulic performance, so it was necessary to introduce lithium expansion modules to ensure negative coolant temperature feedback. This final design achieves a core power density of 130 kW/l with a core pressure drop of 700 kPa and a peak cladding temperature of 650°C [52]. The lithium modules operate passively by thermal expansion, which pushes neutron absorbing ^{6}Li into the core, but negative reactivity feedback is not inherent to the reactor system. While this configuration could also be explored for B&B operation, the shortcomings of solid fuel discussed in Section 1.2 apply, and additionally the properties of molten salt coolant make passive reactivity control even more challenging to achieve in this system than in liquid metal-cooled reactors.

1.3.6 Moltex Stable Salt Reactor

The Stable Salt Reactor (SSR) by Moltex Energy is a fast reactor designed to consume legacy wastes from the LWR fuel cycle. A fuel salt circulates by natural convection within individual fuel tubes, which are submerged in a pool of fuel-free coolant salt that is pumped through the core. The SSR incorporates the advantages of MSRs while allowing replacement of fuel assemblies like in LWRs. Separation of the fuel and coolant, like in the FHR, reduces corrosion to structural components and allows simplified core design. The fuel salt is a mixture of NaCl and actinide– and lanthanide–trichlorides, and the coolant salt is ZrF_4–NaF–KF. A chloride salt is selected for the fuel, due to its higher actinide solubility compared to fluoride salts, while the fluoride salt coolant is preferred for its thermodynamic stability and ease of chemistry control [5]. Non-reactor grade zirconium (containing naturally occurring traces of the neutron poison hafnium), and natural chlorine containing 75% of the absorbing isotope ^{35}Cl are assumed to have negligible neutronic effects in the fast spectrum [62].

Zirconium in the coolant salt scavenges free chlorine and fluorine ions so that they do not react with the protective chromium oxide layer on stainless steels, and the oxide layer protects the steel from corrosion. Sacrificial zirconium metal chunks can also be added to the fuel tubes without risking interference with other reactor components, such as pumps [61]. Figure 1.5 illustrates the reactor configuration, with each fuel assembly containing a bundle of individual fuel tube elements, and the fuel and coolant flow patterns are shown in the expanded view.

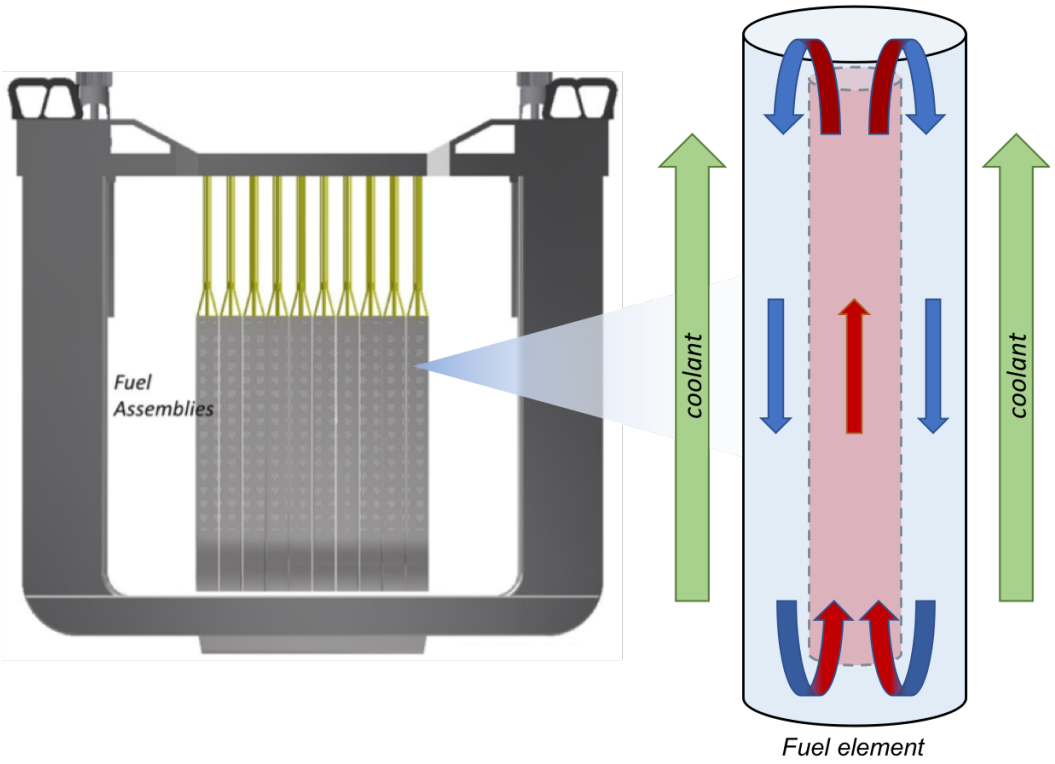

Fig. 1.5 Moltex SSR with naturally convecting fuel [44]

Natural convection of the fuel salt enhances heat transfer to the coolant so that larger tube diameters can be used than if only conduction heat transfer is present. Moltex performed computational fluid dynamics (CFD) calculations showing that, for 10 mm diameter tubes, a power density of 200 kW/l of fuel salt is achievable while remaining below the fuel boiling point [61]. The operating temperature of the fuel salt ranges from just above the melting point (in the range 450–520°C) to 1200°C, but the containing tube temperature rises just a few tens of degrees above the coolant salt temperature [38].

Each fuel tube is approximately three-quarters full of fuel salt, and the remaining space at the top serves as a gas plenum and allows fuel expansion. A vent at the top is adapted from

the Dounreay Fast Reactor design; it allows gaseous fission products to escape to an argon blanket above the coolant, while preventing coolant salt entering the fuel tube [59]. The fuel tubes are fabricated of high-temperature nickel alloy Nimonic PE16, and are arranged in 18-by-21 hexagonal assemblies with pin diameter of 10 mm and a 1-mm helical wire wrap [60]. The main tank is fabricated from corrosion-resistant stainless steels and sits below ground level in a concrete pit. The tank contains a large pool of coolant salt with a grid of fuel assemblies at the centre. Pumped secondary heat exchangers are at the periphery of the tank, and coolant flows downwards through these and upwards through the fuel assemblies. In the event of fuel element failure, contamination of the coolant salt would require maintenance, but introduces little radiological risk. Fission products are highly soluble in the molten salt, and the coolant salt is also isolated from the power cycle by a secondary circuit. The overall temperature reactivity coefficients are strongly negative, and internal cladding pressure remains low due to venting and allowance of the liquid fuel expansion. Reactivity control during reactor operation is achieved passively by feedback mechanisms such as thermal expansion of the fuel, and control rods are included for start-up and shutdown [61].

Several other aspects of the Moltex fuel tubes concept allow for improved neutron economy and simplified reactor design compared to a traditional MSR. In a single-fluid pool-type MSR, the fuel salt circulates from the core to the external fuel circuit, which includes heat exchangers, pumps, and other auxiliary components. The drift of delayed neutron precursors (DNP) to the external circuit results in some loss of reactivity because the external delayed neutrons are not utilised as effectively as in-core. DNP drift also makes the system neutronically sensitive to the fuel pump speed, so transients must be carefully controlled during fuel pump start-up and shutdown [37]. Pool-type MSRs require shielding for the external circuit in addition to the core, and corrosion and irradiation damage to the pumps and reactor vessel pose a significant materials challenge. Since the fuel salt fills the entire reactor vessel, a relatively large mass of fissile and fertile material is required to sustain criticality. In contrast, the Moltex concept confines the more corrosive fuel salt to replaceable fuel tubes in the core, which also reduces the required fuel mass and avoids DNP drift.

The SSR is fuelled with a mixture of LWR SNF and natural uranium dissolved in a chloride salt. Since the molten fuel can tolerate a low-purity mixture without significantly affecting its thermophysical properties, TRUs can be relatively cheaply separated from LWR SNF and dissolved in the carrier salt [59]. Fuel element fabrication is greatly simplified for a molten salt compared to solid fuels. However, reprocessing is still needed to extract TRUs from LWR SNF, carrying the proliferation and radiotoxic risks associated with fast reactors. While the SSR offers waste disposition with a cheap and simple design, its resource

utilisation is comparable to the current generation of reactors. Moltex are also exploring a thermal SSR for thorium-based breeding, with fissile material in the fuel tubes and fertile thorium-carrying salt in the coolant loop [60]. Further applications and fuel cycle objectives could be explored within the SSR design concept.

1.4 Thesis Objectives

A breed-and-burn molten salt reactor (BBMSR) is proposed to address the Generation IV goal of resource sustainability in a once-through cycle, avoiding high enrichment and reprocessing so that waste generation and proliferation risk are minimised. Use of molten salt fuel and coolant produces a passively safe alternative to solid-fuelled B&B designs, and the Moltex dual-salt configuration offers a solution to the materials limitations of both single-fluid pool-type MSRs and solid-fuelled reactors. Primary objectives of the BBMSR are to achieve significantly higher uranium utilisation than the current LWR fuel cycle, and to achieve competitive economics by maximising the core power density.

This thesis aims to assess the feasibility of the BBMSR concept in terms of neutronic and thermal–hydraulic performance of the dual-salt fuel configuration. Practical limitations of materials compatibility and manufacturing capabilities must be considered, based on the available knowledge. B&B operation requires a hard spectrum and high heavy metal loading, which is challenging to achieve in a molten salt configuration with separate fuel and coolant. The BBMSR should be designed with a large fuel volume fraction to help satisfy neutronic requirements, but this will be limited by heat removal considerations. Since heat transfer by natural convection of the fuel salt is both a key feature and a limiting phenomenon for BBMSR design, a major focus of this work is to develop methods that enable efficient thermal–hydraulic analysis of the fuel concept in varying configurations.

Additional goals of this thesis are to understand the limits of the design space and develop viable fuel configurations. Fuel design scoping studies are performed for both natural uranium and LEU (up to 20%) feed fuel, with LEU considered as a potential avenue to relax neutronic constraints and allow more design flexibility. To assess whether the BBMSR offers the potential for significant improvements, achievable fuel utilisation and power density are characterised for natural uranium and LEU fuel versions, and are compared with typical LWR performance.

1.5 Thesis Organisation

This thesis consists of six chapters. The first chapter introduces the BBMSR as a new reactor concept proposed to address the Generation IV sustainability objective. Fast, B&B, and molten salt reactor technologies are reviewed as a basis for BBMSR development and overview of existing challenges. The objectives of this thesis are identified.

Chapter 2 describes the potential capabilities and limitations of the BBMSR concept. It is qualitatively compared with previous fast, B&B, and MSR concepts to highlight its distinguishing features and potential advantages that may help to meet several reactor design and fuel cycle objectives. Preliminary neutronic modelling is performed to assess the feasibility of B&B operation in the dual-salt configuration, and additional design requirements and challenges are identified based on the results. The feasibility of using the proposed fuel, coolant, and cladding materials is discussed. Known properties and open questions regarding materials compatibility are briefly reviewed.

Chapter 3 analyses the natural convection of molten salt fuel in a tube. As a first approximation, a simplified analytical solution of the coupled temperature–velocity profile is derived. The analytical result emphasises the sensitivity of the heat transfer performance to the flow profile, so the BBMSR fuel concept is modified to include an inner wall that divides the ascending and descending fuel salt flows. CFD is then used to model the ascending flow section and obtain a new heat transfer correlation that captures its unique physics.

Chapter 4 presents the development of a finite-difference model (FDM) which implements the new heat transfer correlation and traditional correlations to iteratively solve for the temperature and velocity distributions in both sections of the concentric fuel. Using the FDM, the effect of varying fuel geometry and heat generation rate on the heat transfer performance is studied. The FDM is then integrated into a design search program that identifies the operational limits for a given fuel geometry, within a set of defined constraints. The program enables efficient analysis of thermal–hydraulic fuel design options.

In Chapter 5, the findings and methods presented in the previous chapters are incorporated into a coherent fuel design scoping study for natural uranium and LEU feed. A neutron balance method is used to rigorously quantify the minimum burnup requirement for B&B operation, and the thermal–hydraulic design search program calculates the allowable power density of potential fuel configurations. Viable fuel configurations for natural, 5% enriched, and 20% enriched uranium are developed and evaluated in terms of uranium utilisation and power density. The BBMSR fuel options are compared with typical LWR performance to emphasise the strengths of the BBMSR concept.

Chapter 6 summarises the work described in this thesis, discusses the methods and results, and recommends next steps for design of the BBMSR system.

Chapter 2

Concept Description and Feasibility

2.1 Conceptual Description of the BBMSR

This section summarises how the BBMSR combines the attractive features of previous B&B and MSR concepts, while avoiding some of their most significant disadvantages.

B&B reactors enhance proliferation resistance and fuel cycle sustainability using a once-through cycle, but solid-fuelled designs face several challenges that lack elegant solutions. High burnup and a hard neutron spectrum are required, which cause the accumulation of structural defects in fuel and cladding materials. The tendency for highly centre-peaked axial burnup in B&B fuel exacerbates these effects. Advanced materials that can withstand high fluence and high temperature are being developed, but until they are realised, solid fuel must be reconditioned and reclad mid-burnup. In the BBMSR, mixing by natural convection of the fuel salt within the tubes produces an axially homogeneous fuel composition throughout the burnup cycle. While cladding fluence will still peak at the centre, the fuel salt can be easily transferred to new cladding tubes in a process that should in practice be cheaper and easier than the reconditioning process for solid fuel. As mentioned in Section 1.2, modern steels have a neutron damage limit corresponding to approximately 10% FIMA, so recladding may be needed a few times to satisfy typical B&B burnup requirements of 20–30% FIMA. The requirement for cladding strength should be particularly low for the BBMSR, since the vented liquid fuel and unpressurised coolant exert little force on the cladding, in contrast to some fast reactor fuels that accumulate internal pressure as they are irradiated.

In most fast reactor designs, positive coolant temperature reactivity feedback is challenging to manage. Whereas conventional fast reactors rely on neutron leakage to compensate for this effect, leakage must be minimised in B&B designs to preserve neutron economy, so it may not be possible to ensure passive reactivity feedback without the use of reactivity control

devices. In the BBMSR, coolant temperature effects should offset by a strongly negative fuel temperature coefficient resulting from thermal expansion of the molten salt fuel, which could maintain inherent passive safety. While quantification of this behaviour is beyond the scope of the present work, previous liquid-fuel MSR designs have demonstrated strongly negative fuel temperature reactivity feedback, including two-fluid designs [49, 69, 60].

B&B MSRs can avoid the issues of limited fuel and cladding lifetimes and positive reactivity feedback encountered in solid-fuelled B&B designs. However, pool-type configurations present the added challenge of a homogeneous fuel mixture in the core, so traditional fuel management strategies, such as fuel zoning and shuffling to increase burnup, cannot be used. With B&B mode, irradiation and corrosion damage to structural materials and pumps may be even more severe than in prior thermal and fast MSR concepts. The dual-salt configuration of the BBMSR maintains the advantages of solid fuel for fuel management and burnup accounting, which are particularly important in B&B mode. The other, more general benefits of separate fuel and coolant forms have already been discussed in Section 1.3.6.

The BBMSR is distinct from the Moltex SSR, which is designed to quickly and cheaply burn LWR wastes without a particular emphasis on fuel utilisation. The thermal, thorium-based SSR may improve fuel utilisation by breeding, but addition of thorium to the coolant sacrifices several of the advantages of maintaining separate fuel and coolant. As a B&B reactor, the BBMSR is designed to enable both breeding and burning within the fuel tubes, without any treatment or separation of the fuel between the two modes.

The BBMSR with a dual-salt configuration has some potential disadvantages that will require careful design solutions. The lower density of a molten salt fuel compared to solid metallic uranium results in reduced heavy metal density. In contrast to a pool-type MSR, the presence of cladding material in the core increases parasitic neutron capture. The following section investigates the neutronic feasibility of the dual-salt configuration. Physical separation of the two salts also means that fission energy is not released directly into the coolant, so localised power peaking must be managed. In terms of reactivity feedback, the delay in temperature increase between fuel and coolant may be beneficial, since fuel expansion suppresses reactivity while coolant expansion has the opposite effect.

2.2 Neutronic Feasibility Assessment

In order to assess the feasibility of B&B operation in the dual-salt fuel tube concept, an infinite lattice model is used to simulate reactivity–burnup performance for various fuel geometries and compositions. An initial configuration is based on the Moltex SSR and

then systematically modified to improve neutron economy for B&B operation. The infinite multiplication factor k_∞ is calculated over 0 to 450 MWd/kg burnup in a two-dimensional infinite lattice unit cell. Since this early scoping study involves numerous simplifications, breeding performance is not quantified rigorously; rather, the objective of the present analysis is to identify BBMSR configurations that can breed enough plutonium to become supercritical ($k_\infty \geq 1$). For self-sustaining B&B operation, each unit of fuel in the reactor must eventually become a net contributor of neutrons to fresh fertile regions.

For all configurations explored in this chapter, the modelled unit cell contains a homogeneous mixture of the reactor materials with volume fractions representing a square lattice, pitch-to-diameter ratio of 1.0, and cladding thickness of 0.5 mm, as illustrated by Figure 2.1. Spatial homogenisation reduces computation time and is a reasonable approximation in modelling fast-spectrum systems, given their relatively long neutron diffusion lengths. While homogenisation may introduce small errors with coolants of non-negligible moderating power, it is assumed to be sufficiently accurate for the purposes of this feasibility assessment.

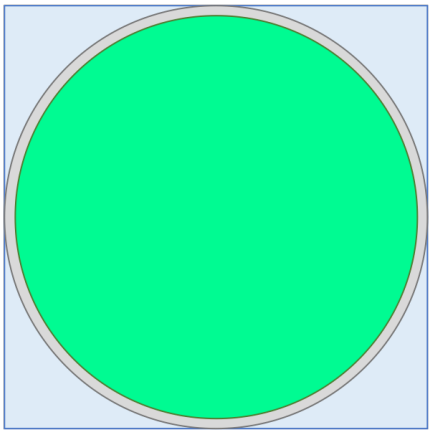

Fig. 2.1 Modelled unit cell

2.2.1 Serpent calculation

The Monte Carlo neutron transport code Serpent-2 is used for neutronic modelling of the BBMSR. Monte Carlo is a stochastic method that traces neutron histories by simulating their interactions with atoms in the system based on their neutron reaction cross-sections. A large number of neutron histories is used to allow statistical convergence. Compared to deterministic methods, the Monte Carlo method produces more accurate results since fewer assumptions are used, but is also more computing intensive and time consuming.

Serpent is a continuous-energy Monte Carlo code that uses a unionised energy grid to minimise the number of grid search iterations and reduce computation time, although this feature requires a large amount of computer memory [39]. Macroscopic cross-sections for each material are pre-generated at the beginning of the calculation, before the neutron interaction simulations are performed. For burnup calculations, Serpent automatically selects the appropriate fission and activation products and actinide daughter nuclides.

The nuclear data library ENDF/B-VII.1 has been used for all calculations included in this thesis. Burnup calculations of the BBMSR pin cell use a single depletion zone, since natural convection of the fuel salt produces a homogeneous composition within each fuel element. All Serpent simulations reported in this chapter use a population of 2000 neutrons with 50 inactive cycles and 500 active cycles. The typical mean statistical errors are 30–50 pcm.

2.2.2 Initial configuration

In the original SSR designed as a fast plutonium burner, the fuel salt is a mixture of natural UCl_3, $PuCl_3$, and NaCl carrier salt (20–20–60%). The coolant is the fluoride eutectic ZrF_4–NaF–KF (42–10–48 mol%). Early literature specifies a power density of 250 kW per litre of fuel salt, with 10 mm outer diameter fuel tubes and a pitch-to-diameter ratio of 1.0 in a square assembly lattice [62, 38]. This SSR configuration is adapted slightly to arrive at the initial configuration for the BBMSR, in which the fuel mixture is 40% UCl_3 and 60% NaCl, with natural uranium and chlorine isotope compositions. The cladding is modelled as natural molybdenum, to approximately represent molybdenum alloys which are attractive materials for molten salt reactors due to their resistance to corrosion and high temperatures.

Figure 2.2 compares burnup versus k_∞ of the SSR burner and the initial BBMSR. The SSR exhibits a linear burnup trend, consistent with a conventional fast reactor, whereas the BBMSR is deeply subcritical at the beginning of cycle, when it must be sustained by neutrons from a supercritical fuel region. As burnup progresses, ^{238}U absorbs neutrons to breed ^{239}Pu, so k_∞ increases to a peak between burnups of 100 and 150 MWd/kg, and then decreases slowly for the rest of the cycle as the fuel is depleted. This initial configuration never breeds enough plutonium to become critical, so it is not capable of self-sustaining B&B operation. Section 5.1.2 quantifies the requirement for self-sustaining B&B operation using the neutron balance method employed in previous B&B studies [53, 24].

Next, the heavy metal loading is increased, which is described in Section 1.1 as an important feature to improve breeding in the fast spectrum, particularly with a primarily fertile fuel. The BBMSR tube diameter is increased from 10 mm to 150 mm, which increases

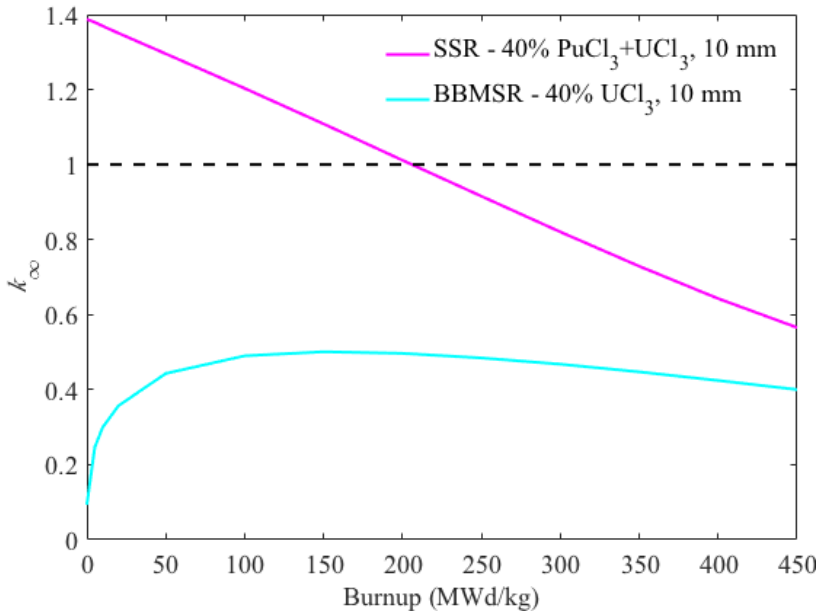

Fig. 2.2 Burnup versus k_∞ for SSR burner and initial BBMSR

the volume of fuel relative to cladding and coolant, while the pitch-to-diameter ratio of 1.0 and molybdenum cladding thickness of 0.5 mm are held constant. Figure 2.3 shows that increasing the outer diameter from 10 mm to 50 mm has a significant positive impact on the reactivity, but further increase in the diameter beyond 50 mm has a minimal effect. Since practical challenges of larger fuel tubes will likely outweigh their marginal reactivity improvement, the 50 mm diameter is used throughout the rest of this chapter. Feasible fuel geometries are investigated in thermal–hydraulic analysis in subsequent chapters.

The heavy metal density can also be improved by increasing the concentration of UCl_3 in the UCl_3–NaCl mixture from 40% to 60, 80, and 100 mole%. Figure 2.4 shows that increasing uranium concentration moderately improves neutronic performance. 100% UCl_3 is carried throughout the rest of the analysis as the hypothetical best-case fuel composition, but it is noted that the 80% composition is only slightly less reactive. The higher heavy metal loading of the 50 mm, 100% UCl_3 fuel significantly increases breeding compared to the initial configuration, but further improvement is needed to achieve criticality.

2.2.3 Comparison with B&B SFR

An SFR-type B&B composition reported in the literature is used to compare inputs and results, and to verify modelling methods. Petroski performs a cross-comparison of many combinations of fuel, coolant, and cladding material [53]. U2Zr fuel (uranium metal alloyed

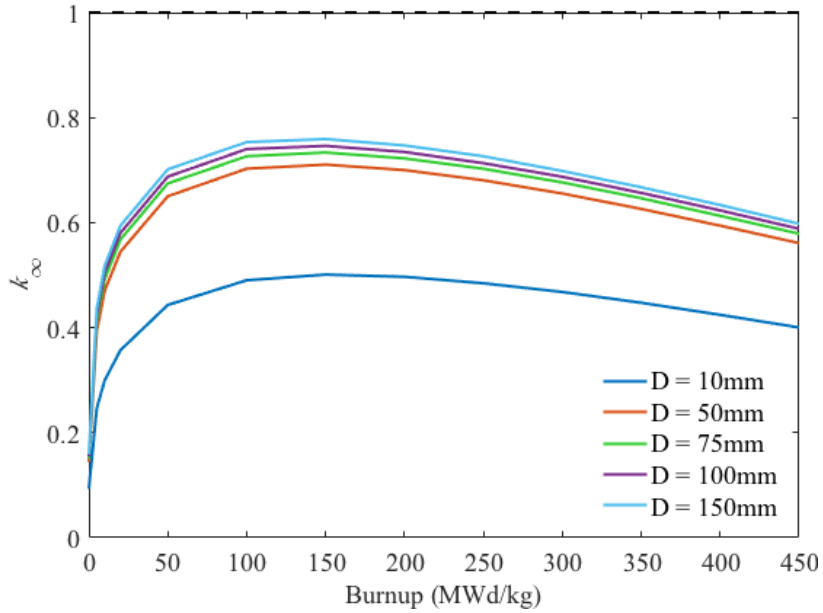

Fig. 2.3 Burnup versus k_∞ for varying fuel tube diameter with 40% UCl_3

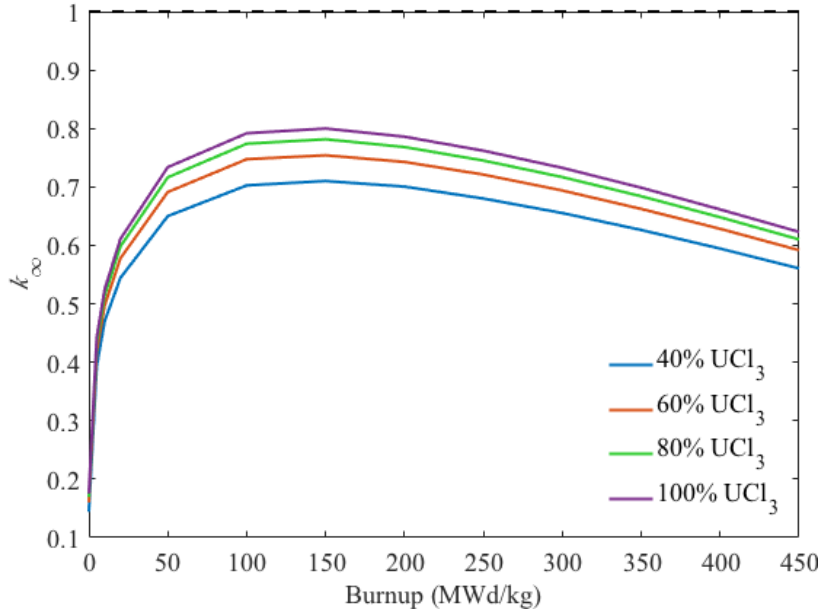

Fig. 2.4 Burnup versus k_∞ for varying UCl_3 mole% with 50 mm fuel tube diameter

with 2% zirconium), T91 steel alloy cladding, and sodium coolant are identified as the optimal combination for B&B neutronic and thermal–hydraulic performance. A major advantage of solid metallic fuel is its high heavy metal density. The homogenised mixture consisting of 75 parts fuel, 30 parts structure, and 100 parts coolant by volume will be referred to in the rest of this chapter as the BBSFR.

The BBSFR is compared with the BBMSR configuration of 50 mm and 100% UCl_3 fuel salt. Figure 2.5a shows expected burnup versus k_∞ performance for the BBSFR, where the system transitions from subcritical to supercritical early in the burnup cycle. This result confirms that the modelling inputs and methods are appropriate for evaluating B&B systems.

Figure 2.5b compares the neutron flux spectra of the two configurations, showing that the BBMSR has a significantly softer spectrum than the BBSFR, likely due to scattering and lower heavy metal density. Furthermore, the BBMSR spectrum contains many dips at high neutron energies where the BBSFR spectrum actually peaks. A softer spectrum may reduce breeding performance by increasing parasitic resonance absorption in non-fuel materials and reducing the neutron reproduction factor η, so there are fewer excess neutrons available. Resonance capture in ^{238}U can improve breeding if compensated by an increase in available neutrons. Additionally, a softer spectrum results in a reduced rate of fast fission of ^{238}U. It is noted that the magnitudes of the flux spectra are different because of the higher heavy metal density of the BBSFR system, according to

$$P = VE_f\sigma_f N\phi \tag{2.1}$$

where P is power, V is volume, E_f is the energy released per fission, σ_f is the fission cross-section of fissile isotopes, N is the density of fissile isotopes, and ϕ is flux. The two systems are modelled with equivalent power and volume, so for smaller fissile isotope density in the BBMSR, the flux must be larger.

From the comparison of BBMSR and BBSFR, it can be inferred that differences in material properties are responsible for the large disparity in neutronic performance. The differences in the flux spectra shapes indicate that the lower heavy metal density of the molten salt compared to metallic fuel is not the only source of inferior performance.

2.2.4 Neutron absorption analysis

A detailed analysis of fission and absorption by nuclides present in the system is undertaken to determine where major neutron losses occur in the BBMSR. The analysis is performed at the 150 MWd/kg burnup step, when k_∞ approaches its peak value. Serpent calculates

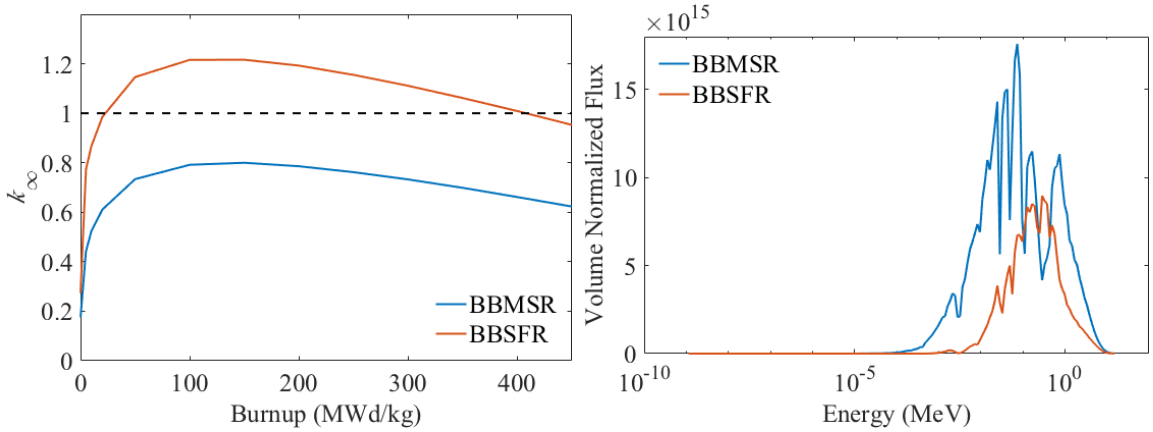

(a) Burnup versus k_∞ (b) Neutron flux spectra

Fig. 2.5 Comparison of BBSFR and BBMSR

macroscopic fission and capture cross-sections of the unit cell composition, and detectors are used to calculate fission and capture reaction rates in individual nuclides. Macroscopic cross-sections for the BBMSR and the BBSFR are given in Table 2.1, and the dominant fission and capture nuclides are listed with their respective contributions to the total cross-sections.

The BBSFR has a larger macroscopic fission cross-section Σ_f, but the main fission contributions are similar between the two systems. Fast fission of ^{238}U is slightly more likely in the BBSFR, corresponding to slightly less production of plutonium, as shown in the comparison of fuel compositions given in Table 2.2. The BBSFR also has a larger macroscopic capture cross-section Σ_c, and nearly 65% of its capture occurs in ^{238}U to breed ^{239}Pu, while only 40% of capture in the BBMSR occurs in ^{238}U. A significant portion of capture reactions in the BBMSR occurs in molybdenum, zirconium, and chlorine. This analysis suggests that the relatively soft spectrum of the molten salt system results in high parasitic neutron capture and fewer neutrons available for breeding.

One potential strategy to improve the neutron economy of the BBMSR is isotope enrichment in the low-capture nuclides of molybdenum, zirconium, and chlorine. Average capture cross-sections for all naturally occurring isotopes of molybdenum, zirconium, and chlorine are found in the ENDF/B-VII.1 data library [28] and listed in Tables 2.3 to 2.5. The thermal cross-section has been calculated by averaging the energy-dependent cross-sections over a Maxwellian spectrum at room temperature from 10^{-5} eV to 0.5 eV. The epithermal cross-section is the resonance integral at infinite dilution from 0.5 eV to 100 keV. The fast cross-section has been calculated by averaging the cross-sections over the ^{235}U fission spectrum from 1 keV to 20 MeV. According to these energy ranges, the current BBMSR configuration spans the epithermal and fast regions. Tables 2.3 to 2.5 reveal consistently small

Table 2.1 Nuclide contributions to absorption in BBSFR and BBMSR at 150 MWd/kg

	BBSFR	BBMSR
Fission: Σ_f (m^{-1})	$\mathbf{2.77 \times 10^{-3}}$	$\mathbf{1.18 \times 10^{-3}}$
^{239}Pu	78.7%	77.5%
^{238}U	15.2%	10.4%
^{240}Pu	3.5%	5.2%
^{241}Pu	1.8%	5.9%
Capture: Σ_c (m^{-1})	$\mathbf{3.91 \times 10^{-3}}$	$\mathbf{3.14 \times 10^{-3}}$
^{238}U	63.5%	39.2%
^{239}Pu	9.6%	11.1%
Nat. Mo	–	12.7%
^{240}Pu	2.5%	4.0%
Nat. Zr	0.4%	2.6%
^{35}Cl	–	2.2%

Table 2.2 Fuel compositions in BBSFR and BBMSR at 150 MWd/kg (wt%)

	BBSFR	BBMSR
^{239}Pu	9.8%	12.0%
^{238}U	88.1%	82.9%
^{240}Pu	2.0%	0.6%
^{241}Pu	0.2%	4.4%

fast capture cross-sections, but several isotopes with large epithermal capture cross-sections could cause parasitic neutron loss.

For each of the analysed elements, the nuclide with the smallest epithermal cross-section is identified: ^{37}Cl, ^{90}Zr, and ^{94}Mo. Assuming hypothetically that close to 100% enrichment is technologically possible, a "low-capture" BBMSR version using only these isotopes is modelled. Table 2.6 compares the absorption contributions of the low-capture BBMSR with the previous natural-materials BBMSR configuration. Some improvement is observed, with capture in ^{238}U increasing from 40% to 47%. The sum of capture in chlorine, zirconium, and molybdenum decreases from 17.5% to 0.7%. Figure 2.6a also shows some improvement in k_∞ for the low-capture version, but Figure 2.6b shows that the shape of the flux spectrum remains very close to that of the BBMSR materials with their natural isotopic compositions, with large flux dips at the fast energies due to scattering in fluorine.

Table 2.3 Chlorine average capture cross-sections from ENDF/B-VII.0 (barns)

Isotope	Thermal	Epithermal	Fast
35	43.6	18.0	0.00
37	0.4	0.2	0.00

Table 2.4 Zirconium average capture cross-sections from ENDF/B-VII.0 (barns)

Isotope	Thermal	Epithermal	Fast
90	0.0	0.1	0.01
91	1.2	6.0	0.01
92	0.2	0.6	0.01
93	0.7	17.8	0.01
94	0.0	0.3	0.01
95	1.2	7.6	0.02
96	0.0	5.1	0.01

Table 2.5 Molybdenum average capture cross-sections from ENDF/B-VII.0 (barns)

Isotope	Thermal	Epithermal	Fast
94	0.3	1.3	0.04
95	13.4	104.5	0.05
96	0.6	17.4	0.03
97	2.2	17.2	0.04
98	0.1	6.4	0.03
99	8.0	41.4	0.03
100	0.2	3.8	0.01

2.2.5 Spectrum hardening

Since elimination of the high-capture isotopes in Cl, Zr, and Mo does not sufficiently improve neutronic performance of the BBMSR, a separate approach to harden the spectrum is explored. Inelastic neutron scattering in the fluoride salt coolant may be significant, despite the relatively tight fuel lattice modelled. The fluoride salt coolant is replaced with the ternary chloride eutectic NaCl–KCl–$MgCl_2$ (30–20–50 mol%), which was selected for its low moderating power in the study of the flexible conversion ratio salt-cooled reactor [66]. Zr is therefore eliminated from the system, but 100% enrichment in ^{37}Cl is assumed for both fuel and coolant salts, and the cladding is modelled as 100% ^{94}Mo in the remainder of this

Table 2.6 Nuclide contributions to absorption in BBMSR with natural isotopic compositions and low-capture isotopes

	Natural	Enriched
Fission: Σ_f (m^{-1})	**1.18E–3**	**1.14E–3**
^{239}Pu	77.5%	77.7%
^{238}U	10.4%	10.0%
^{240}Pu	5.2%	5.3%
^{241}Pu	5.9%	6.0%
Capture: Σ_c (m^{-1})	**3.14E–3**	**2.56E–3**
^{238}U	39.2%	46.6%
Nat. Mo/^{94}Mo	12.7%	0.2%
^{239}Pu	11.1%	12.6%
^{240}Pu	4.0%	4.6%
Nat. Zr/^{90}Zr	2.6%	0.0%
^{35}Cl	2.2%	0.5%

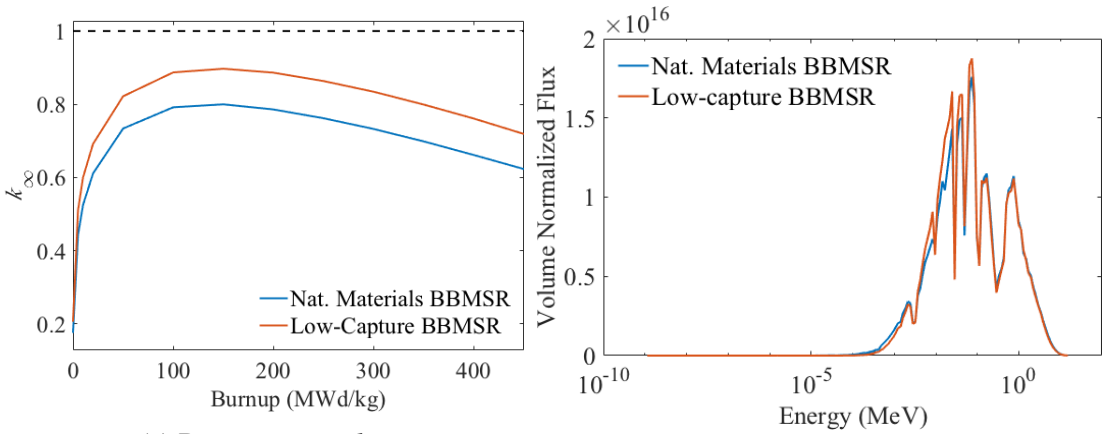

(a) Burnup versus k_∞

(b) Neutron flux spectra

Fig. 2.6 Comparison of BBMSR versions with natural isotopic compositions and low-capture isotopes

section. Figure 2.7a compares burnup versus k_∞ of the 50 mm, 100% UCl_3 BBMSR with the original fluoride coolant using low-capture isotopes, and the identical configuration with the ternary chloride coolant. The BBSFR is also included for reference. The chloride-cooled BBMSR does become supercritical, and its performance approaches that of the BBSFR despite the lower heavy metal density in molten salt versus solid metallic fuel.

The neutron spectra of these three configurations are compared in Figure 2.7b, confirming that switching from fluoride to chloride salt coolant significantly hardens the neutron spectrum by increasing flux at the higher energies. These results indicate that B&B operation in the dual-salt BBMSR configuration may be feasible with natural uranium using 100% UCl_3 fuel salt, chloride coolant, enriched ^{37}Cl and ^{94}Mo (or a more neutronically transparent cladding material), and a large fuel volume fraction. The fuel volume fraction will be limited by heat removal capabilities, so thermal–hydraulic analysis is needed determine these limits.

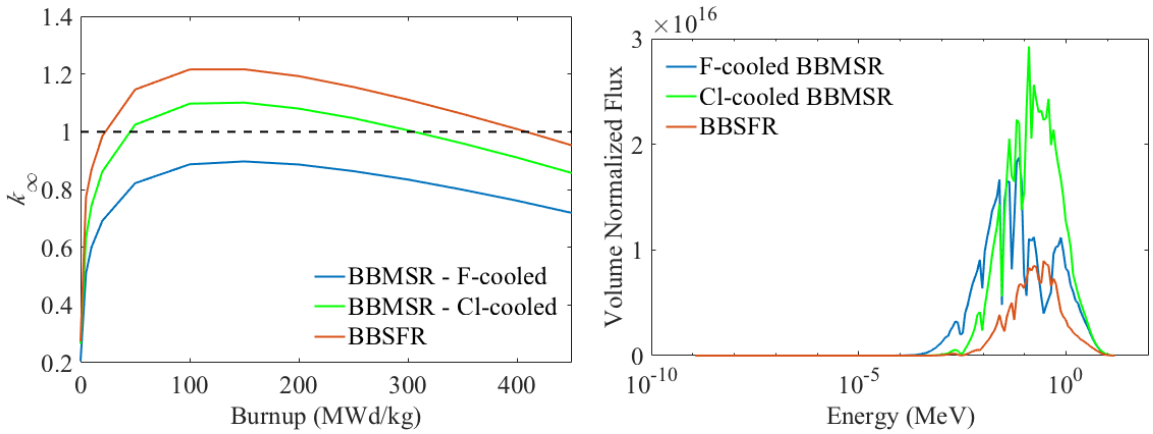

(a) Burnup versus k_∞

(b) Neutron flux spectra

Fig. 2.7 Comparison of fluoride salt-cooled BBMSR, chloride salt-cooled BBMSR, and BBSFR

2.2.6 Thorium

Thorium breeder configurations have been examined in past and current molten salt reactor research, as described in Section 1.3.1. To examine the effect of thorium on breeding performance of the BBMSR, the natural uranium in UCl_3 is replaced with ^{232}Th. Figure 2.8 shows the reactivity-burnup results of a 50 mm unit cell with 100% $ThCl_4$ fuel salt, compared to the 50 mm unit cell with 100% UCl_3 fuel. Both configurations include the ternary chloride coolant and enriched ^{37}Cl and ^{94}Mo. Thorium has a significant reactivity penalty compared to natural uranium for B&B operation, and does not become supercritical at any point in the

burnup cycle. Uranium is therefore maintained as the preferred fuel for the BBMSR, since it also has a more developed fuel cycle infrastructure compared to thorium.

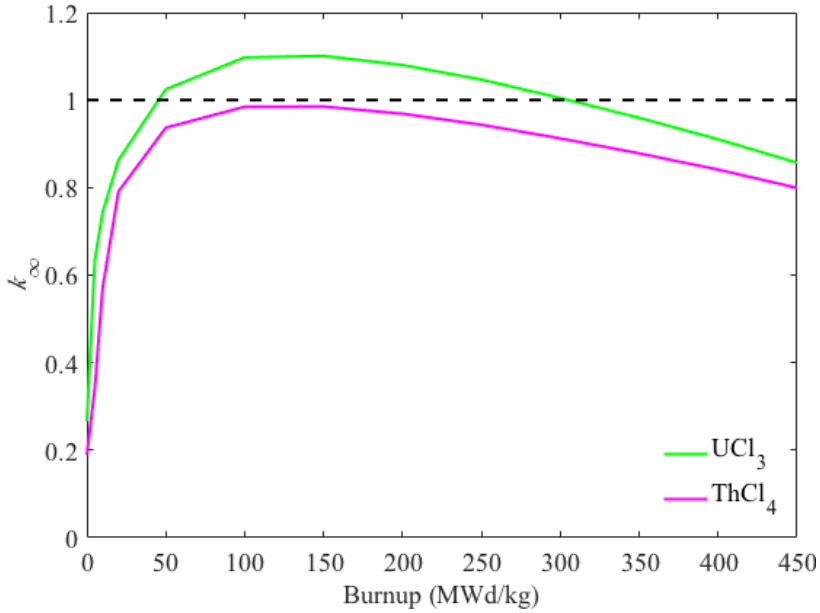

Fig. 2.8 Burnup versus k_∞ for UCl_3- and $ThCl_4$-fuelled BBMSR

2.2.7 Low-enriched uranium

Next, LEU variations on the chloride-cooled BBMSR configuration are considered to relax neutronic constraints, potentially allowing greater flexibility for thermal–hydraulic design and fuel with a lower concentration of UCl_3 for chemical stability considerations. Although use of LEU diverges from the original definition of B&B operation, it may still enable high uranium utilisation with much better proliferation resistance than the medium-enriched uranium or reprocessed plutonium required for traditional fast reactors. Enrichment levels from 5% to 20% ^{235}U are modelled to determine the effect of enrichment on k_∞ over burnup.

Figure 2.9 displays burnup versus k_∞ for the natural uranium and LEU cases, using 100% UCl_3 fuel, ternary chloride coolant, 50 mm tube diameter, ^{37}Cl in both fuel and coolant, and ^{94}Mo cladding. The natural uranium version shows the typical B&B breeding behaviour described in Section 2.2.2. Increasing enrichment increases the initial k_∞, but the long-term behaviour converges for all the configurations containing up to 20% ^{235}U. The 20% enriched version shows nearly linear burnup behaviour, similar to LWR fuel which primarily burns ^{235}U. However, since the BBMSR is configured for efficient breeding of ^{239}Pu from ^{238}U, the slope of its k_∞ curve is significantly flatter than that of an LWR.

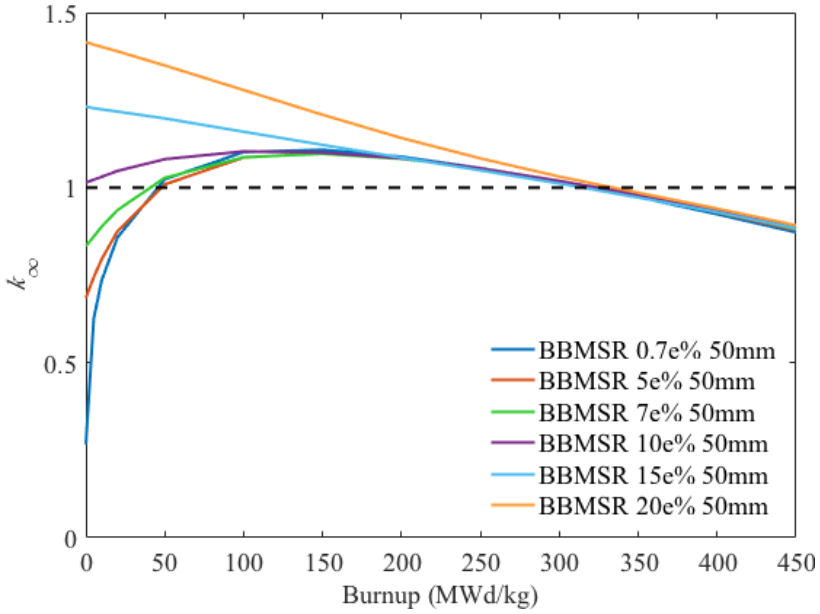

Fig. 2.9 Burnup versus k_∞ for varying enrichment

The 20% enriched version is also used to demonstrate the effect of tube diameter in the improved BBMSR. Figure 2.10 shows that for decreasing fuel tube diameter, k_∞ decreases but the burnup trend is similar. The natural uranium BBMSR with 50 mm tube diameter is also included for comparison. These results indicate that the enrichment can be adjusted to tune the initial reactivity, while the tube diameter can be adjusted to tune the average excess reactivity and discharge burnup.

A final comparison between the BBMSR and Moltex SSR is presented to demonstrate that the modifications described in this section significantly improve neutron economy. Figure 2.11 shows burnup versus k_∞ of the SSR and the BBMSR with 20% enriched uranium and 30 mm tube diameter, since this configuration has initial k_∞ closest to that of the SSR. The BBMSR has a significantly flatter burnup curve due to its harder spectrum which improves breeding performance.

2.3 Materials Feasibility Discussion

The use of chloride fuel salt with enriched ^{37}Cl is a common feature among B&B MSR designs [42, 26]. The BBMSR additionally requires pure (or high concentration) UCl_3 fuel salt and a chloride coolant salt to support B&B operation. Significant uncertainty in the thermophysical and chemical properties of the chloride fuel and coolant salts remains. This

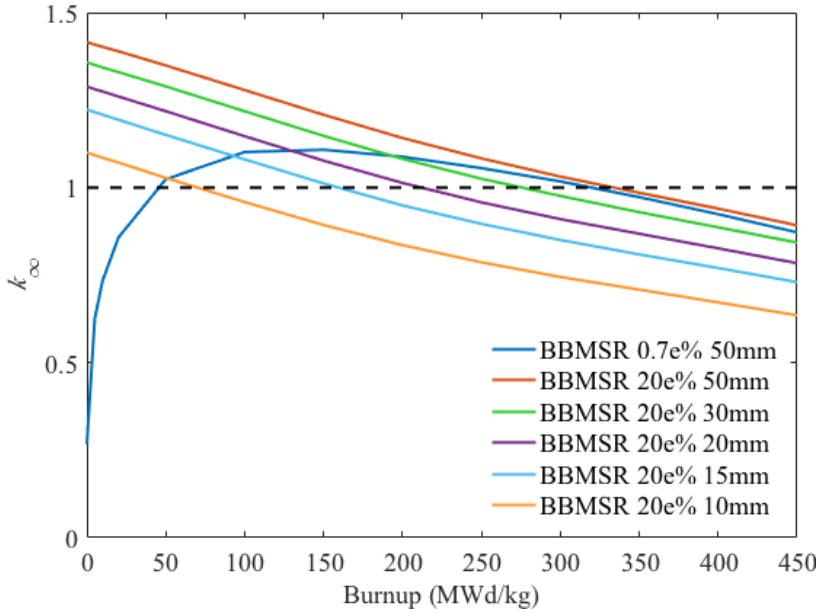

Fig. 2.10 Burnup versus k_∞ for varying tube diameter

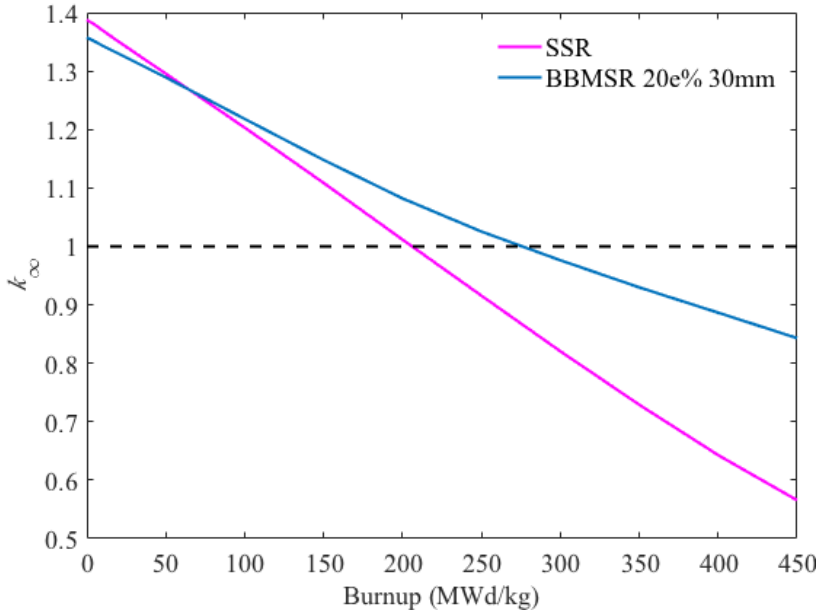

Fig. 2.11 Burnup versus k_∞ for BBMSR vs Moltex SSR

section discusses some known characteristics and open questions regarding the use of these salts.

In addition, the neutronic feasibility study indicates that enrichment in ^{94}Mo may be needed to avoid high parasitic absorption in the BBMSR cladding, which may be achievable with recent advances in enrichment processes. Separation of Isotopes by Laser Excitation (SILEX) is a modern laser-enrichment technology that can be used for cost-effective isotope separation of uranium as well as chlorine and molybdenum [84]. However, alternative cladding materials are also identified in this section.

2.3.1 Ternary chloride coolant salt

The ternary chloride salt adopted as the BBMSR coolant was previously identified in the design of the flexible conversion ratio salt-cooled reactor, for which a detailed screening of numerous fluoride and chloride salts was performed [76]. Chloride salts were found to be neutronically superior because of their lower moderating power and smaller coefficient of thermal expansion, which were particularly important for mitigation of the positive coolant temperature coefficient. In addition, chloride salts also enable better thermal–hydraulic performance due to low viscosities. Salts containing lithium were eliminated because of the need to enrich in ^{7}Li to avoid high parasitic absorption in ^{6}Li. Of the remaining candidate salts, the ternary mixture NaCl–KCl–$MgCl_2$ (30–20–50 mol%) was selected for its low melting point of 396°C. These selection criteria are highly relevant for the BBMSR coolant, so the adoption of the same coolant salt is justified. The salt's properties, together with a discussion of uncertainties, are summarised in ref. [52]. These properties reproduced in Table 2.7.

The selected coolant salt is reported to be chemically compatible with common structural materials. Absorption in ^{35}Cl and ^{39}K produces the radioisotope ^{36}Cl, and venting of gaseous fission products to the coolant in the BBMSR will also contribute to activation of the coolant. Low-level radioactivity in the coolant is expected to be manageable for both refuelling and decommissioning [76, 60].

2.3.2 Uranium chloride fuel salt

While it is possible to operate an MSR in the fast spectrum using a fluoride fuel salt — for example, the GIF-endorsed Molten Salt Fast Reactor is fuelled with a thorium fluoride — chloride salts have numerous advantages for fast MSR design. Higher actinide and lanthanide solubility and lower moderating power in chloride salts help to achieve high fuel loading and

a hard spectrum. Lower viscosities in chlorides enhance thermal–hydraulic performance, and particularly in the BBMSR, this characteristic reduces the resistance to natural circulation of the fuel within tubes.

100% UCl_3 is selected as the BBMSR fuel to satisfy the need for high fissile loading to support B&B operation, but it will require management of challenging thermal–hydraulic and chemical behaviour. Figure 2.12, a phase diagram for the mixture of UCl_3 and NaCl, shows that 100% UCl_3 melts at 850°C whereas the eutectic with 32% UCl_3 melts at 520°C, so the BBMSR system will need to operate at high temperatures to maintain the fuel in its molten state. However, some freezing in the fuel may not be detrimental to overall operation, unlike in pool-type reactors where salt freezing can block critical flow pathways. If small amounts of carrier salt are needed to satisfy thermal–hydraulic and chemical requirements, Figure 2.4 shows that a mixture of UCl_3–NaCl (80–20%) may have similar neutronic performance to the 100% UCl_3 fuel. A mixture of UCl_3 and UCl_4 may also be a feasible way to achieve more manageable fuel properties without the use of a carrier salt. UCl_3 is less corrosive and allows a higher heavy metal density, but a small addition of UCl_4 lowers the melting point of the mixture. A small UCl_4 content may also suppress precipitation of fission products out of the fuel salt, especially at high burnup when fission products accumulate [48]. Further consideration of fuel salt mixtures is reserved for future studies, and only 100% UCl_3 is analysed in the rest of this thesis.

Although chloride fuel salts are gaining popularity for fast MSR design, especially within the B&B space, the property databases for these salts are largely incomplete or outdated. For instance, an experimental study dating from 1975 [8] is most commonly used as the source for density and viscosity of UCl_3–NaCl, in this thesis and in numerous other recent studies of fast MSR systems. While some gaps remain in the fluoride salt property databases, they are significantly more established than those for chloride salts, owing to the emphasis on fluorides in historical MSR development. Modern measurements of fluoride and chloride salt properties are underway in national laboratories, universities, and private companies around the world.

The physical properties that have been used for modelling 100% UCl_3 molten salt in this thesis are listed in Table 2.8. Thermal–hydraulic analysis reported in subsequent chapters has been performed assuming constant properties evaluated at a temperature of 1000°C, or 1273 K, except where noted otherwise. The density and viscosity correlations are taken from the previously mentioned 1975 study [8]. Specific heat capacity is reported in ref. [5] with the caveat, "the data for the liquid phase of UCl_3 have been estimated by comparison to the data for the early lanthanide trichlorides." Thermal conductivity data for actinide chlorides

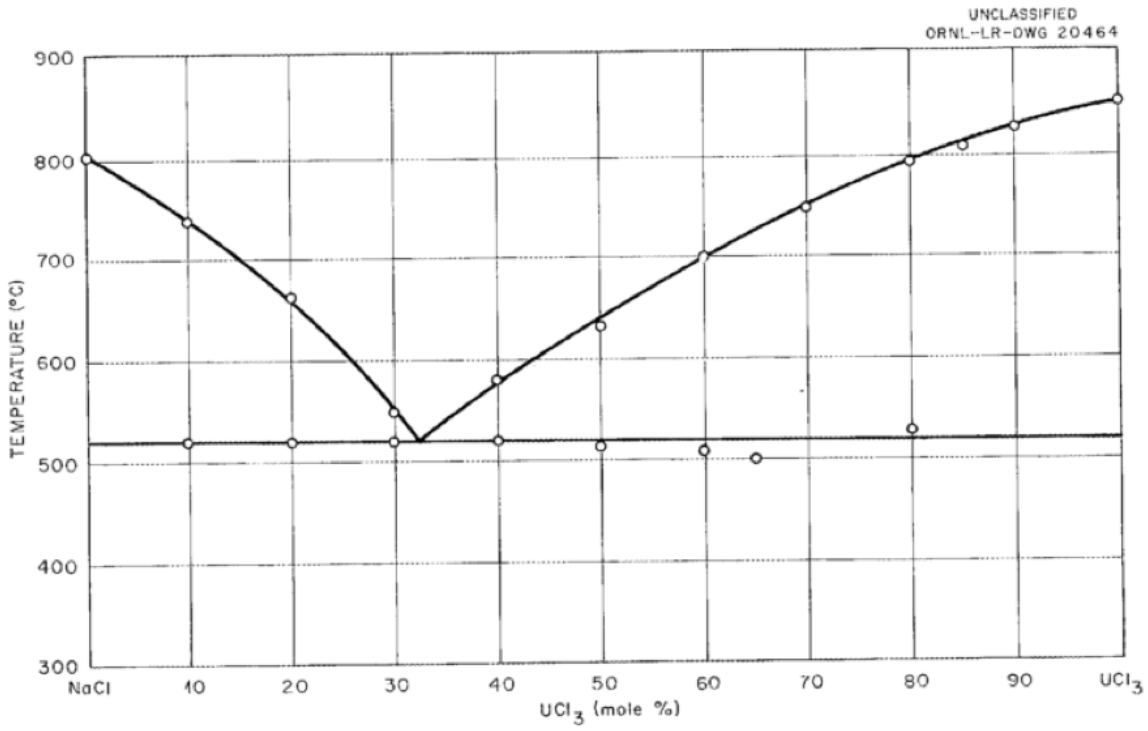

Fig. 2.12 NaCl–UCl_3 Phase diagram from ref. [73]

is particularly lacking. A conductivity of 0.7 W/mK is reported for $PuCl_3$–NaCl (16–84%) at 750°C, but since NaCl likely enhances the thermal conductivity of lanthanide chloride mixtures, the value is rounded down to 0.5 W/mK for the present study [69, 48]. This conservative assumption is further supported by Figure 2.13 from a 1982 study, which shows thermal conductivity as a function of temperature for several individual salts, with UCl_4 starting at 0.375 W/mK at 600°C but increasing rapidly with temperature [48]. The melting point of UCl_3 is reported experimentally in ref. [73], but the boiling point is extrapolated from the temperatures corresponding to measured vapour pressures, up to a vapour pressure of 1 atmosphere [48].

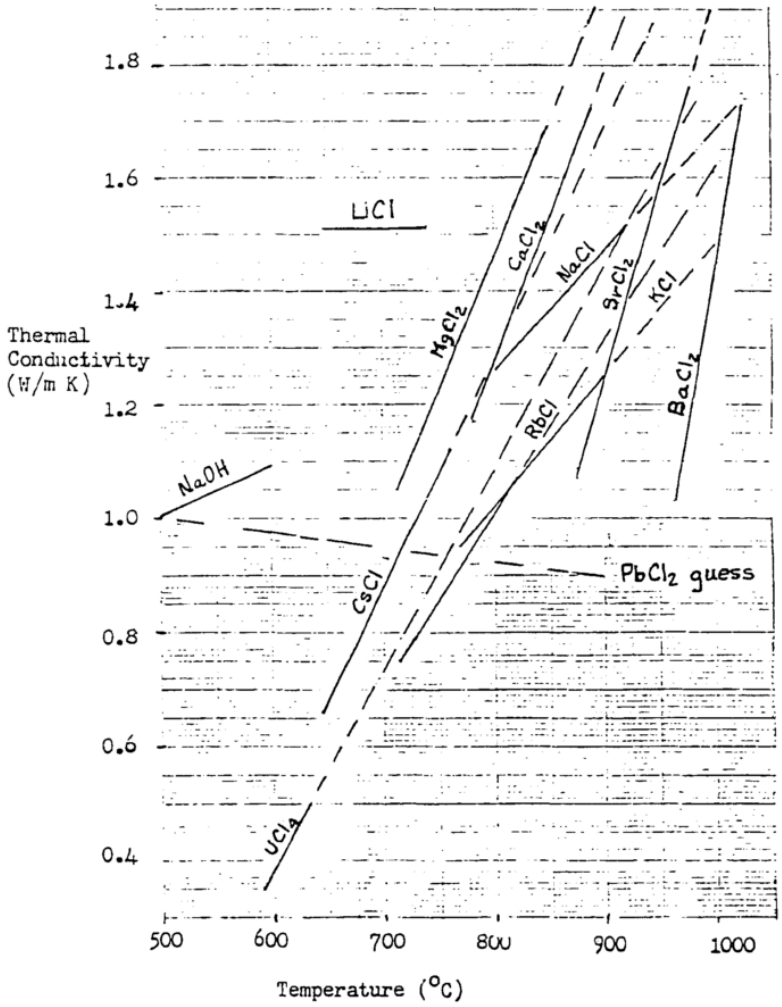

Fig. 2.13 Thermal conductivity of individual salts, from ref. [48]

Table 2.7 Thermophysical properties of NaCl–KCl–$MgCl_2$ (30–20–50 mol%) from ref. [52]

Property	Equation/Value	Unit
Melting temperature, T_l	669	K
Boiling temperature, T_b	2773	K
Density, ρ	$2472 - 0.778(T[\mathrm{K}])$	kg m^{-3}
Specific heat capacity, c_P	1004	J(kg K)$^{-1}$
Dynamic viscosity, μ	$\exp(3040/(T[\mathrm{K}]) - 2.96)$	kg(ms)$^{-1}$
Thermal conductivity, κ	0.39	W(mK)$^{-1}$

Table 2.8 Thermophysical properties of UCl_3

Property	Equation	Value (at 1273 K)	Unit	Uncertainty	Source
Melting temperature, T_l	–	1073	K	Low	[73]
Boiling temperature, T_b	–	2023	K	Medium	[48]
Density, ρ	$6374.7 - 1.5222(T[\mathrm{K}])$	4436.94	kg m^{-3}	Low	[8]
Specific heat capacity, c_P	–	435.6	J(kg K)$^{-1}$	Medium	[5]
Kinematic viscosity, ν	$10^{-1.2213+1100/(T[\mathrm{K}])} \times 10^{-6}$	4.39 E-7	m^2 s^{-1}	Low	[8]
Thermal conductivity, κ	–	0.5	W(mK)$^{-1}$	High	[69]*
Thermal expansion coeff., β	–	3.43 E-4	K^{-1}	Low	Calculated
Prandtl number, Pr	ν/α	1.70	–	Medium	Calculated

* Adjusted

2.3.3 Candidate cladding materials

Based on the neutronic requirement of high actinide loading, it can be estimated that the operating fuel temperature of the BBMSR will be higher than 800°C, corresponding to the melting temperature of the 80% UCl_3 mixture (from Figure 2.12). A cladding material is therefore needed that can withstand high temperatures in addition to fast neutron fluence and corrosion by molten salts. The predicted ease of transferring the fuel to new cladding could relax these requirements, but the cladding lifetime in the reactor must still be long enough to produce sufficient cycle length for economic reactor operation.

Molybdenum (Mo) exhibits excellent resistance to high temperatures, irradiation, and corrosion. However, use of natural isotopic Mo cladding in the BBMSR produces a high rate of parasitic neutron absorption, so enrichment in ^{94}Mo is needed. In addition, manufacturing methods for Mo cladding are not yet developed, so alternative cladding materials are considered here.

Stainless steel is also relatively resistant to corrosion, high temperatures, fast neutron fluence, and mechanical stresses [76]. It is commonly used in fast reactor designs, and it is proposed for use in the SSR where zirconium in the coolant salt ZrF_4–NaF–KF automatically maintains the required chemistry to avoid excessive corrosion by the molten salts [60]. The common high temperature-resistant austenitic stainless steel type 310 (SS310) is considered in this thesis.

Silicon carbide (SiC) is a promising advanced cladding material that can allow higher operating temperatures and higher burnups than conventional claddings. Experimental data suggest that SiC can exhibit low corrosion rates and high stability to fast neutron fluence [83]. Although SiC has a low neutron capture cross-section and low activation, it may soften the reactor flux spectrum, so its suitability for the BBMSR will depend on the relative density of cladding needed in the system. Its superior strength at high temperatures and high neutron fluence may allow for thinner cladding, especially when combined with venting technology to relieve pressure in the fuel element [82]. While SiC cladding is not yet a mature technology, it is becoming increasingly popular in advanced reactor and accident-tolerant LWR designs, so full characterisation and development of fabrication methods are underway [18]. A potential weakness of SiC cladding is that its thermal conductivity deteriorates after irradiation; however, this effect is less pronounced when irradiation occurs at high temperature, as would be the case in the BBMSR [68].

Key properties of the three cladding materials are summarised in Table 2.9. The post-irradiation thermal conductivity of SiC remains comparable to the conductivity of the metals. Cladding temperature limits vary for different reactor systems, since they are dependent on

numerous phenomena. In other fast reactors, the allowable cladding temperature is typically limited to far less than the melting temperature of the material, for varying reasons such as eutectic formation, impaired corrosion resistance, or increased creep damage rate beyond a certain temperature. The BBMSR cladding temperature limit would likely be affected by the temperature at which corrosion and irradiation resistance diminish; experimental research is needed to determine these limits. Table 2.9 includes only melting temperatures of the materials for comparison. Detailed comparison of the neutronic impact of these cladding materials in the BBMSR is reserved for further neutronic analysis in Chapter 5.

Table 2.9 Properties of candidate cladding materials

	Mo	SS310	SiC
Density (g/cm^3)	10.22	8.03	3.21
Melting temperature (°C)	2623	1400	2545
Thermal conductivity (W/mK)	138	19	30*
Source	[29]	[74]	[68]

* Thermal conductivity of SiC after irradiation at $T_{irr} > 800$°C

Chapter 3

Fuel Convection Analysis

The BBMSR fuel salt circulates only by natural convection and is contained within individual tubes that are cooled externally. A key design challenge is to ensure sufficient heat transfer from the fuel to coolant to avoid localised fuel boiling and weakening of the cladding. The neutronic feasibility assessment indicated that B&B operation with natural uranium feed fuel may be achievable with a large fuel volume fraction, but the fuel configuration is limited by the system's thermal–hydraulic characteristics. Because molten salts have low thermal conductivities relative to solid nuclear fuels, the fuel tubes would be limited to very small diameters if the fuel were stagnant.

Natural circulation within the fuel tubes may sufficiently enhance heat transfer to the coolant to allow the high fuel volume fraction required for B&B operation and economically competitive power density. The physical phenomena involved in a buoyant, heat-generating fluid are unusual and complex, and existing heat transfer correlations have limited applicability in this domain. This chapter explores heat transfer behaviour in convection of a fluid with internal heat generation, and develops an innovative method for thermal–hydraulic analysis of the BBMSR fuel.

3.1 Analytical Convection Model

A first approximation of the fuel's thermal–hydraulic behaviour is made by mathematically deriving an analytical solution for laminar, incompressible flow in a two-dimensional parallel channel with buoyancy, uniform internal heat generation, and uniform cooling flux at the walls. Previous analysis and experimental studies of natural convection in heat-generating fluids show that the hot core rises while the cooler annulus descends [33, 67]. In short cells, the annulus grows from the bottom to the top, while in cells of large length-to-width

ratio, the end effects become relatively unimportant and the annulus evolves to a constant thickness [41].

The analytically modelled channel is illustrated in Figure 3.1, where x is the distance from the vertical axis, y is the distance from the lower end of the channel, and D is the width of the channel. The wall temperature boundary condition T_{Wall} varies along the channel length, while v is always zero at the wall. It is assumed that the channel is infinitely long, so that the temperature and velocity profiles, $T(x) - T_{Wall}$ and $v(x)$ respectively, are fully developed and independent of y. The channel ends are closed, so the flow reverses at the ends to satisfy mass conservation. The velocity and temperature distributions are physically coupled, so the Navier–Stokes equations for momentum and energy must be mathematically coupled.

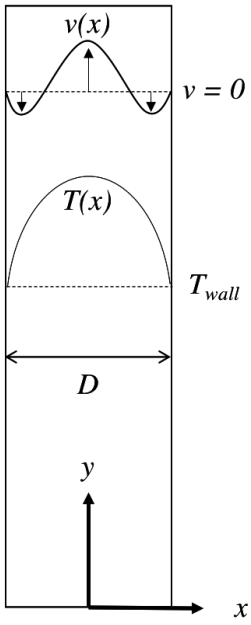

Fig. 3.1 Parallel channel for analytical model

Momentum:

The Navier–Stokes momentum equation in the y direction is:

$$\rho\left(u\frac{\partial v}{\partial x}+v\frac{\partial v}{\partial y}\right)=-\frac{\partial p}{\partial y}+\mu\left(\frac{\partial^2 v}{\partial x^2}+\frac{\partial^2 v}{\partial y^2}\right)-\rho g \tag{3.1}$$

where $u =$ velocity in the x direction, $v =$ velocity in the y direction, $p =$ pressure, $\mu =$ dynamic viscosity[1], $\rho =$ density, and $g =$ acceleration due to gravity.

The Boussinesq approximation is frequently applied for buoyancy-driven, incompressible flow. It neglects property variations except where density is multiplied by g, and it approximates the density variation with a simplified equation of state,

$$\rho \simeq \rho_0[1-\beta(T-T_0)] \tag{3.2}$$

where ρ_0 is the fluid density at a reference temperature T_0, ρ is the density at the local temperature T, and β is the volumetric coefficient of thermal expansion. The Boussinesq approximation is valid when $\beta(T-T_0) << 1$ [4]. Assuming this condition holds true for the convecting fuel problem and recognising $-\partial p/\partial y = \rho_0 g$, Equation 3.1 is simplified as:

$$\rho\left(u\frac{\partial v}{\partial x}+v\frac{\partial v}{\partial y}\right)=\mu\left(\frac{\partial^2 v}{\partial x^2}+\frac{\partial^2 v}{\partial y^2}\right)+\rho_0 g\beta(T-T_0) \tag{3.3}$$

with constant β, μ, T_0, and ρ_0; and $T = T(x) - T_{Wall}$. For the closed system in the present analysis, T_0 must be found such that mass continuity is satisfied. As demonstrated later in this section, T_0 is the temperature occurring at the velocity inflection points, so the velocity direction is positive when $T > T_0$ and negative when $T < T_0$.

Equation 3.3 can be further simplified, since $u = 0$; $\partial v/\partial y = 0$; and $\partial^2 v/\partial y^2 = 0$ in fully developed flow:

$$\frac{\partial^2 v}{\partial x^2} = -\frac{\rho_0 g\beta}{\mu}(T-T_0) \tag{3.4}$$

Energy:

For an incompressible fluid with constant thermal diffusivity $\alpha = \kappa/(\rho c_P)$, constant specific heat capacity c_P, and uniform volumetric heat generation rate q''', the temperature distribution T is described by the energy balance:

$$u\frac{\partial T}{\partial x}+v\frac{\partial T}{\partial y}=\alpha\left(\frac{\partial^2 T}{\partial x^2}+\frac{\partial^2 T}{\partial y^2}\right)+\frac{q'''}{\rho_0 c_P} \tag{3.5}$$

[1]The dynamic viscosity (μ) is calculated from reported kinematic viscosity (ν) data as $\mu = \nu\rho$.

In fully developed flow, $u = 0$, and $\partial^2 T/\partial y^2 \approx 0$ since axial conduction can be neglected relative to horizontal conduction. Equation 3.5 thus reduces to:

$$\frac{1}{\alpha}\left(v\frac{\partial T}{\partial y} - \frac{q'''}{\rho_0 c_P}\right) = \frac{\partial^2 T}{\partial x^2} \tag{3.6}$$

It is assumed that $\partial T/\partial y$ is dependent only on the coolant parameters at the wall:

$$\frac{\partial T}{\partial y} = \frac{2q''}{(\rho_0 \bar{v} c_P D)_{coolant}} \tag{3.7}$$

where $D_{coolant}$ is the hydraulic diameter of the coolant channel, and all heat generated within the modelled channel is assumed to be removed by conduction at the wall, so $q'' = q'''D$.

General velocity derivation:

An expression for $\partial^2 T/\partial x^2$ is found by differentiating Equation 3.4 twice, and it is substituted in for the right side of Equation 3.6 to obtain:

$$\frac{1}{\alpha}\left(v\frac{\partial T}{\partial y} - \frac{q'''}{\rho_0 c_P}\right) = -\frac{\mu}{\rho_0 g\beta}\cdot\frac{\partial^4 v}{\partial x^4} \tag{3.8}$$

Since $\partial T/\partial y$ is a constant, $(T - T_{Wall})$ and v are only functions of x, so Equations 3.4 and 3.8 can be rewritten as ordinary differential equations:

$$T(x) = T_{Wall} + T_0 - \frac{\mu}{\rho_0 g\beta}\frac{d^2 v}{dx^2} \tag{3.9}$$

$$\frac{\mu}{\rho_0 g\beta}\cdot\frac{d^4 v}{dx^4} + \frac{1}{\alpha}\frac{\partial T}{\partial y}\cdot v - \frac{q'''}{\alpha\rho_0 c_P} = 0 \tag{3.10}$$

Equation 3.9 represents the general temperature solution, but Equation 3.10 must be rearranged to obtain the general velocity solution. The physical constants can be grouped into mathematical terms,

$$A = \frac{\mu}{\rho_0 g\beta},\ B = \frac{1}{\alpha}\frac{\partial T}{\partial y},\ C = \frac{q'''}{\kappa}$$

where thermal conductivity $\kappa = \alpha\rho_0 c_P$, leaving the simplified ordinary differential equation

$$A\frac{d^4 v}{dx^4} + Bv - C = 0 \tag{3.11}$$

for which a general solution $v(x)$ is given by the sum of the complementary function $v_c(x)$ and particular integral $v_p(x)$:

$$v_c(x) = c_1 e^{\lambda_1 x} + c_2 e^{\lambda_2 x} + c_3 e^{\lambda_3 x} + c_4 e^{\lambda_4 x} \tag{3.12}$$

$$v_p(x) = \frac{C}{B} \tag{3.13}$$

The exponents of the complementary solution are of the form:

$$\lambda_1 = \sqrt[4]{\frac{B}{A}}, \quad \lambda_2 = -\sqrt[4]{\frac{B}{A}}, \quad \lambda_3 = i\sqrt[4]{\frac{B}{A}}, \quad \lambda_4 = -i\sqrt[4]{\frac{B}{A}}$$

The complex exponentials in $v_c(x)$ are transformed using trigonometric identities, and the general velocity solution is rewritten as:

$$v(x) = e^{\omega x}(j_1 \cos \omega x + j_2 \sin \omega x) + e^{-\omega x}(j_3 \cos \omega x + j_4 \sin \omega x) + \frac{C}{B} \tag{3.14}$$

with the constant

$$\omega = \sqrt{\frac{1}{2}} \left(\frac{B}{A}\right)^{\frac{1}{4}}$$

Boundary conditions:

1. Assuming symmetry of the velocity function, at the centreline $(x = 0)$,

$$\left.\frac{dv}{dx}\right|_{x=0} = 0 \tag{3.15}$$

2. Assuming symmetry of the temperature function and recalling Equation 3.9,

$$\left.\frac{dT}{dx}\right|_{x=0} = \left.\frac{d^3 v}{dx^3}\right|_{x=0} = 0 \tag{3.16}$$

3. Assuming the no-slip condition at the wall, $x = D/2$,

$$v(D/2) = 0 \tag{3.17}$$

4. From Equation 3.9, where $T(D/2) = T_{Wall}$,

$$\left.\frac{d^2v}{dx^2}\right|_{x=D/2} = -\frac{\rho_0 g\beta}{\mu}(T_{Wall} - T_0) \tag{3.18}$$

5. The reference temperature T_0 satisfies the mass continuity condition such that,

$$\int_0^{D/2} v(x)dx = 0 \tag{3.19}$$

Solution:

The integral and the first, second, and third derivatives of Equation 3.14 are obtained to apply the five boundary conditions. The unknown constants j_1–j_4 of the general velocity equation (Equation 3.14) and T_0 of the general temperature equation (Equation 3.9) can thus be solved.

$$j_1 = j_3 = \frac{-C/B - 2j_2L}{2M} \tag{3.20}$$

$$j_2 = -j_4 = \frac{C/B(-2\gamma \cdot M + N + P)}{-2LN - 2LP + 2MP - 2MN} \tag{3.21}$$

$$T_0 = T_{Wall} + \theta \tag{3.22}$$

where the following mathematical terms are used for clarity:

$$\gamma = \omega \cdot \frac{D}{2} \tag{3.23}$$

$$L = \sin\gamma \cdot \sinh\gamma \tag{3.24}$$

$$M = \cos\gamma \cdot \cosh\gamma \tag{3.25}$$

$$N = \cos\gamma \cdot \sinh\gamma \tag{3.26}$$

$$P = \sin\gamma \cdot \cosh\gamma \tag{3.27}$$

$$\theta = 2\omega^2[-2j_1 \cdot L + 2j_2 \cdot M] \tag{3.28}$$

Figure 3.2a shows a representative temperature profile given by Equation 3.9, as the difference between $T(x)$ and T_{Wall}. The markers designate the position where the reference temperature $(T_0 - T_{Wall})$ occurs. Figure 3.2b shows a representative velocity profile given by Equation 3.14, with markers designating the inflection points where the flow reverses

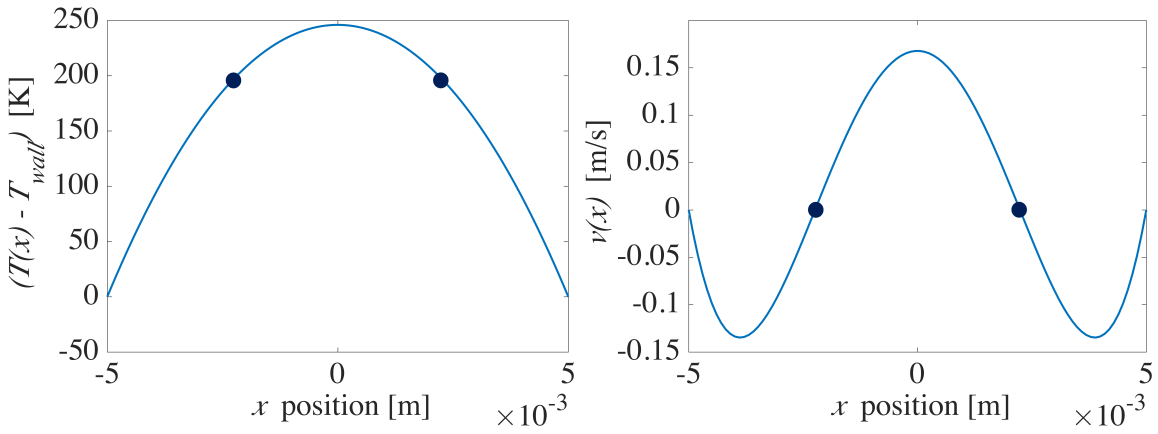

(a) Temperature

(b) Velocity

Fig. 3.2 Representative output from analytical convection model

direction. The x-position of the velocity inflection points coincides with the location of the temperature $(T_0 - T_{Wall})$.

3.2 Concentric Fuel Concept

The analytical solution illustrates the expected natural convection behaviour in the fuel tube. In principle, there is a continuous flow pattern over the length of the tube, and the internal fluid boundary has a fixed position at the velocity inflection point. However, an inflection point in the velocity profile is destabilising and can lead to turbulence even at low Reynolds number [58]. Any flow instability or stagnation effect could produce different types of convective flow. For instance, the internal flow boundary may shift from its calculated position, or multicellular convection patterns may develop, especially in such a high aspect ratio system [36]. These conditions can significantly and unpredictably localize heat transfer and deteriorate the heat transfer coefficient of the fuel, with adverse effects on the safety and reliability performance of the reactor.

Modelling assumptions could also result in inaccurate calculation of the internal boundary position. A potentially significant limitation of the analytical model is the assumption that all heat generated in a given cross-section is conducted out at the wall, thus neglecting axial convection heat transfer. These physical instabilities and modelling approximations can lead to high uncertainty in the fuel safety case.

To promote stability of the natural convection pattern in the fuel tube, an internal wall is added as a physical barrier separating the ascending core and the descending annulus flow

sections. Although buoyancy remains the only flow driver in this concentric tube configuration, the flow moves into the forced convection regime because the global temperature difference between the ascending core and the descending annulus sections induces an external pressure gradient at the inlet and outlet of each section. With sufficiently strong internal heat generation, the wall-to-bulk temperature differences within each fuel section may also induce local buoyancy effects that distort the velocity profile. Together, the local and global buoyancy effects produce a mixed convection condition in each tube section.

In this chapter the inner fuel channel will be referred to as section A, and the outer annulus as section B. The section sizes are related by a parameter ε, the ratio of section A cross-sectional area to total fuel pipe area, as

$$r_A = \frac{\sqrt{\varepsilon D^2}}{2} \tag{3.29}$$

$$r_B = \frac{D}{2} - r_A - t_w \tag{3.30}$$

where t_w is the thickness of the inner wall between A and B; r_A is the radius of section A; and r_B is the annular thickness of section B, i.e., the distance between inner wall and outer cladding. The section hydraulic diameters are $d_A = 2r_A$ and $d_B = 2r_B$, respectively. In addition to the overall fuel diameter D, ε is a design parameter that can be tuned for optimal heat transfer from fuel to coolant.

The velocity in section A, v_A, is positive, while the section B velocity, v_B, is negative, and overall mass continuity is satisfied by

$$v_B = -v_A \cdot \frac{A_A}{A_B} \tag{3.31}$$

where A_A and A_B are the respective cross-sectional areas.

Since the location of the boundary between the flow sections is fixed and predetermined in the concentric fuel concept, a numerical finite-difference approach can be used to model the axial and radial exchange of energy in the fuel tube, as an alternative to the highly simplified analytical derivation. The mass flow rate and axial bulk temperature profile in each fuel section can be determined using correlations for pressure drop and heat transfer. First, existing heat transfer correlations are qualitatively evaluated to assess their suitability for the concentric fuel concept.

3.2.1 Comparison of convection heat transfer correlations

In internal mixed convection, the heat transfer coefficient may be increased or decreased by up to one order of magnitude compared to forced convection [1]. The effect on heat transfer depends on whether buoyancy is aiding or opposing the direction of forced convection, and whether the flow is laminar or turbulent. In laminar flow, aiding mixed convection enhances heat transfer, while the converse is true for opposing mixed convection. In turbulent aiding mixed convection, heat transfer is impaired, while in turbulent opposing mixed convection, heat transfer is enhanced compared to pure forced or pure natural convection. A transition to turbulence occurs at much lower critical values of Grashof and Reynolds numbers than for either of the pure convection conditions [30].

While numerous heat transfer correlations have been successfully developed for mixed convection with external wall heating, new, tailored models are needed for convection with internal heat generation (IHG), as seen in the BBMSR concentric fuel. Prior studies report the complex and unique heat transfer characteristics of forced and natural convection in fluids with IHG. Simulated and observed phenomena include unstable thermal stratification, turbulence at low Rayleigh number, and oscillating temperature and velocity fields [63, 85, 54]. A modelled natural circulation loop with IHG predicts nearly uniform radial temperature profiles and higher buoyant velocities than with wall heating alone [32]. Using a predefined laminar velocity profile it can be shown analytically that for some systems with large IHG, steady-state flow cannot be established, and negative Nusselt numbers may also occur with large IHG [14]. These findings indicate that the characteristics of a flow with distributed heat source depart significantly from the heat transfer theory and correlations developed for externally heated flows.

Existing mixed convection theory can, however, be used to inform the choice of convection correlations for estimating BBMSR fuel temperatures. Laminar and turbulent forced convection heat transfer coefficients are qualitatively compared with laminar and turbulent mixed convection with IHG, so four regimes are considered altogether for each fuel section. As mentioned above, turbulence increases the heat transfer coefficient compared to laminar flow, while mixed convection may increase or decrease heat transfer depending on the direction and conditions of flow [30]. Based on this established knowledge, the four regimes can be arranged in order of increasing heat transfer coefficient. (Prior studies indicate that IHG improves the heat transfer coefficient compared to external heating; since the extent of improvement is not yet known, mixed convection with IHG can be conservatively treated like mixed convection with external heating, for the purposes of the regime comparison.)

Figure 3.3 shows the four regimes of convection heat transfer, arranged in order from smallest to largest heat transfer coefficient for ascending flow. Although the flow in section A of the concentric fuel may be either laminar or turbulent, depending on the fuel's fluid properties and geometry, the transition to turbulence is difficult to predict in mixed convection. Given this uncertainty, the laminar correlations will produce a more conservative fuel design, so the turbulent categories are eliminated. There are no existing correlations for laminar mixed convection with IHG, but the laminar forced convection coefficient ($Nu = 4.36$) may be overly conservative and constrain the fuel design excessively. CFD should therefore be included in the modelling methodology for the concentric fuel, to develop a new heat transfer correlation for ascending pipe flow including the effects of buoyancy and IHG.

Fig. 3.3 Heat transfer correlation selection for fuel section A, ascending core

To select a heat transfer coefficient for section B, Figure 3.4 organises the convection heat transfer regimes in order from smallest to largest for descending flow. Instability is highly likely when the direction of flow opposes the buoyancy force, so section B is assumed turbulent for all fuel configurations and the laminar categories are eliminated [30]. The strong instability and high uncertainty in turbulent convection with buoyancy and IHG also make it very challenging to model in CFD. Therefore, section B is conservatively approximated as turbulent forced convection using the Dittus–Boelter correlation:

$$Nu_B = 0.023\, Re_B^{0.8}\, Pr^{0.4} \tag{3.32}$$

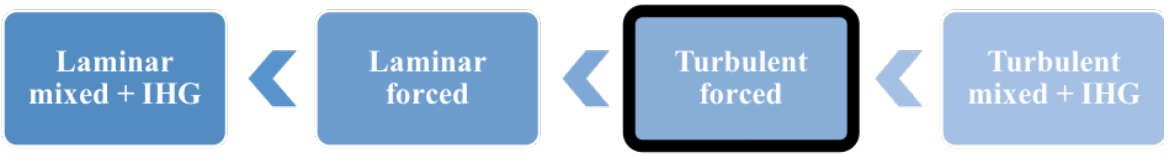

Fig. 3.4 Heat transfer correlation selection for fuel section B, descending annulus

3.2.2 Developing a new heat transfer correlation

A mixed convection heat transfer correlation is developed that can be applied to calculate bulk temperatures in section A, the ascending core region of the concentric fuel concept. As opposed to performing a detailed CFD calculation for each configuration of interest, a correlation facilitates efficient exploration of BBMSR design options, such as fuel tube geometry and power rating, that are bound by the maximum fuel temperature. Heat transfer is investigated by simulating the laminar ascending mixed convection flow of incompressible fluid in an open-ended vertical tube, with prescribed inlet velocity and temperature, and uniform IHG and wall cooling flux. Varying boundary conditions and geometries of interest for the fuel concept are modelled. In addition, the maximum-to-bulk temperature relationship is investigated so that the peak fuel temperatures within section A can be estimated, and the fuel can be designed within safe temperature limits.

The system modelled in CFD represents only section A of the fuel. Since the goal is to characterise radial temperature profile trends rather than absolute temperatures, it is not necessary to model the entire concentric fuel configuration, nor the axially varying heating conditions present in a nuclear fuel element. Simplifying the model also improves confidence in the simulated results because there are fewer components and phenomena to verify.

The thermophysical properties of the Moltex SSR fuel salt NaCl–UCl_3–$PuCl_3$ (60–20–20%) are used for the CFD modelling since the lower viscosity of the preferred BBMSR fuel, 100% UCl_3, results in highly unstable simulations. In addition to numerical instability, the low viscosity of UCl_3 is likely to result in turbulent flow for most relevant fuel configurations, so the laminar results from the simulations of NaCl–UCl_3–$PuCl_3$ provide a conservative approximation of heat transfer in the UCl_3 fuel.

3.3 CFD Study

The open-source CFD package OpenFOAM is used to simulate heat transfer in the system representing section A. The pre-built solver *buoyantBoussinesqPimpleFoam*, "a transient solver for buoyant, turbulent flow of incompressible fluids," is modified for this analysis [72]. A heat source term is added in the energy equation, allowing the IHG parameter to be specified as a boundary condition. The OpenFOAM temperature boundary condition *externalWallHeatFluxTemperature* is used to simulate the isoflux walls.

The custom solver iteratively solves the Boussinesq-approximated Navier–Stokes equations for the given geometry, fluid properties, and boundary conditions to obtain the velocity

and temperature fields. The transition to turbulence is not straightforward to predict for mixed convection with IHG, so all flows are assumed laminar in this study and turbulence modelling is switched off. Although steady-state heat transfer behaviour is the objective of the present work, the transient solver was found to be significantly more stable than the steady-state version for buoyant, incompressible flow. The transient solver employs the pressure-velocity coupling algorithm PIMPLE, which merges the steady-state SIMPLE and the transient, pressure-implicit PISO methods. The result is a transient, semi-implicit algorithm that iterates over the pressure, momentum, and energy equations until the absolute residual tolerance falls below 10^{-7}, arriving at a steady-state solution for each time step. The code automatically adjusts the time step to maintain a Courant number less than 0.9, and 100 seconds is found to be sufficient for convergence to a steady-state heat transfer solution in all simulated configurations.

3.3.1 Boundary conditions

Figure 3.5 illustrates the defined boundary conditions: temperature T_{in} and velocity v_{in} are uniform across the inlet, cooling flux q''_w is uniform along the walls, and volumetric heat generation rate q''' is uniform everywhere within the fluid. Nineteen cases are simulated in OpenFOAM, using a range of geometries and boundary conditions of practical interest for section A of the BBMSR concentric fuel concept. To represent overall fuel D ranging from 10–25 mm, the ascending fuel system is simulated with $d = 7.1$–17.7 mm (corresponding to d_A with $\varepsilon = 0.5$). The tube length L is fixed at 4 meters for all cases. q''' ranges from 75–300 W/cm^3; q''_w from 2.0–10.5 W/cm^2; v_{in} from 0.13–0.15 m/s; and T_{in} from 828–1000 K. The wall temperature T_w increases with distance from the bottom of the cylinder z, while the radial profiles of T and v become fully developed within 4 meters for all simulated configurations. The no-slip condition $v_w = 0$ is satisfied everywhere.

3.3.2 Physical properties

All simulations are performed using the estimated properties of the Moltex fuel mixture, NaCl–UCl_3–$PuCl_3$ (60–20–20 mole%), which has an estimated Prandtl number of 4.0. The properties are reported in Table 3.1, with density and viscosity evaluated at a film temperature of 1273 K.

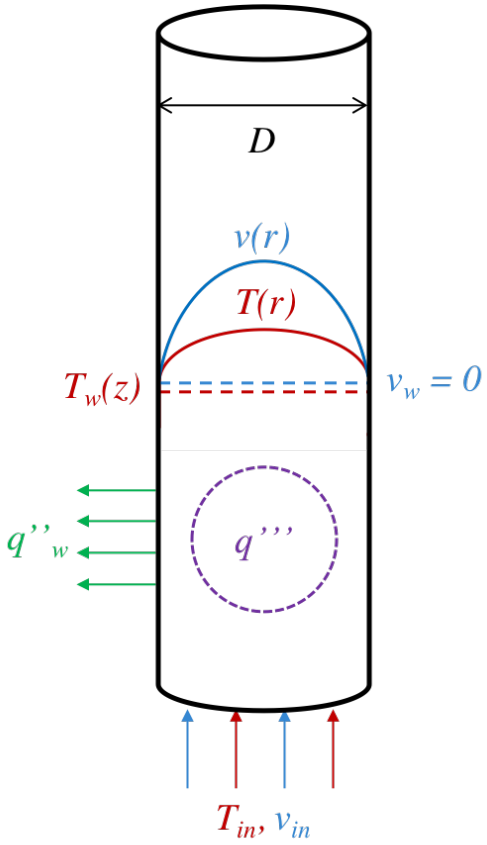

Fig. 3.5 System modelled in CFD

Table 3.1 Thermophysical properties of NaCl–UCl_3–$PuCl_3$, from refs. [8, 38]

Property	Equation	Value at 1273 K
Density, ρ (kg/m^3)	$4.1690 - (9.014 \times 10^{-4} T\,[\mathrm{K}])$	3042
Kinematic viscosity, $\nu = (\mathrm{m}^2/\mathrm{s})$	$\exp(-1.2675 + 1704/T\,[\mathrm{K}])10^{-6}$	1.18×10^{-6}
Specific heat capacity, c_P (J/(kg K))		550
Thermal conductivity, κ (W/(m K))		0.5

3.3.3 Mesh sensitivity & model verification

The mesh utility supplied with OpenFOAM, *blockMesh*, is used to generate a structured O-grid cylindrical mesh, as shown in Figure 3.6. The O-grid cylinder face is extruded axially to produce structured axial mesh layers.

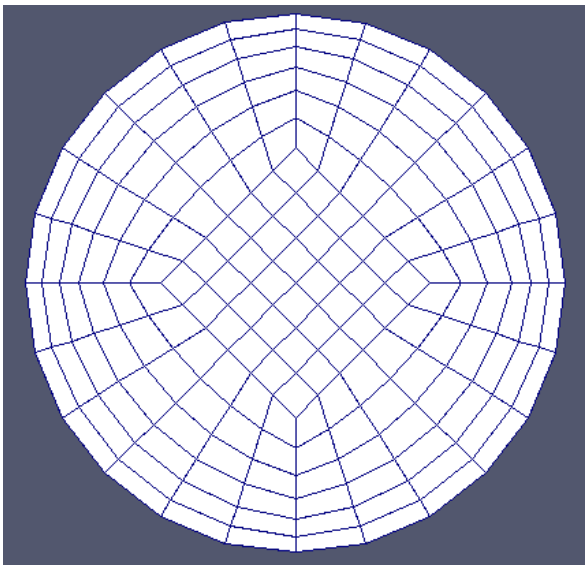

Fig. 3.6 O-grid mesh configuration with $M_d = 18$

A verification and mesh sensitivity study has been performed using the reference scenario of forced convection with uniform wall heat flux and zero IHG. The mesh was gradually refined, increasing the number of cells by varying both the diametric cell number M_d and axial layer number M_z, until a configuration was identified that produces heat transfer and momentum solutions within $\pm 5\%$ of the analytical Nusselt number and friction factor values for fully developed Poiseuille flow, $Nu = 4.36$ and $f = 64/Re$, respectively. Figure 3.7 presents the mesh refinement results, with the "Optimal" mesh configuration (indicated in red) satisfying the 5% accuracy requirement for both Nu and f with the smallest number of cells. The pair of clustered points are the results of mesh configurations with different combinations of M_d and M_z but a similar number of total cells. The optimal configuration for a tube of $d = 10$ mm and $L = 4$ m was achieved with $M_d = 18$ and $M_z = 600$. For the simulations of varying d, M_d is adjusted to maintain the optimal resolution, while $M_z = 600$ is fixed since L is held constant for all simulations in the study.

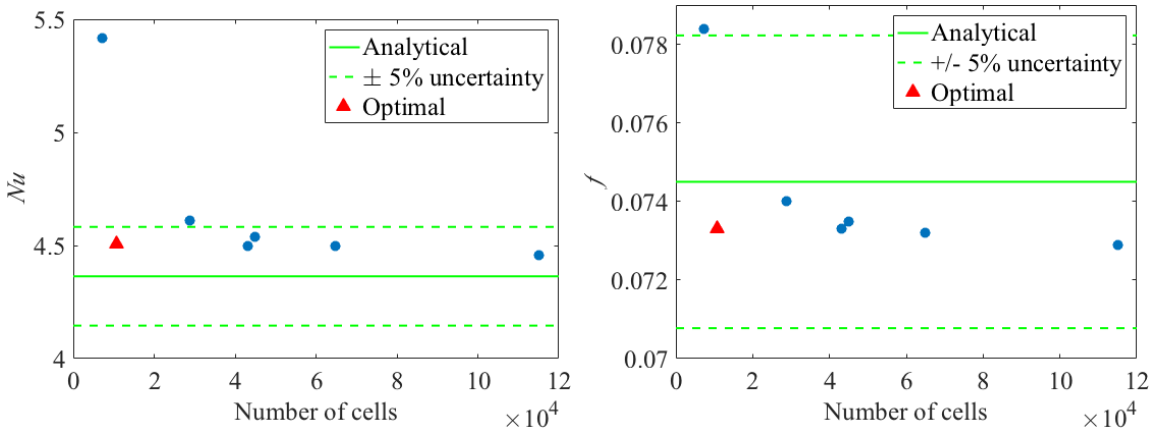

(a) Mesh convergence of Nu

(b) Mesh convergence of f

Fig. 3.7 Mesh refinement results

3.3.4 CFD results

To characterise the heat transfer performance of each simulated case, the Nusselt number (Nu), Reynolds number (Re), and Grashof number (Gr) are calculated at each axial mesh position as:

$$Nu = \frac{dq''_w}{(T_m - T_w)\kappa} \tag{3.33}$$

$$Re = \frac{\rho v_m d}{\mu} \tag{3.34}$$

$$Gr = \frac{g\beta\rho(T_m - T_w)d^3}{\mu} \tag{3.35}$$

where T_m is the axial bulk temperature and T_w is the axial wall temperature. In this thesis, a negative value of Nu denotes simply that T_w is greater than T_m. The local values Nu, Re, and Gr are averaged over the top 50 mesh layers (or 33 cm) of the tube to obtain a set of converged parameters for each simulated case. In mixed convection flows, Nu typically depends on Re and Gr. Figure 3.8 shows Nu plotted against each parameter, but neither appears to correlate well with heat transfer behaviour.

The apparent lack of order with respect to Re and Gr motivates the development of new non-dimensional parameter specifically for mixed convection flow with IHG and cooling wall flux. Energy gained by the system due to IHG is removed by (1) radial conduction at the wall by a cooling heat flux, and (2) axial mixed convection. This heat transfer balance can be expressed in terms of boundary conditions as the ratio of heat generated internally to

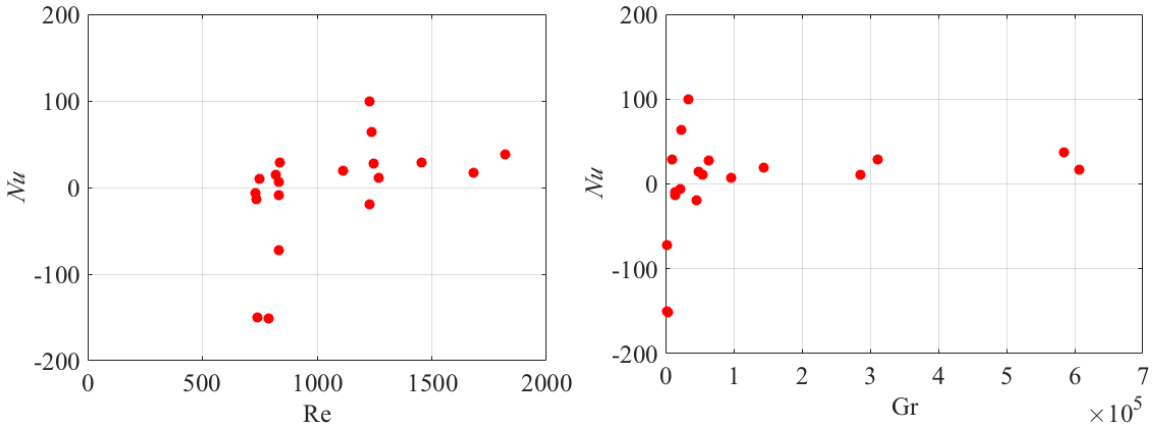

(a) Nusselt versus Reynolds number (b) Nusselt versus Grashof number

Fig. 3.8 Nusselt number versus traditional non-dimensional parameters

heat removed at the wall,

$$\frac{q'''\pi d^2 L/4}{-q''_w \pi d L} \tag{3.36}$$

which is simplified and assigned to the new non-dimensional IHG-flux number, Ω:

$$\Omega = -\frac{q'''d}{4q''_w} \tag{3.37}$$

At moderately small values of Ω, axial convection and radial conduction contribute similarly to removal of the internally generated heat, while for larger Ω, most of the heat is removed by axial convection of the fluid. At the limit when $\Omega \to \infty$, it can be shown analytically that the radial temperature profile is an inverted parabola with the maximum occurring at the wall, even though a cooling flux may be present [14]. Since the heat transfer balance also influences the buoyancy contribution to flow and heat transfer, Ω reflects the tightly coupled mixed convection phenomena present in the IHG system. Figure 3.9 showing *Nu* versus Ω reveals patterns within three distinct heat transfer regimes, using Ω as the transition criterion:

(I) $\Omega \leq 4$

(II) $4 < \Omega < 6$

(III) $\Omega \geq 6$

The trends and detailed heat transfer behaviour are investigated by exploring a single case from each of these regimes. All three representative cases share $d = 10.6$ mm, $v_{in} = 0.15$ m/s,

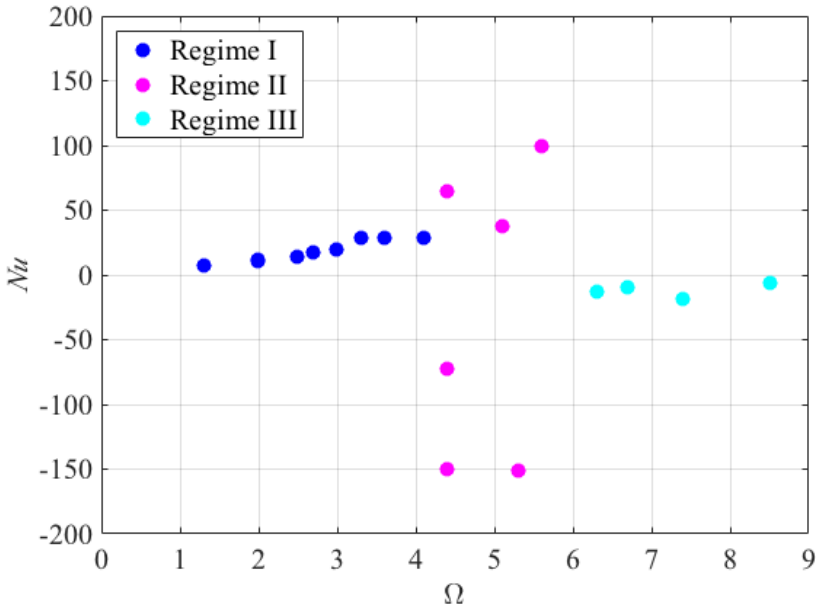

Fig. 3.9 Nusselt number versus IHG-flux number

and $T_{in} = 1000$ K, while Table 3.2 summarises the varying inputs and results. Figure 3.10 presents the radial temperature and velocity profiles of the representative cases. The temperature profiles are normalised by T_{in}, since the aim is to characterise radial temperature trends rather than calculate absolute temperatures. The axial temperature and velocity trends can also be observed by comparing the radial profiles at $0.2L$, $0.4L$, $0.6L$, $0.8L$, and L.

Table 3.2 Summary of selected cases for regime comparison

	Inputs			Results	
	q''' (kW/m^3)	q''_w (kW/m^2)	Ω	$T_m - T_w$ (K)	Nu
Regime I case	7.50E+04	100	2.0	185.7	11.4
Regime II case	2.10E+05	100	5.6	21.3	99.3
Regime III case	7.50E+04	27	7.4	−30.0	−19.1

Regime I is characterised by stable mixed convection behaviour, and Figure 3.9 shows that Nu is well correlated to Ω. Figure 3.10a shows a relatively uniform temperature across the core, resulting from the combination of uniform IHG and convection by the centre-peaked velocity profile (Figure 3.10b), with a temperature gradient near the wall due to the cooling flux. Since IHG, mixed convection, and wall cooling all have perceptible effects on the temperature profile, Regime I is named the "mixed heat transfer" (MHT) regime. A correlation is developed by fitting an exponential curve through the nine simulated results in

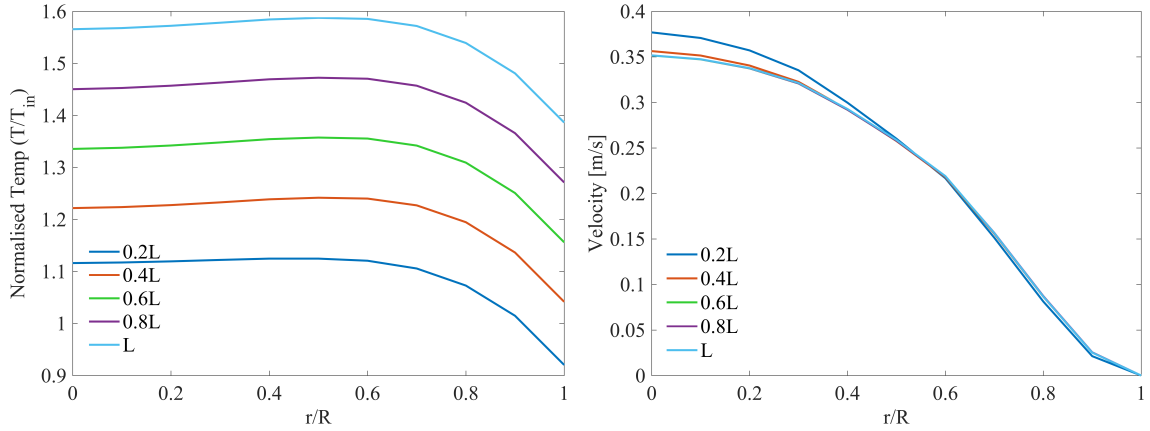

(a) Regime I, radial temperature profile

(b) Regime I, radial velocity profile

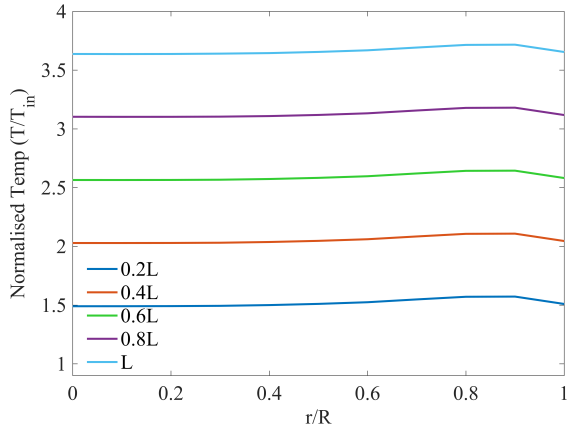

(c) Regime II, radial temperature profile

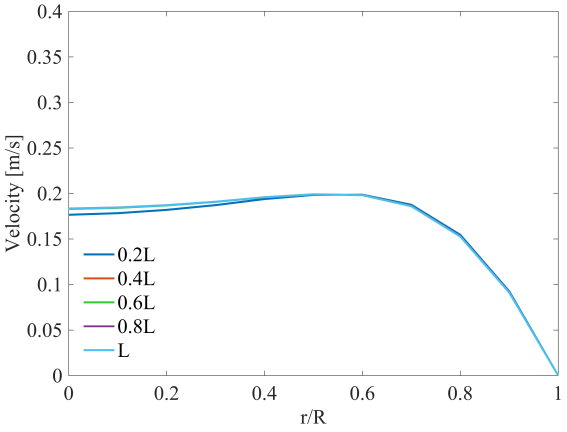

(d) Regime II, radial velocity profile

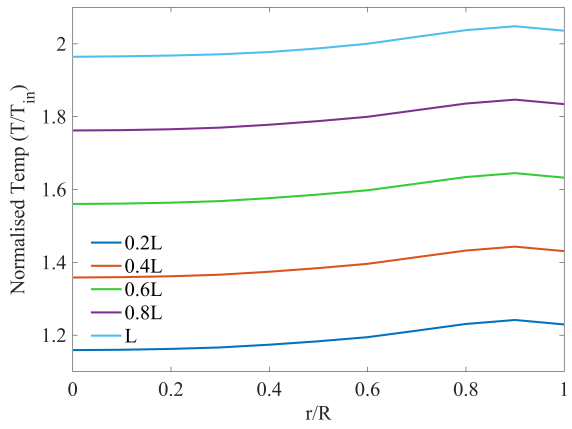

(e) Regime III, radial temperature profile

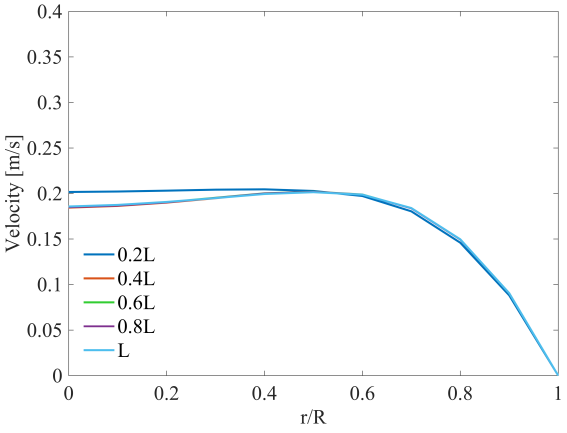

(f) Regime III, radial velocity profile

Fig. 3.10 Comparison of heat transfer regimes

the MHT regime, with $Nu = 4.36$ set as the intercept since the system is assumed to converge to forced-laminar-uniform flux heat transfer behaviour when $\Omega = 0$:

$$Nu = 4.36 \exp(0.4954 \times \Omega) \tag{3.38}$$

The fit has an *R*-squared value of 0.93. Applying the MHT correlation at its upper limit of $\Omega = 4$ yields $Nu = 31.63$, which is 625% larger than the forced-laminar-uniform flux value of $Nu = 4.36$.

In traditional pipe flow heat transfer theory, the flow is thermally fully developed when the radial temperature distribution converges. This convergence is determined by calculating the ratio,

$$\tau = \frac{T_w - T_m}{T_w - T_{Max}} \tag{3.39}$$

In wall-heated forced convection flow with $Nu = 4.36$, $\tau = 1.636$. The Regime I results have an average value of $\tau = 1.2$, reflecting the flatter radial profile resulting from IHG and mixed convection. The MHT correlation can be used to estimate bulk temperatures, while τ can be used to estimate maximum radial temperatures in section A.

For Regime II where $4 < \Omega < 6$, Figure 3.10c shows that the temperature profile is almost uniform, due to a smaller wall cooling flux than in the MHT regime. While the displayed profiles are smooth and appear stable, the presence of an inflection point in the velocity profile (Figure 3.10d) is destabilising and can produce turbulence even at low values of *Re* [58]. Thus, there is high uncertainty in the simulated heat transfer behaviour of Regime II, which can be observed in the considerable scatter of *Nu* in Figure 3.9. Regime II is therefore called the "unstable" regime.

In Regime III where $\Omega > 6$, Nu is always negative because $T_w > T_m$, as shown in Figure 3.10e. Since radial conduction is very small relative to IHG in Regime III, heat transfer is dominated by convection. The fluid velocity at the wall is zero, so heat accumulates at the wall and the temperature profile is inverted. It may be possible to correlate *Nu* to another non-dimensional parameter in Regime III, named the "insulated" regime. However, this is left for future work since $\Omega > 6$ is beyond the scope of interest for the molten salt nuclear fuel design. It is noted that the velocity profile in Figure 3.10f also contains an inflection point, so instability remains likely and there may be significant uncertainty in the simulated results. The observations of unstable flow and negative *Nu* at higher values of Ω agree with previously reported analytical estimates based on an arbitrary fixed velocity field [14]. The present work expands on these estimates by obtaining the velocity field and defining simple

transition criteria between the regimes of MHT, unstable, and insulated mixed convection with IHG.

3.4 Conclusions

The MHT correlation can be integrated into a finite-difference model to calculate the axial temperature profile in section A. Configurations with $\Omega > 4$ should be eliminated from the fuel design study since they are likely to have unstable convection behaviour, so Equation 3.38 and $\tau = 1.2$, for calculating bulk and peak temperatures respectively, are adequate to model section A numerically.

The proposed regimes and MHT correlation are valid for ascending, laminar flow of an incompressible fluid in a wall-cooled vertical tube. Since the study was performed to enable analysis and design of the BBMSR fuel concept, the correlation has been developed specifically based on the properties of a molten salt fuel.

However, the methodology and use of the non-dimensional parameter Ω can be extended to analysis of other systems with IHG and mixed convection, including descending flows. Influence of fluid properties, such as viscosity and coefficient of thermal expansion, was not examined in this work. Future analysis could include other incompressible fluids to evaluate whether the MHT correlation can be improved by incorporating property influences. Further investigation is needed for a more detailed understanding of heat transfer behaviour in the unstable and insulated regimes. For example, turbulence modelling may improve the simulation accuracy, possibly revealing trends that enable the development of new correlations for these regimes. Finally, experimental study of the system with IHG and mixed convection is necessary to validate the findings in this work.

Chapter 4

Thermal–Hydraulic Fuel Modelling

Mixed convection in the BBMSR concentric fuel design can be analysed using a one-dimensional finite-difference model (FDM) to calculate velocity and temperature distributions in the fuel tube sections. The newly developed MHT correlation from Chapter 3 can be used to calculate heat transfer in section A, the inner section, while the Dittus–Boelter correlation can be used for section B. This chapter describes how the FDM is developed; the model is then used to investigate the thermal–hydraulic behaviour of the concentric BBMSR fuel and determine the maximum achievable power density for various configurations. The FDM is incorporated into a fuel design package that enables efficient exploration of the design space within defined operational constraints.

4.1 Finite-Difference Model for Concentric Fuel

Figure 4.1 illustrates the physical layout of the concentric pipe with overall diameter D and length L, and the nodalization scheme used in the FDM. With N axial nodes in each section, there are $2N$ nodes in total for which the energy and momentum balance are solved. r_A is the radius of section A, and r_B is the annular thickness of section B, as defined in Section 3.2. q''_A is the heat flux across the inner wall from section A to section B, and q''_B is the heat flux across the outer cladding from section B.

4.1.1 Energy balance

Figure 4.2 illustrates the balance of energy from IHG, axial convection, and radial conduction for general nodes in sections A and B. The IHG term in each node is the product of node volume and local heat generation rate q'''_z. It is assumed that q'''_z varies axially with a chopped

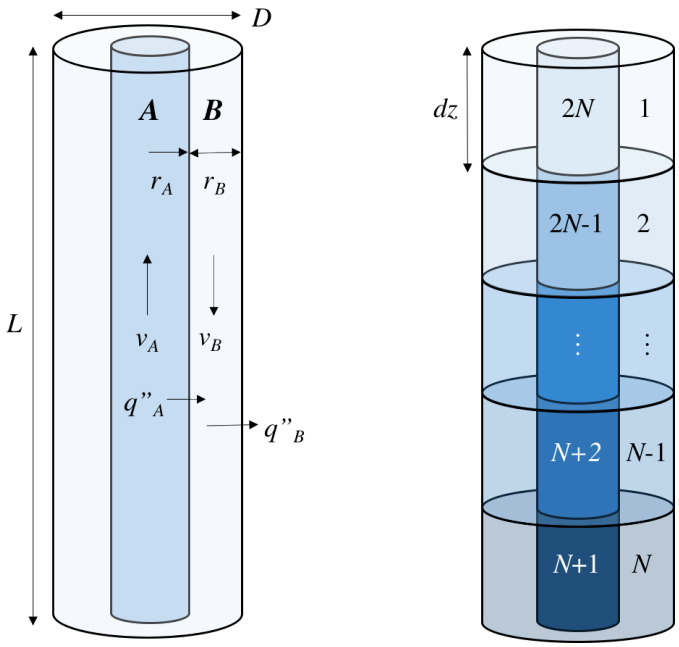

Fig. 4.1 Concentric fuel pipe layout and axial nodalization

cosine power shape, representing the simplified neutron flux shape in a reactor with some axial neutron leakage, neglecting the effects of delayed neutron drift and axial reflectors at this stage:

$$q'''_z(z) = q''' \cdot cos\left(\frac{\pi z}{L_e}\right) \tag{4.1}$$

where q''' is the peak heat generation rate and L_e is the neutronic extrapolation length where the flux is zero. The node volumes V_A and V_B are found by multiplying the cross-sectional area of each section (related by ε) by the node height $dz = L/N$.

The axial flow of thermal energy into and out of all nodes is given by $\dot{m}c_P T$. The FDM calculation is initialised with a random guess for $\dot{m}$, which is iteratively updated as the model converges on the velocity and temperature distribution solution.

The radial conduction quantities q_A and q_B are calculated in terms of the differences between T_A, T_B, and the outer fuel temperature (i.e., inner cladding surface temperature) T_{ci} as:

$$q_A = \frac{T_A - T_B}{R_A} \tag{4.2}$$

$$q_B = \frac{T_B - T_{ci}}{R_B} \tag{4.3}$$

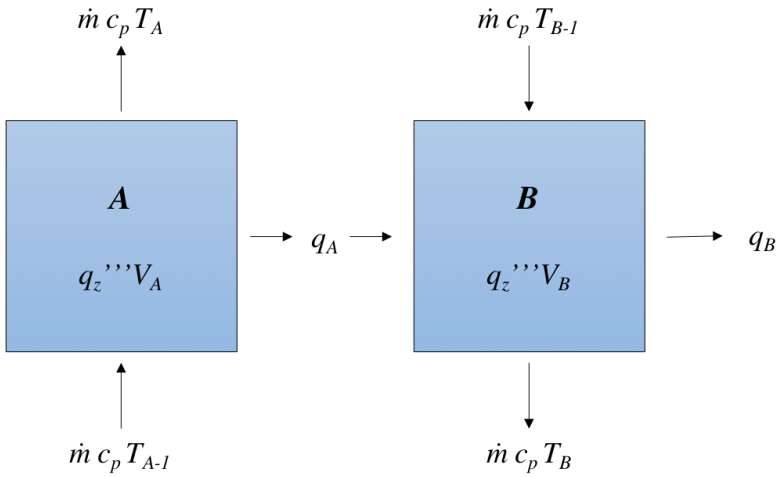

Fig. 4.2 Energy balance on inner (A) and outer (B) fuel nodes

where R_A and R_B are the respective thermal resistances across each wall:

$$R_A = \frac{1}{h_A r_A 2\pi dz} + \frac{\ln(r_w/r_A)}{\kappa_w 2\pi dz} + \frac{1}{h_B r_w 2\pi dz} \tag{4.4}$$

$$R_B = \frac{1}{h_B D\pi dz} \tag{4.5}$$

The outer radius of the inner wall is $r_w = r_A + t_w$. The heat transfer coefficient in each section is $h_X = Nu_X \kappa_f / d_X$, where $X = A, B$. Nu_A is calculated using the MHT correlation (Equation 3.38) and Nu_B is calculated using the Dittus–Boelter correlation (Equation 3.32), as explained in Section 3.2.1. Ω is calculated using Equation 3.37, where $q''_w = q_A/(2\pi r_A dz)$ and $d = d_A$.

Table 4.1 organises the energy balance terms for each type of A and B node: top, bottom, and middle. All energy terms in each row sum to zero. Radial conduction between sections A and B is neglected for the top and bottom nodes, since thermal energy is transferred primarily by the flow of fuel between concentric sections. The node index i ranges from 1 to $2N$, with 1–N in section B and $(N+1)$–$2N$ in section A, as shown in Figure 4.1. For each node i, the index of its corresponding adjacent node in the other section is $2N+1-i$, as shown in Figure 4.1.

All energy terms are balanced for each node by grouping similar terms together into a matrix of coefficients of T_i and a matrix of known values (i.e., IHG and T_{ci} terms). The bulk T_i values can then be solved by simple matrix division.

Finally, the maximum radial temperatures in section A are estimated using Equation 3.39 with $\tau = 1.2$, where $T_m = T_A$ and T_w is the temperature of the inner wall at a given axial location. Assuming heat flux is constant across the inner wall from section A to section B, the axial profile of T_w can be calculated:

$$\frac{T_A - T_w}{1/(h_A 2\pi r_A dz)} = \frac{T_A - T_B}{R_A} \tag{4.6}$$

4.1.2 Momentum balance

The momentum balance is solved to calculate the bulk velocity in the concentric fuel sections. Since the fuel tube is a closed system with no externally imposed pressure gradient, the changes in gravitational and frictional pressure, p_g and p_f respectively, over both sections must sum to zero according to Bernoulli's principle:

$$\Delta p_g + \Delta p_f = 0 \tag{4.7}$$

U-bend losses between sections are neglected. Using the axial temperature distribution from the energy balance calculation, the fuel density in each node i is calculated using the density equation for UCl_3 from Table 2.8, $\rho_i = 6.3747 \times 10^3 - 1.5222 \times T_i[K]$. The net gravitational pressure drop over all nodes is found by summing terms in each section:

$$\Delta p_g = \left(\sum_{i=1}^{N} \rho_i \cdot g \cdot dz \right)_A - \left(\sum_{i=1}^{N} \rho_i \cdot g \cdot dz \right)_B \tag{4.8}$$

Table 4.1 Energy balance for all node types

Node index i	Convection		Conduction		IHG
	In	Out	In	Out	
1	$\dot{m}c_P T_{2N}$	$-\dot{m}c_P T_1$	0	$-\frac{T_1 - T_{ci,1}}{R_B}$	$q'''_i V_B$
$2:(N-1)$	$\dot{m}c_P T_{i-1}$	$-\dot{m}c_P T_i$	$\frac{T_{2N+1-i} - T_i}{R_A}$	$-\frac{T_i - T_{ci,i}}{R_B}$	$q'''_i V_B$
N	$\dot{m}c_P T_{N-1}$	$-\dot{m}c_P T_N$	0	$-\frac{T_N - T_{ci,N}}{R_B}$	$q'''_i V_B$
$N+1$	$\dot{m}c_P T_N$	$-\dot{m}c_P T_{N+1}$	0	0	$q'''_{2N+1-i} V_A$
$(N+2):(2N-1)$	$\dot{m}c_P T_{i-1}$	$-\dot{m}c_P T_i$	0	$-\frac{T_i - T_{2N+1-i}}{R_B}$	$q'''_{2N+1-i} V_A$
$2N$	$\dot{m}c_P T_{2N-1}$	$-\dot{m}c_P T_{2N}$	0	0	$q'''_{2N+1-i} V_A$

Then the velocities in A and B can be solved by combining Equation 3.31 with the equation for net frictional pressure drop:

$$\Delta p_f = \left(f_A \cdot \frac{L}{d_A} \cdot \frac{\rho_m v_A^2}{2} + f_B \cdot \frac{L}{d_B} \cdot \frac{\rho_m v_B^2}{2} \right) \tag{4.9}$$

where ρ_m is the density at the mean temperature of the entire fuel tube.

The friction factors f_X are obtained using correlations for turbulent, transition, and laminar flow. In turbulent flow with $Re_X > 30,000$, the McAdams relation for a smooth tube is applied in either section:

$$f_X = 0.184\, Re_X^{-0.2} \tag{4.10}$$

The Blasius relation gives the friction factor in transition flow, for $2300 < Re_X \leq 30,000$ in either section:

$$f_X = 0.316\, Re_X^{-0.25} \tag{4.11}$$

For laminar flow with $Re_X \leq 2300$, molecular shear effects are significant over the flow cross-section, and Figure 4.3 shows that the friction factor of an annular flow depends on the ratio of inner radius r_i to outer radius r_o [77]. Section A is a simple circular tube with $r_i/r_o = 0$, so from Figure 4.3 where $f' = 4f$, the correlation is:

$$f_A = 64/Re_A \tag{4.12}$$

For section B, $r_i/r_o = r_A/r_B$, which varies by fuel configuration. To simplify the FDM, section B is approximated as an infinite parallel flat-plate channel with $r_i/r_o = 1$, corresponding to the upper limit friction factor correlation:

$$f_B = 96/Re_B \tag{4.13}$$

This is a conservative approximation, since a larger friction factor will reduce heat transfer from the fuel.

4.1.3 Iterative numerical schemes

Since Nu_B is a function of v_B and the velocities depend on the temperature distribution, the coupled temperature–velocity solution must be obtained iteratively. Using a Gauss–Seidel iteration algorithm, an arbitrary guess for $\dot{m}$ initialises the energy balance routine to find the temperature distribution, from which the momentum balance is calculated to update $\dot{m}$, and

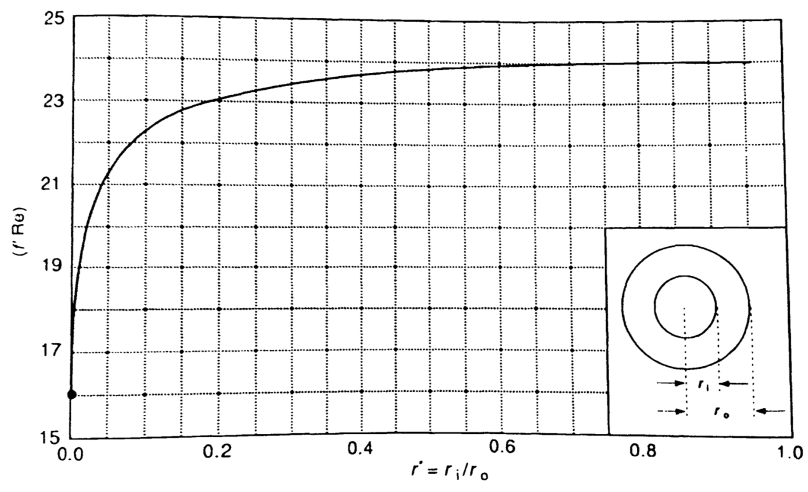

Fig. 4.3 Product of laminar friction factor ($f' = 4f$) and Reynolds number for fully developed flow in an annular channel, from [77]

so on until the value of $\dot{m}$ converges. However, the Gauss–Seidel algorithm was found to be unstable for some input configurations, resulting in numerical oscillation between two solution modes.

Using the interval halving algorithm instead, the energy balance is initialised with two arbitrary $\dot{m}$ guesses that conservatively bound the solution value of $\dot{m}$. The interval between $\dot{m}$ guesses is iteratively halved to eventually converge on the value of $\dot{m}$ that satisfies both the energy balance and Bernoulli equations. Interval halving is simple to implement in the FDM, converges quickly, and remains stable for all input configurations, so it is adopted as the preferred iterative algorithm.

An additional outer iteration loop is needed to converge on the value of Nu_A as a function of Ω, which depends on the temperature distribution and q_A. This loop is found to be stable using the Gauss–Seidel algorithm. It is initialised with the guess $\Omega = 2.0$ (the median of the valid range), and the value of Ω is updated each time that a converged temperature–velocity solution is obtained in the inner iteration loop.

4.1.4 FDM results and parametric study

This section examines how axial temperature distributions in the concentric fuel are affected by varying diameter, length, and power density in the FDM. A base case is defined with $D =$ 10 mm, $L = 2$ m, and $q''' = 100$ W/cm^3. In case variant 1, L is increased to 4 m; variant 2 increases D to 20 mm; and variant 3 increases q''' to 200 W/cm^3. The case inputs are listed in Table 4.2.

Table 4.2 Concentric fuel parameter study inputs

	Base case	Variant 1	Variant 2	Variant 3
D (mm)	10	10	20	10
L (m)	2	4	2	2
q''' (W/cm^3)	100	100	100	200

For all four cases, $\varepsilon = 0.5$, and power density is distributed as a cosine power shape according to Equation 4.1. The extrapolation length is assumed to be $L_e = 1.5L$ for all configurations, which corresponds to a relatively high axial leakage rate and low axial power peaking; the actual value of L_e/L will depend on the realistic axial neutron flux shape in the BBMSR. The cladding inner surface temperature is defined as a simple linear gradient from 550°C at the bottom of the coolant channel to 700°C at the top. The properties of UCl_3 evaluated at 1273 K are taken from Table 2.8. The inner wall is modelled as 0.3-mm thick SiC, with thermal conductivity $\kappa = 30$ W/mK from Table 2.9. Table 4.3 summarises the FDM results of the four cases by comparing the peak fuel temperature, fuel temperature range, average Ω value, and velocity in section A. The axial temperature profile results for each of the four cases are also plotted in Figure 4.4. The plots display the cladding inner surface temperature input, T_{ci}; section B bulk temperature, T_B; inner wall temperature, T_w; and in section A both the bulk temperature T_A and maximum radial temperature T_{Max}.

Table 4.3 Concentric fuel parameter study results

	Base case	Variant 1 (L = 4 m)	Variant 2 (D = 20 mm)	Variant 3 (q''' = 200 W/cm^3)
Peak T (°C)	1136	1120	1155	1364
T range (°C)	478	487	387	666
Ω	2.5	1.9	6.6	2.7
v_A (m/s)	0.12	0.08	0.17	0.14

Figure 4.4a shows that in the base case, the temperature in section A increases almost linearly as the fuel moves upwards, approaching a peak around $0.8L$ and remaining nearly flat to the top. The hot fuel moves into section B at the top and then loses heat through the cladding surface as it descends. The bulk temperature at the bottom is approximately 100°C hotter than the cladding surface temperature.

For variant 1 with $L = 4$ m, Figure 4.4b shows a more skewed temperature distribution, with a larger difference between sections A and B in the top half compared to the base case. The value of Ω is smaller than the base case, but the peak temperature and range are

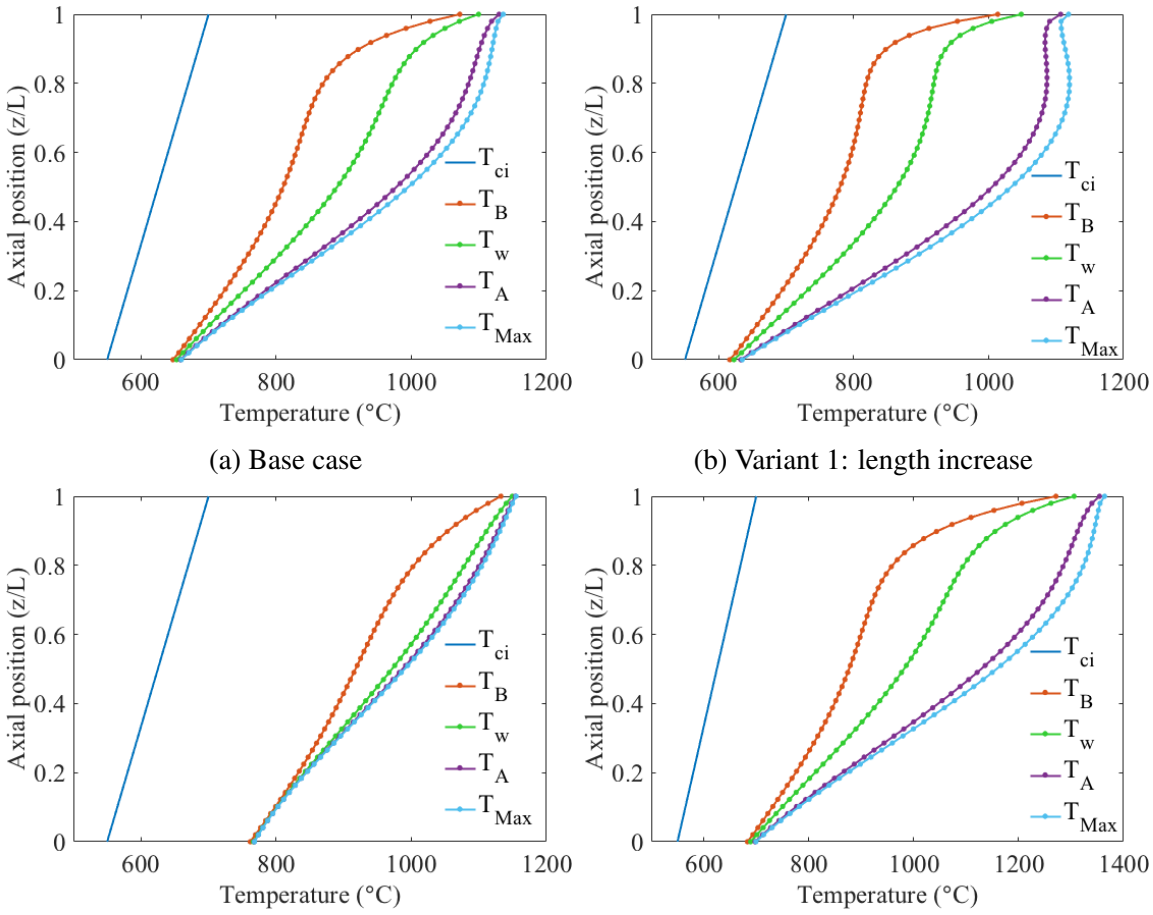

(a) Base case

(b) Variant 1: length increase

(c) Variant 2: diameter increase

(d) Variant 3: power increase

Fig. 4.4 FDM results

similar, indicating that the overall fuel heat transfer performance is not affected significantly by height, given the same surface temperature range. In a realistic fuel system, the coolant will accumulate more heat as it moves up through a taller channel so T_{ci} will have a larger range. In addition, a larger coolant pressure drop in a taller channel may reduce the allowable coolant mass flow rate.

For variant 2 with $D = 20$ mm, $\Omega = 6.1$ and therefore $Nu_A = 90$ according to the MHT correlation (Equation 3.38). This high Nu_A makes T_A only slightly hotter than T_w in Figure 4.4c. The minimum temperature is significantly hotter than for the previous cases, but the peak temperature is similar. However, since the MHT correlation is valid only for $\Omega \leq 4$, this value of Nu_A is non-physical and the configuration would be eliminated from the design search.

Variant 3 with $q''' = 200$ W/cm^3, shown in Figure 4.4d, has a similar Ω value and temperature profile shape to the base case. The temperatures are effectively scaled up due to the higher power, with the peak temperature 300°C hotter, and the range larger by 225°C.

Overall, the FDM parameter study shows that the value of Ω corresponds to the shape of the temperature profile. The difference between T_A and T_B shrinks as Nu_A improves with increasing Ω.

4.1.5 Concentric fuel flow area parametric study

The parameter ε, or the ratio of the section A cross-sectional area to the total fuel area, can be tuned for optimal heat transfer in each fuel configuration. Figure 4.5 illustrates $\varepsilon = 0.5$ and $\varepsilon = 0.8$ for $D = 10$ mm. The effect of ε on heat transfer performance is demonstrated using the FDM to evaluate the peak fuel temperature as ε is varied from 0.3 to 0.8. Figure 4.6 shows the results for fuel configurations with D ranging from 10 mm to 50 mm, and fixed parameters $L = 2$ m and $q''' = 100$ W/cm^3. The peak fuel temperature increases sharply for larger values of ε with smaller tube diameters, since the frictional pressure drop increases as section B narrows, and convective heat transfer is impaired.

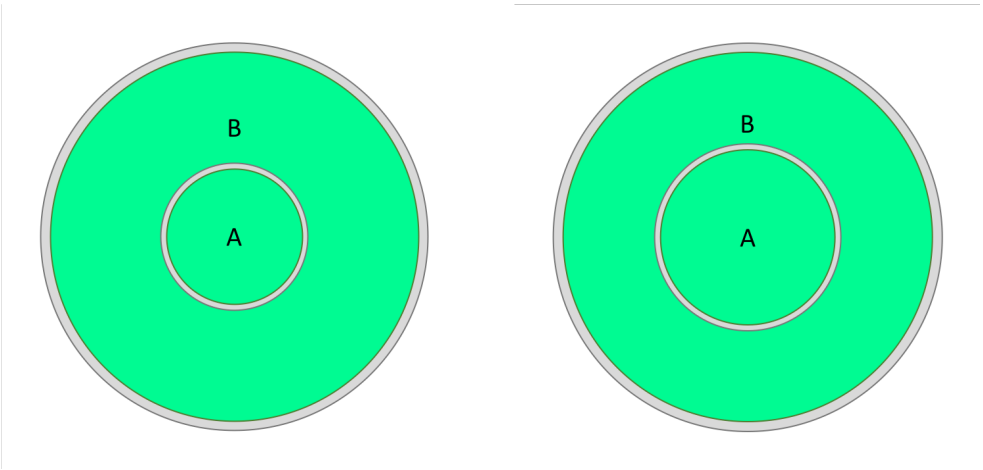

(a) $\varepsilon = 0.5$ (b) $\varepsilon = 0.8$

Fig. 4.5 Illustration of varying ε value for $D = 10$ mm

While the fuel length and heat generation rate also slightly influence the optimal value of ε, the trends are similar to those shown in Figure 4.6. Since all configurations appear to have an optimum roughly near $\varepsilon = 0.5$, this value is used for all comparison studies presented in this chapter. In later design stages, ε can be optimised specifically for preferred configurations.

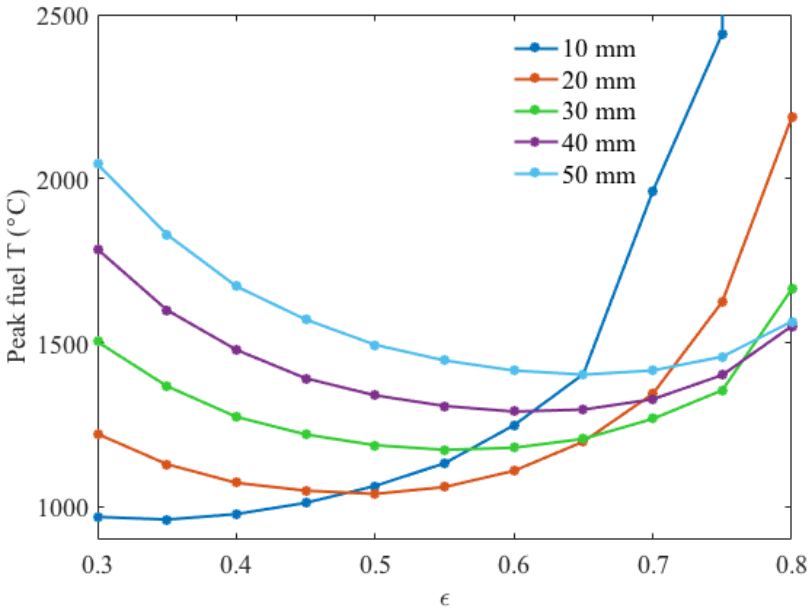

Fig. 4.6 Optimal ε by fuel diameter

4.2 Thermal–Hydraulic Design Search Program

This section describes a program developed to enable efficient thermal–hydraulic design of the fuel by modelling the performance impacts of various fuel geometries and searching for limiting operating parameters. The resulting modelling package is used during the neutronic analysis described in Chapter 5 to identify viable fuel designs.

4.2.1 Inputs and constraints

The fuel D, L, and pitch-to-diameter ratio (P/D) are entered as inputs to the design program. The thermal–hydraulic design of the BBMSR fuel is primarily constrained by pressure drop across the core and the temperature limits of fuel, cladding, and coolant materials. The wide range of potential design configurations and unusual behaviour of the convecting fuel leads to some non-obvious thermal–hydraulic interactions and trade-offs. Since the fuel and coolant salts have high melting temperatures, the system temperatures are limited at the lower as well as the upper end. The relatively high viscosities and low thermal conductivities of the molten salts introduce additional design challenges.

To manage this complexity, the design program has been developed with only three fixed thermal–hydraulic constraints: maximum fuel temperature, core pressure drop, and core outlet temperature. These constraints are explicitly defined at the highest level of the design program, and the program satisfies them by iterating to find the limiting values of power

density and coolant mass flow rate, given the fuel geometry inputs. The allowable maximum fuel temperature is a safety constraint, while the maximum pressure drop is an economic and operational constraint.

The remaining performance parameters are treated as flexible constraints, since their target values may need to be adjusted based on the results of initial design iterations, or because of uncertainties in material properties. The flexible constraints are used as criteria applied to a set of results, to evaluate and narrow the design parameters for the next design iteration. This approach allows more flexibility and enhances transparency of the design process, as opposed to explicitly limiting the values of many parameters. Modelled results for some configurations that fail to meet certain requirements or targets may still provide valuable information that guides the next design iteration.

4.2.2 Algorithm description

First, the coolant mass flow rate is calculated based on the geometry inputs and maximum pressure drop constraint using equations given in Appendix B. Then, the program iteratively solves for the value of q''' that results in the maximum allowable fuel temperature and defined core outlet temperature, using the interval halving algorithm described in Section 4.1.3 to ensure stable convergence. The fuel heat generation rate q''' is converted to channel power density, which takes into account the volume of all the fuel, cladding, and coolant in the channel.

The key performance parameters and flexible constraints are calculated as outputs. As the power is updated in each iteration, the axial coolant and cladding temperature profiles are calculated and used as inputs to the FDM, which returns the values of Ω, T_w, T_B, and T_{Max}. Appendix B contains the equations used to calculate the coolant velocity, and coolant and cladding temperature profiles for a given value of q'''.

4.3 Fuel Design Trade-Off Analysis

A trade-off analysis is performed using the thermal–hydraulic design search program to identify trends in the performance of the BBMSR concentric fuel design. The modelled geometry inputs are defined according to Table 4.4. P/D is given for a hexagonal lattice, since a hexagonal arrangement allows high fuel volume fractions without prohibitively high pressure drop. The modelled axial power shape is a chopped cosine with $L_e = 1.5L$.

Table 4.4 Geometry inputs for trade-off study

D (mm)	10, 12.5, 15
L (m)	2, 3, 4
P/D	1.10, 1.12, 1.14, 1.16, 1.18, 1.20
ε	0.5

The fuel boiling temperature is assumed to be the most limiting temperature in the system. Since the cladding temperature limit is reactor specific, further studies are required before a limit can be established for the BBMSR concept. The chloride coolant salt has a high boiling temperature that is unlikely to be approached in any practical fuel design configurations. Therefore, the maximum allowable fuel temperature is constrained to 1550°C, which allows a 200°C margin from the estimated boiling temperature of 100% UCl_3 fuel, 1750°C [48].

The core pressure drop is physically limited by the system pumping power requirement and available pump technology. In this thesis the core pressure drop is fixed at 1 MPa, a roughly typical value for fast reactors [27]. The value is calculated simply as the frictional pressure drop in the coolant channel, using the correlation for a cylindrical geometry. Gravitational pressure drop within the coolant channel can be neglected if density changes are small, since it is balanced by the negative term from the return flow of coolant outside of the core. In a configuration with coolant pumped upward through the channel, neglecting gravitational pressure drop is a conservative assumption since buoyancy aids the heated flow of coolant. Other sources of pressure loss due to expansion, contraction, and fuel spacers, which typically contribute around 15% of the total pressure drop in a fast reactor, are also excluded in this stage of analysis [22].

The coolant outlet temperature is fixed at 750°C, so the program solves for the inlet temperature in each fuel configuration. Most molten salt reactor designs have an outlet temperature between 700–850°C [7]. Outlet temperatures as high as 1000°C are targeted for future designs, based on the estimated capabilities of advanced materials. Properties of the ternary chloride coolant $MgCl_2$–NaCl–KCl (50–30–20%) are found in Table 2.7.

The high fuel operating temperatures of the BBMSR demand a suitably resistant material for the outer cladding and inner wall. Candidate materials discussed in Section 2.3.3 are evaluated neutronically in Chapter 5, but SiC is modelled in the present trade-off study because it is assumed to have the most favourable combination of properties for the BBMSR. An outer cladding thickness of 0.5 mm is assumed, similar to other fast reactors, while the inner wall thickness is modelled as 0.3 mm, since it is not load bearing. While SiC in particular has not yet been demonstrated with such thin cladding structures, the vented fuel

design minimises stress on the structure because there is virtually no pressure difference across the cladding or inner wall, which should allow the use of thinner materials [18].

4.3.1 Key performance parameters

The key thermal–hydraulic performance parameters are core power density, core temperature rise, and pumping power. These parameters are related to the economics of building and operating the reactor. High core power density leads to a lower capital cost on a per MWe basis because the core size can be reduced for the same amount of power generated.

A small core temperature rise, ΔT_{core}, is desirable because it reduces the required size and cost of heat exchangers; decreases axial thermal stresses on the cladding; and allows the core outlet temperature T_{out} to be maximised within material temperature limits. High T_{out} increases plant thermal efficiency, especially if the reactor is coupled to an advanced high-temperature power conversion system such as the Brayton or S-CO_2 cycle. In addition, a reactor with high T_{out} may be able to supply industrial process heat, increasing potential plant revenues. In the BBMSR, an axially homogeneous fuel composition also keeps axial power peaking low, which helps the goal of small ΔT_{core} and high T_{out}.

Small coolant pumping power is desirable to reduce the required pump size and cost, which directly impacts the reactor capital cost. In addition, the plant thermal efficiency is reduced by the power consumed for pumping, so this performance parameter should be minimised. Pumping power depends on the coolant mass flow rate and pressure drop, which are in turn related to the power density and ΔT_{core}. For example, a larger power density requires more pumping power to maintain safe temperatures and small ΔT_{core}, so these competing effects must be balanced.

Figure 4.7a shows that the allowable channel power density decreases almost linearly as P/D increases for a given fuel diameter and length. Although a looser pitch allows a higher fuel power rating q''', compactness is sacrificed as a smaller proportion of the channel is producing power, so the overall power density decreases. The allowable power density decreases significantly as the fuel diameter increases, similar to solid fuel. As the length increases, the allowable power density decreases because the fixed core pressure drop is spread over a taller channel, so the coolant mass flow rate is reduced. The optimal configuration for maximising channel power density would have a small diameter and height, and a tight lattice. A typical LWR has a core power density of 100 W/cm^3, whereas an SFR can yield more than twice this figure. BBMSR fuel configurations with channel power density greater than 100 W/cm^3 are considered economically competitive for the purposes of

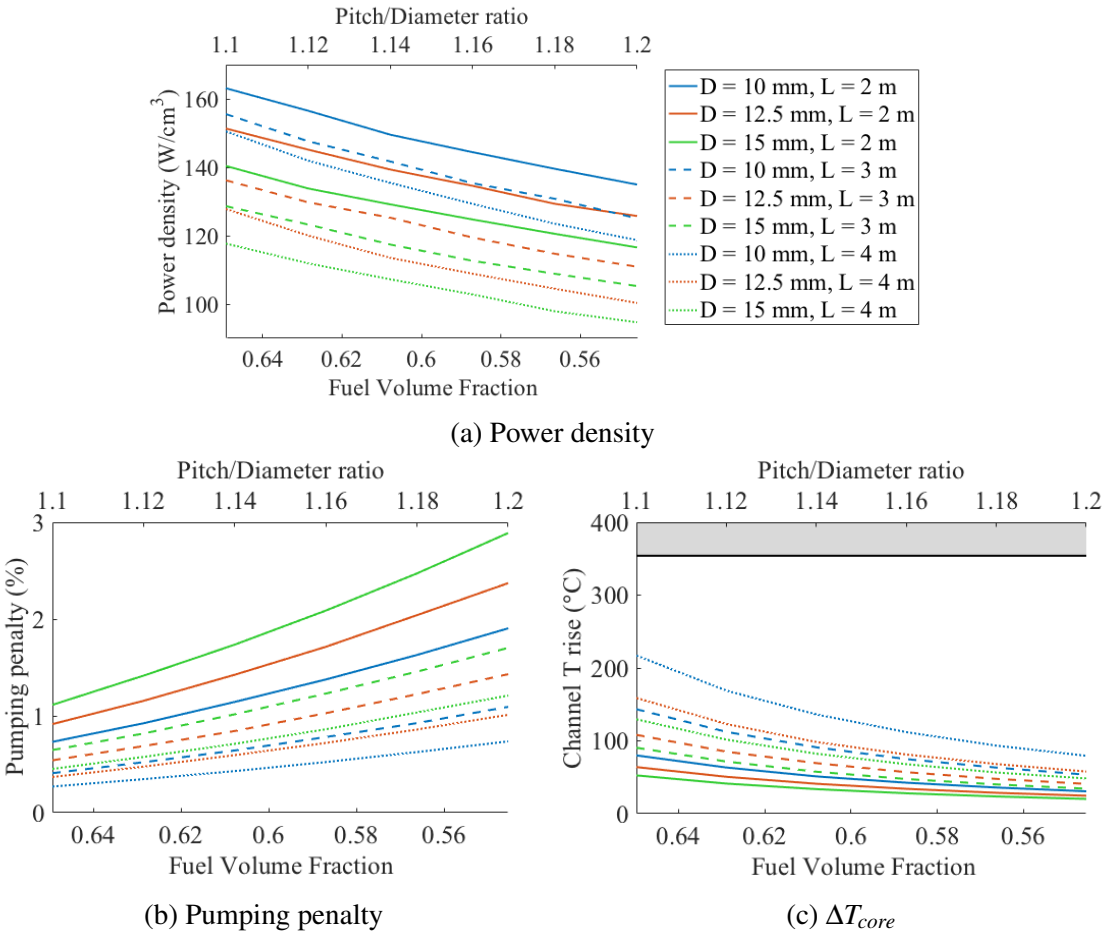

(a) Power density

(b) Pumping penalty

(c) ΔT_{core}

Fig. 4.7 Key performance parameters

this thesis, and Figure 4.7a shows that all of the modelled configurations achieve this target for $P/D < 1.16$.

Figure 4.7b shows the system's pumping penalty, or pumping power as a fraction of power generated in the channel. Since the pressure drop is fixed in this study, the coolant mass flow rate increases with increasing pitch and decreasing length, which in turn increases the required pumping power. Typical reactor pumping power is between 1% and 10% of total reactor thermal power, and the pumping penalties seen in Figure 4.7b fall within this range [25]. The pump is modelled as 100% efficient in this work, whereas a realistic pump efficiency is 80–90% [77].

Figure 4.7c shows that ΔT_{core} decreases as the channel pitch grows. With fixed pressure drop, the increasing coolant mass flow rate in a looser lattice reduces the temperature rise. For the BBMSR using the ternary chloride coolant, ΔT_{core} is constrained to no more than 354°C, equal to the margin between the fixed T_{out} (750°C) and freezing point of the coolant

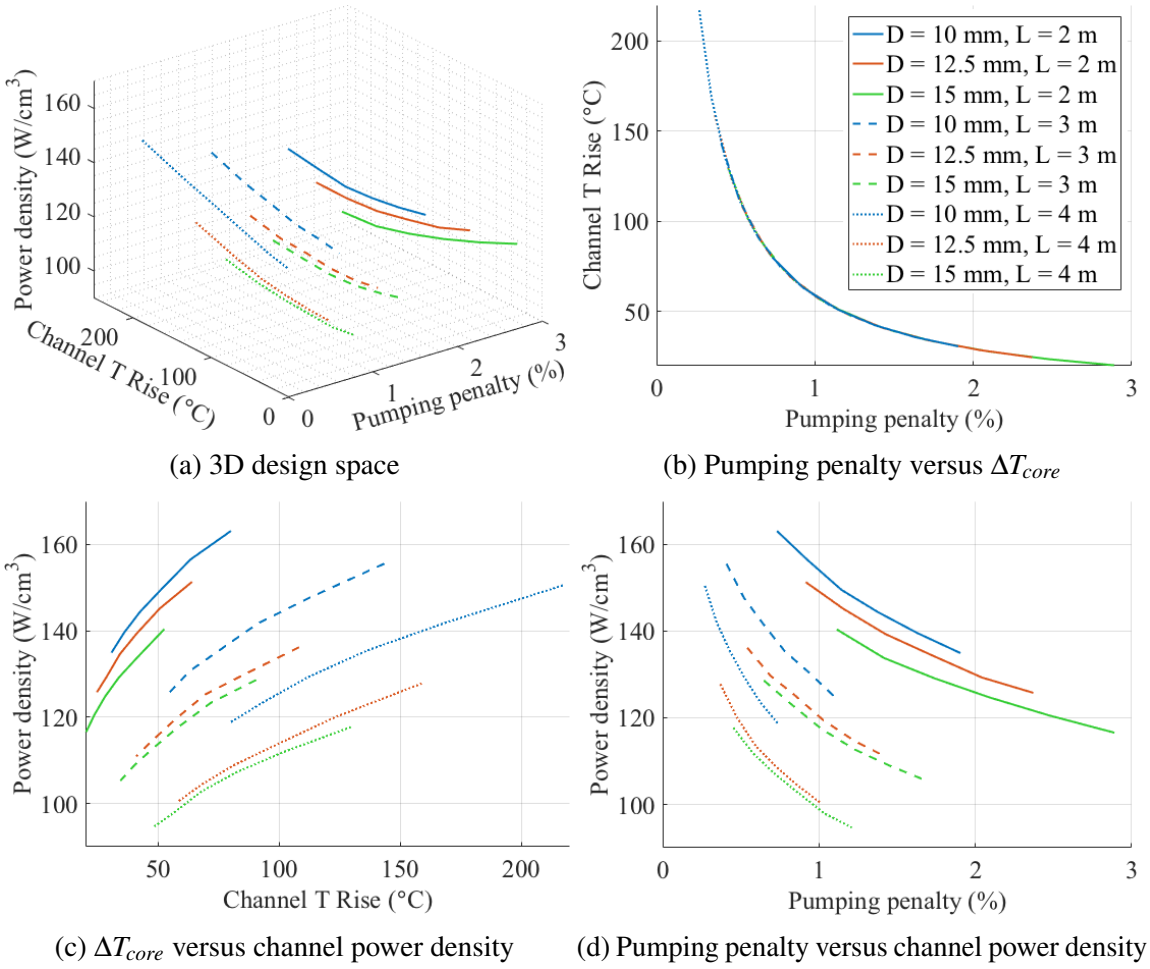

(a) 3D design space

(b) Pumping penalty versus ΔT_{core}

(c) ΔT_{core} versus channel power density

(d) Pumping penalty versus channel power density

Fig. 4.8 Trade-offs of key performance parameters

salt (396°C). Most of the modelled BBMSR configurations have ΔT_{core} below 200°C, even at $P/D = 1.1$.

The three-dimensional plot in Figure 4.8a depicts the interaction of channel power density, pumping penalty, and ΔT_{core}, and its two-dimensional projections are shown to examine each pair of parameters. From Figure 4.8b, ΔT_{core} decreases exponentially as pumping penalty increases regardless of the fuel geometry, so the optimal balance between these parameters lies somewhere in the middle of the range. From Figure 4.8c, ΔT_{core} increases with power density for the given constraints, especially as the fuel lengthens. Figure 4.8d shows that power density decreases as the pumping penalty grows, corresponding to increasing P/D. In summary, a high power density and low pumping power can be achieved simultaneously, but at the cost of a high ΔT_{core}.

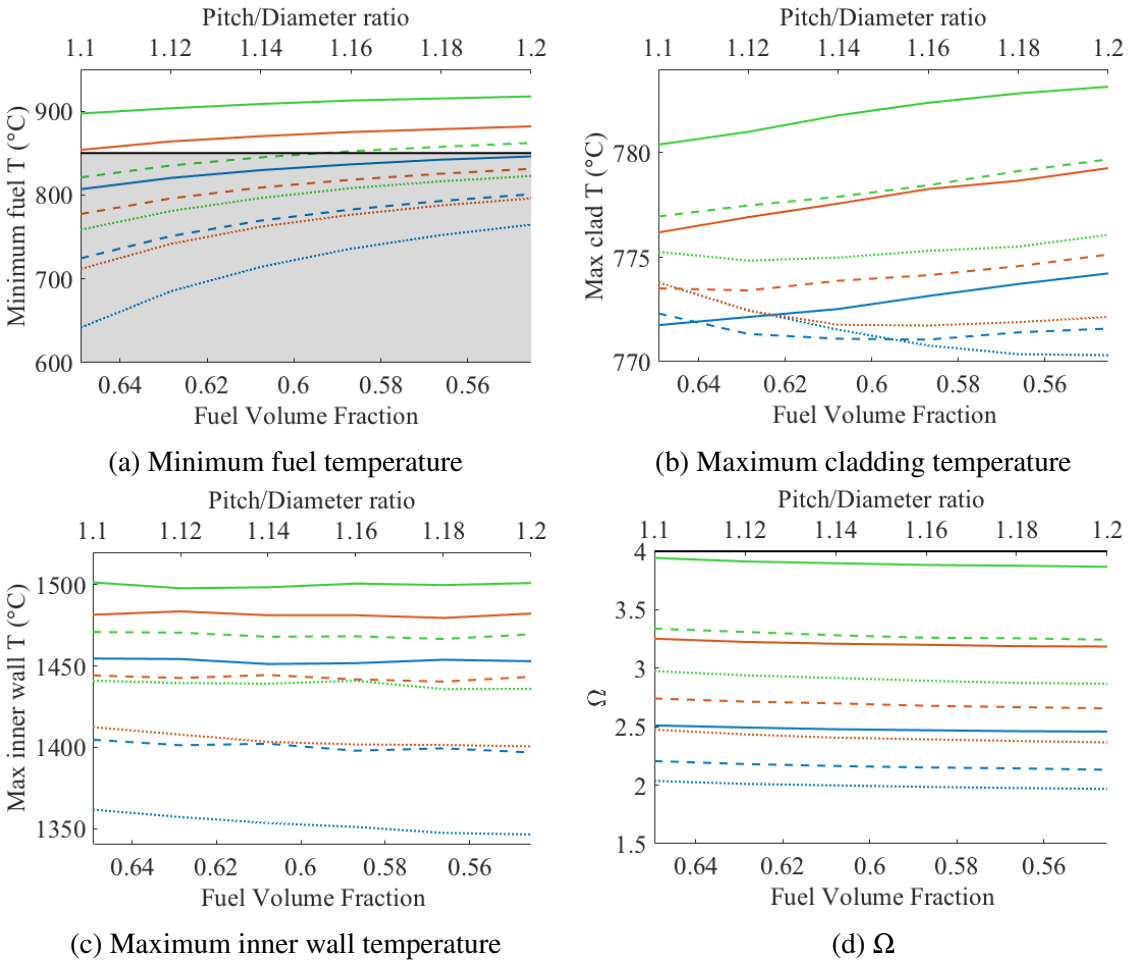

(a) Minimum fuel temperature

(b) Maximum cladding temperature

(c) Maximum inner wall temperature

(d) Ω

Fig. 4.9 Flexible constraints (refer to legend of Figure 4.8)

4.3.2 Flexible constraints

The minimum fuel temperature, maximum cladding temperature, maximum inner wall temperature, and Ω are evaluated as flexible constraints for the modelled fuel configurations.

The minimum fuel temperature is constrained by the melting point of UCl_3, 850°C. In practice, the fuel will likely remain liquid slightly below the melting point due to turbulent mixing in the flow, so the minimum fuel temperature has not been imposed as a fixed constraint but is rather used as a design guide. However, Figure 4.9a shows that most of the modelled configurations have a minimum fuel temperature well within the freezing range indicated by the shaded region. The minimum fuel temperature is smallest for the fuels with small D and long L, since these also have a large ΔT_{core}, as seen in Figure 4.7c. This analysis demonstrates that avoiding fuel freezing is an additional reason to minimise ΔT_{core}.

The maximum outer cladding and inner wall temperatures are shown in Figures 4.9b and 4.9c, respectively. Further material studies would be needed to quantify temperature limits for both outer cladding and inner wall. For the preferred material SiC, the melting temperature is 2545°C and creep resistance in LWRs is demonstrated up to 1600°C [68]. The structural integrity of the outer cladding is important for safe operation of the BBMSR, and the maximum temperatures in Figure 4.9b are well within the LWR creep temperature limit for SiC. However, the maximum inner wall temperatures shown in Figure 4.9c are significantly higher, but since the inner wall is not structurally important, these high temperatures may be tolerable.

The value of Ω is calculated for all fuel configurations to check that they fall within the valid range of the MHT correlation ($\Omega \leq 4.0$), and Figure 4.9d shows that they do for the modelled fuel geometries. The Ω limit is used to inform the design process, rather than explicitly constraining Ω in the design search program.

Similar phenomena explain the trends seen for the cladding and inner wall temperatures and Ω. As observed in Section 4.1.4, Ω increases with larger D and shorter L, indicating improved heat transfer and smaller temperature differences radially across the fuel. As a result, the cladding and inner wall temperatures tend to be higher for these configurations, since the design program identifies the power density that results in the maximum allowable fuel temperature. In addition, the maximum cladding temperature tends to increase with P/D, which may be attributed to more efficient cooling resulting in less radial temperature peaking of the fuel. Ω and the maximum inner wall temperature are not significantly affected by P/D.

4.3.3 Coolant direction study

Analysis of the key performance parameters in the trade-off study indicates that the advantages of high power density and low pumping penalty correspond to high ΔT_{core}, which is undesirable for efficiency and cost considerations. A high ΔT_{core} also negatively affects the flexible constraints, since large temperature differences within the fuel element push the limits of both fuel boiling and freezing. A potential strategy to reduce ΔT_{core} without significantly impairing the other performance parameters is to reverse the direction of coolant flow, so that the coolant flows down the channel and increases in temperature from top to bottom. The hottest fuel always tends to occur near the top due to the internal natural convection effect, so the hotter fuel and colder coolant are axially aligned. The goal is to

effectively "flatten" the average axial temperatures, so that the average moves closer to the maximum allowable temperature, and the power density can be increased.

The FDM is used to quantify the effect of coolant flow direction for a single representative fuel configuration, with temperature distributions shown in Figure 4.10 and key results summarised in Table 4.5. The base case defined in Section 4.1.4 is revisited as the upward flow scenario, and the downward flow scenario is identical except that the cladding inner surface temperature profile T_{ci} is reversed.

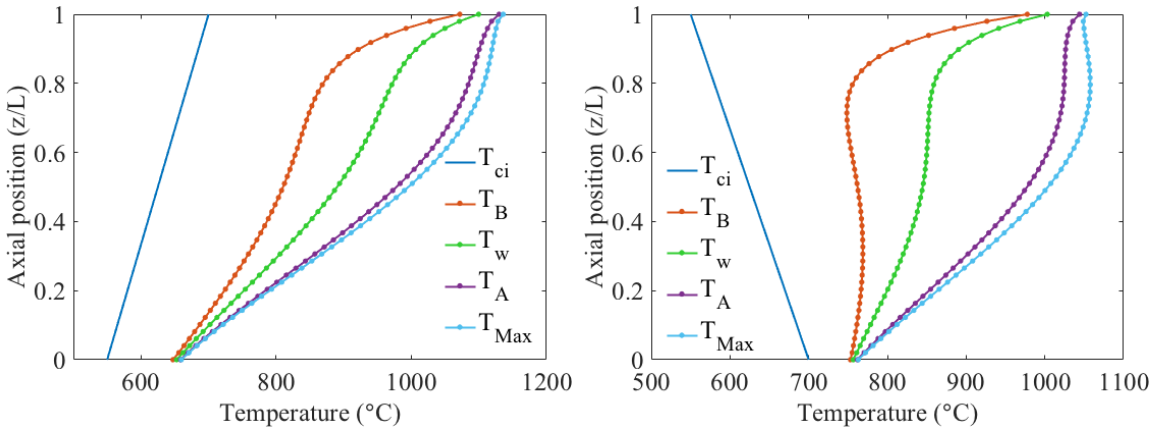

(a) Upward flowing coolant (b) Downward flowing coolant

Fig. 4.10 Comparison of coolant flow direction scenarios

Table 4.5 Coolant flow direction comparison results

	Upward flow	Downward flow
Peak T (°C)	1136	1058
T range (°C)	478	296
Ω	2.5	2.0
v_A (m/s)	0.12	0.12

The upward flow case is analogous to a counterflow heat exchanger, in which a fairly steady temperature differential is maintained between the hot and cold fluids (i.e., fuel and coolant) over the length of the channel, as seen in Figure 4.10a. The downward flow case is analogous to a parallel flow heat exchanger, in which the temperature differential is large at the inlet (top) and decreases over the length of the channel, as seen in Figure 4.10b. In principle, parallel flow has lower heat cycle efficiency compared to counterflow, due to greater heat transfer irreversibility arising from the large temperature differential at the inlet. However, this is manifested as a lower peak fuel temperature and smaller fuel temperature

range for a given BBMSR fuel configuration, which is advantageous to avoid freezing and boiling of the fuel salt.

The thermal–hydraulic design search program is used to perform a parametric study for downward coolant flow, maintaining a fixed $T_{out} = 750°C$ at the bottom of the channel. The other inputs and constraints from the original trade-off study are kept the same, and the program searches for the coolant inlet temperature at the top of the channel in each configuration. Since buoyancy opposes the direction of coolant flow in this configuration, the buoyancy contribution to gravitational pressure drop is quantified as

$$\Delta p_b = (\rho_{in} - \rho_{out}) g L \tag{4.14}$$

For the ternary chloride coolant with ρ given in Table 2.7, assuming $\Delta T_{core} = 100°C$ and $L = 4$ m, the buoyant pressure is calculated to be $\Delta p_b = 3.049$ kPa, which is only 0.3% of the total core pressure drop 1 MPa. The gravitational pressure drop is therefore neglected for simplicity in modelling all downward flowing coolant configurations, and only the frictional pressure drop is considered.

The resulting key performance parameters from the downward flow parametric study are shown in Figure 4.11. Figure 4.11a shows that downward flowing coolant yields power densities approximately 10% higher than the upward flow results shown in Figure 4.7a, without noticeably increasing either pumping penalty (Figure 4.11b) or ΔT_{core} (Figure 4.11c). Aligning the colder fuel with warmer coolant towards the bottom of the channel increases the minimum fuel temperatures, so that a larger subset of configurations are viable in terms of avoiding fuel freezing, as seen in Figure 4.11d. Figure 4.11e shows that Ω is also slightly reduced compared to Figure 4.9d, which will be advantageous when considering larger fuel D. Downward flowing coolant is thus adopted as a key feature of the BBMSR concept.

4.4 Discussion and Conclusions

The analysis presented in this chapter indicates that the BBMSR concentric fuel design with 100% UCl_3 fuel, ternary chloride coolant, and SiC cladding can satisfy thermal–hydraulic requirements and achieve competitive power densities. Next, neutronic analysis is performed to assess whether fuel configurations that can achieve economically competitive power density also exhibit the neutron economy required for B&B operation.

While radiative heat transfer in the coolant salt may be significant, it is unlikely to play a role within the fuel because actinide-carrying salts are not optically transparent. Wavelength-

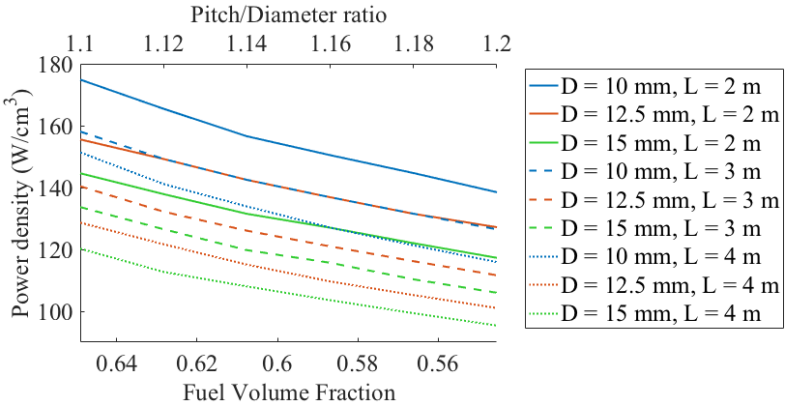

(a) Power density

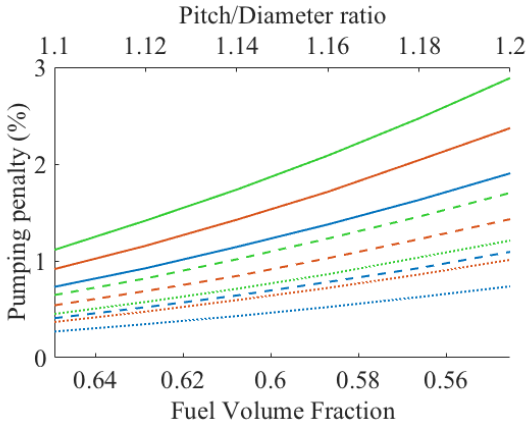

(b) Pumping penalty

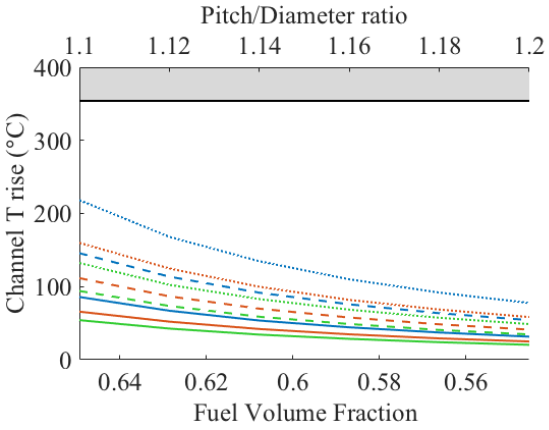

(c) ΔT_{core}

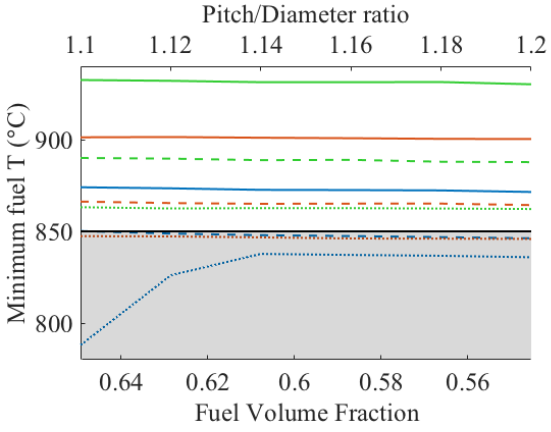

(d) Minimum fuel temperature

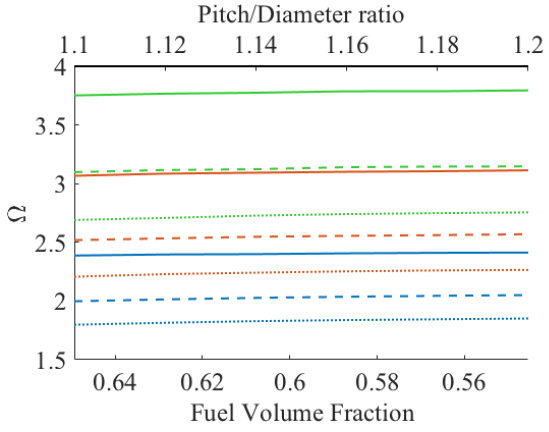

(e) Ω

Fig. 4.11 Downward flowing coolant results

dependent absorption data are needed to estimate radiative heat transfer in the molten salts, but there has been little experimental so far work to characterise this phenomenon. However, neglecting radiation in the present approach leads to a more conservative estimate of heat transfer performance.

The fuel design is restricted such that section A remains in flow Regime I, since the MHT correlation is only valid in this regime. However, BBMSR fuel designs that fall into the two other regimes could be considered in future work if modelling methods are developed to estimate their heat transfer coefficients, which would expand the design space.

Although the high melting point of the fuel and resulting high operating temperatures of the system are challenging to balance with the other system constraints, the BBMSR's high outlet temperature could enable high plant thermal efficiency. In solid-fuelled reactors, even if advanced cladding materials are developed, metallic fuel has a relatively low melting temperature and low temperature of Pu–Fe eutectic formation [25]. Use of molten salt fuel may confer a considerable advantage in this area.

Chapter 5

Neutronic & Thermal–Hydraulic Fuel Design

A primary objective of the BBMSR is to improve fuel utilisation from current LWR levels, without use of reprocessing or high enrichment. In addition, the BBMSR should be capable of a core power density of at least 100 W/cm^3 to be economically competitive with LWRs. Neutronic scoping and thermal–hydraulic analysis are performed to search for BBMSR fuel configurations that are attractive in terms of both fuel utilisation and power density.

Since numerous trade-offs exist between thermal–hydraulic and neutronic performance, the thermal–hydraulic design search program is used to determine the practical operational limits of the configurations considered. The neutronic feasibility assessment (Section 2.2) shows that neutronic performance improves with fuel tube diameter, but Section 4.3 demonstrates that most thermal–hydraulic objectives are more easily satisfied at smaller tube diameters. In addition, Section 4.3 indicates that higher power density and smaller core temperature rise can be achieved with shorter fuel length, but the effect of core height on axial neutron leakage must also be considered.

In this chapter, fuel configurations are investigated for three different fuel cycle scenarios: natural uranium, 5% enriched, and 20% enriched feed fuel. Fuel with 5% enrichment represents the current, LWR-based fuel cycle infrastructure capability, while 20% is the maximum safeguards limit for LEU, as defined by the International Atomic Energy Agency [35]. Many advanced reactor designs require more than 5% enrichment, so it is reasonable to expect that the future fuel cycle will allow uranium enrichment in the range 5–20%.

5.1 Methodology

5.1.1 3D pin cell model

For neutronic evaluation of each BBMSR fuel configuration, a three-dimensional, heterogeneous pin cell is modelled with fuel, inner wall, cladding, and coolant salt. The fuel tube diameter D and length L_{fuel} are varied to identify neutronically viable geometries. Axial leakage is simulated using vacuum axial boundaries beyond the neutron reflectors, discussed below. Radial leakage and other neutron losses such as absorption in non-fuel materials are assumed to be zero, so the pin cell is modelled with reflective radial boundaries. All fission products are assumed to remain in the fuel throughout burnup for the present analysis, which is a conservative approximation since release of fission gases in the vented fuel is likely to improve neutronic performance.

Section 4.3 shows that power density increases as the hexagonal P/D decreases, and the pumping penalty remains acceptably low even for very tight lattices. Practically, the minimum value of P/D is limited by the wire wrap used to space the fuel for coolant flow. In typical hexagonal lattice fast reactor assemblies, the wire wrap diameter, or increase in effective diameter of the wire-wrapped fuel element, is 1–2 mm larger than the fuel element. This study assumes a wire wrap diameter of 1.5 mm, and the resulting practical minimum P/D values are given in Table 5.1 for the tube diameters of interest. Even with fixed P/D, increasing D corresponds to an increased volume fraction of fuel relative to cladding; allowing P/D to decrease with larger fuel D further increases the fuel volume fraction. The wire-limited minimum P/D is used for neutronic and thermal–hydraulic modelling of all configurations described in this chapter. The outer cladding thickness is fixed at 0.5 mm and the inner wall thickness is 0.3 mm for all configurations.

Table 5.1 Minimum practical pitch for 1.5-mm-wire wrap

Fuel D (mm)	Minimum pitch (mm)	Minimum P/D
10	11.5	1.15
20	21.5	1.075
30	31.5	1.05
40	41.5	1.038

5.1.2 Neutron balance analysis

For each pin cell depletion simulation, a neutron balance is calculated as the integral of k_{eff} with respect to burnup. The neutron balance calculation is conceptually similar to the linear reactivity model (LRM) for determining discharge burnup, and can be applied in cases of nonlinear burnup such as B&B reactors [9]. In the idealised continuous refuelling scenario, equilibrium operation requires the areas above and below the one-batch k_{eff} curve to be equal, corresponding to a neutron balance of zero at the discharge burnup.

While the neutron balance derived in this thesis is unitless and does not correspond to a physical quantity, it is a convenient measure to determine minimum burnup requirement and maximum burnup limit. Fresh fertile B&B fuel is a net neutron absorber, so a negative neutron balance accumulates at low burnup. As the fuel breeds fissile material and begins producing excess neutrons, its neutron balance begins to increase. The theoretical minimum discharge burnup B_{min} required to sustain B&B operation is reached when the neutron balance becomes positive, indicating that the fuel is a *net* producer of excess neutrons. The neutron balance eventually decreases as the fuel is depleted at even higher burnup, and the theoretical maximum discharge burnup B_{max} occurs when the quantity becomes negative again.

The neutron balance method enables the use of simple neutronic models for rapid scoping calculations to compare B&B performance of various fuel configurations. However, it is an approximate method that cannot provide the accuracy of a full-core model with realistic fuel management, power distribution, and neutron losses. The pin cell undergoes burnup at constant power density, and the neutron spectrum depends only on the composition of the pin cell. In a previous B&B study by Heidet and Greenspan, comparison of a unit cell depletion to a full-core model showed the full-core spectrum to be softer at low burnup, since fresh fuel at the core periphery absorbs the neutrons leaking out from the central fuel zones [24]. Similarly, power density of a fuel assembly would realistically increase as it is irradiated and moved toward the centre of the core. The unit cell neutron balance used in this chapter assumes an infinite-batch fuel shuffling scheme, in which feed fuel is continuously being replenished while burnt fuel is being discharged.

The neutronic feasibility assessment (Section 2.2) shows that neutron economy of the fuel can be tuned via its geometry and composition. Some configurations do not have enough breeding gain to ever establish a positive neutron balance, so they are not B&B-capable. For the natural (0.7% ^{235}U) and 5% enriched versions, which are subcritical at beginning-of-cycle, the objective of the present study is to identify the smallest B&B-capable tube diameters within practical engineering limits (e.g., materials and manufacturability considerations), since a smaller diameter corresponds to higher power density. In conventional B&B reactor

design, a common design aim is to minimise B_{min} because of the constraint on cladding fluence. For the BBMSR with easily replaceable cladding, the emphasis is instead on simultaneously achieving high fuel utilisation and competitive power density. To satisfy this objective, the neutron balance curve should peak at zero such that $B_{min} = B_{max}$.

Since the 20% enriched fuel version is already supercritical at beginning-of-cycle, it does not have a minimum burnup requirement, so the design objective is simply to achieve significantly better fuel utilisation than the LWR fuel cycle. The relationship between utilisation and power density is explored by comparing the characteristics of various fuel configurations with 20% enriched fuel.

5.1.3 Neutron reflectors

Previous studies of homogeneous, pool-type B&B MSR designs show that solid reflectors around the core can significantly reduce leakage and thereby reduce the required core volume for B&B operation [42, 26]. Assuming a 100 cm thick reflector layer on all sides of the core, lead is shown to be the most effective reflector material, followed by zirconium, and then steel. Gregg also finds fuel salt in the upper and lower plena to be an effective reflector, and suggests that internal steel components such as core support structures may contribute to neutron reflection [20]. These components were represented by a 20-cm thick layer of a 50–50% mixture of steel and fuel salt.

Since the fuel and coolant salt are separate in the BBMSR, coolant salt can be used to reflect neutrons without increasing the required uranium mass. (Additionally, a large coolant volume serves as a heat sink and may aid passive decay heat removal in accidents involving loss of pumping power, but quantitative analyses of these phenomena are reserved for future studies.) The BBMSR fuel is modelled with a 20-cm thick axial metal reflector and a coolant plenum of height L_{cool} above and below the fuel, so the total model height is $[2(20 + L_{cool}) + L_{fuel}]$ cm. The value of L_{cool} is varied to test the effect on neutronic performance. The solid reflector is modelled as an extension of the fuel element, having the same diameter as the cladding. This approximately represents a reflector layer above and below the fuel region, with space for coolant flow similar to the spacing between fuel elements, similar to the approach mentioned above with a 50–50% mixture of reflector and salt. The fuel expansion space described in Section 1.3.6 is neglected in the present analysis.

Elemental lead (Pb), zirconium (Zr), and iron (Fe; representing steel) are evaluated as solid reflector candidates for the BBMSR. Pb is modelled only as a reference case, since its low melting temperature (327°C) would make it difficult to incorporate as an axial reflector

in an MSR with high operating temperatures. Zr and Fe have melting temperatures in excess of 1000°C, so should be safely compatible with BBMSR coolant temperatures.

5.1.4 Thermal–hydraulic analysis

Using the thermal–hydraulic design search program described in Chapter 4, the maximum allowable channel power density can be found for a given fuel configuration, to inform the neutronic scoping study. A power density of 100 W/cm^3 is targeted for economically competitive reactor operation.

The MHT correlation developed for modelling heat transfer in the concentric fuel concept is only valid for $\Omega \leq 4.0$, but it becomes challenging to satisfy this requirement at realistic power densities for larger fuel diameters with $\varepsilon = 0.5$, corresponding to approximately equal volumes of the inner and outer concentric fuel sections. By increasing the value of ε so that the size of the inner fuel section increases relative to the overall fuel D, Ω can be reduced to less than 4.0. The maximum power densities reported in this chapter are calculated by adjusting ε as needed in the thermal–hydraulic model to satisfy $\Omega \leq 4.0$. (For simplicity, the geometry in all neutronic models uses $\varepsilon = 0.5$.)

Section 4.1.5 shows that for each fuel geometry there is a value of ε that optimises heat transfer performance. By increasing ε beyond this optimal value, the allowable power density q''' is reduced.

In general, higher power is allowed for shorter L_{fuel}, as shown in Section 4.3. However, since Ω decreases as L_{fuel} increases, the length–power trend is reversed at larger D when ε must be increased to satisfy $\Omega \leq 4.0$. In these configurations, longer L_{fuel} will have both higher power density and better neutronic performance than corresponding shorter versions, so the shorter versions can be eliminated from design consideration.

5.1.5 Code comparison: deterministic versus Monte Carlo

A code comparison analysis is performed to determine whether a computationally efficient alternative to Serpent can be used for carrying out neutronic design scoping with reasonable accuracy. WIMS 10 and a development version of WIMS 11 are used to compare results from several deterministic methods to the Monte Carlo code Serpent, described in Section 2.2.1. WIMS is a neutronics software package with a modular structure that allows different methods to be combined so that a specific model can be tailored to the problem being solved [3]. Serpent is assumed to provide a reference solution, so the discrepancy between WIMS and Serpent results is referred to in this section as the error of the WIMS calculation.

WIMS and Serpent results are compared for three types of pin cell model geometry:

1. Infinite 2D pin cell
2. Infinite 3D: axially heterogeneous with reflective boundaries
3. Finite 3D: axially heterogeneous with vacuum axial boundaries, to simulate axial leakage

Additionally within each geometry type, the codes are compared for two fuel configurations identified in Section 2.2, the neutronic feasibility assessment:

A. Natural uranium fuel in a 50 mm tube

B. 20% enriched uranium in a 10 mm tube

Figure 5.1 depicts the 2D pin cell model, with hexagonal $P/D = 1.182$ for both fuel configurations. The cladding material is SiC with a thickness of 0.5 mm, and the inner wall of the concentric fuel design is omitted for the code comparison calculations. In the 3D models, $L_{fuel} = 100$ cm and $L_{cool} = 30$ cm, so the total model height including fuel, coolant, and cladding is 160.1 cm. Table 5.2 gives the detailed dimensions of the two configurations. In both codes the fuel is modelled at 1200 K, and the cladding and coolant are modelled at 900 K. All Serpent simulations reported in this section use a population of 2000 neutrons with 50 inactive cycles and 500 active cycles. The mean Monte Carlo statistical errors are well below 100 pcm.

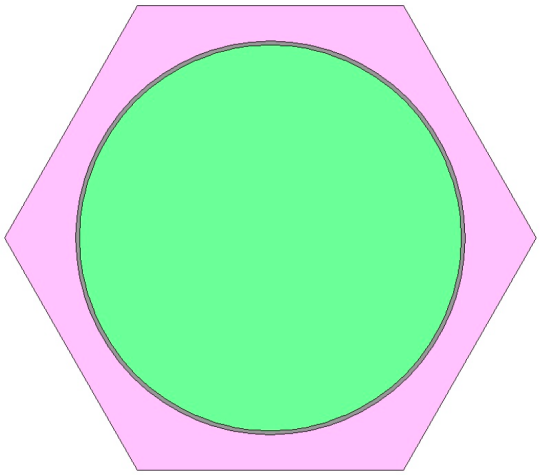

Fig. 5.1 2D pin cell geometry

Table 5.2 Dimensions of models for comparison of WIMS and Serpent

	Configuration A	Configuration B
Cladding outer diameter (mm)	10	50
Fuel diameter (mm)	9	49
Coolant hexagonal pitch (mm)	11.82	59.1
Equivalent coolant cylindrical diameter (mm)	12.41	62.06

Infinite 2D

For the infinite 2D model, WIMS 11 is executed with the module sequence: HEAD, WIMSECCO, CACTUS, and BURNUP. HEAD initialises the WIMS calculation by reading the specified materials and geometry, generating microscopic and macroscopic cross-sections, and performing an equivalence treatment of resonance shielding. The WIMSECCO module integrates the ECCO code to generate fine-energy (1968) group cross-sections, suitable for modelling fast spectrum systems. ECCO cross-sections are generated for ten nuclides: ^{235}U, ^{238}U, ^{239}Pu, ^{240}Pu, ^{241}Pu, ^{242}Pu, ^{241}Am, ^{37}Cl, C (natural), and Na (natural). These cross-sections replace those generated by HEAD, so the WIMSECCO output contains a mixture of HEAD and ECCO-generated cross-sections. Next, CACTUS uses the method of characteristics to solve the multigroup neutron transport equation and obtain the flux solution, followed by a depletion calculation in the BURNUP module. The entire sequence is repeated for each burnup step.

The WIMS and Serpent depletion calculations use 100 steps of 25 days each for a total of 2500 days burnup, or 6.8 years, with a cell power density of 150 W/cm^3. For fuel Configuration A the mean error between WIMS and Serpent is 484 pcm, and Figure 5.2a shows good agreement between the codes throughout burnup. For fuel Configuration B the mean error between codes is 332 pcm, and Figure 5.2b also shows good agreement throughout burnup.

Infinite 3D

The infinite 3D model is compared between Serpent and three different WIMS flux solvers: CACTUS3D, MERLIN, and MONK. As in the 2D case, WIMS is executed with HEAD, WIMSECCO, the flux solver, and BURNUP. The MERLIN module uses the SP3 approximation to solve the multigroup transport equation. MONK performs a Monte Carlo calculation using the WIMS 172-group cross-section data. (Since MONK is not yet available in the development version of WIMS 11, this model is run using WIMS 10. However, since ^{37}Cl is

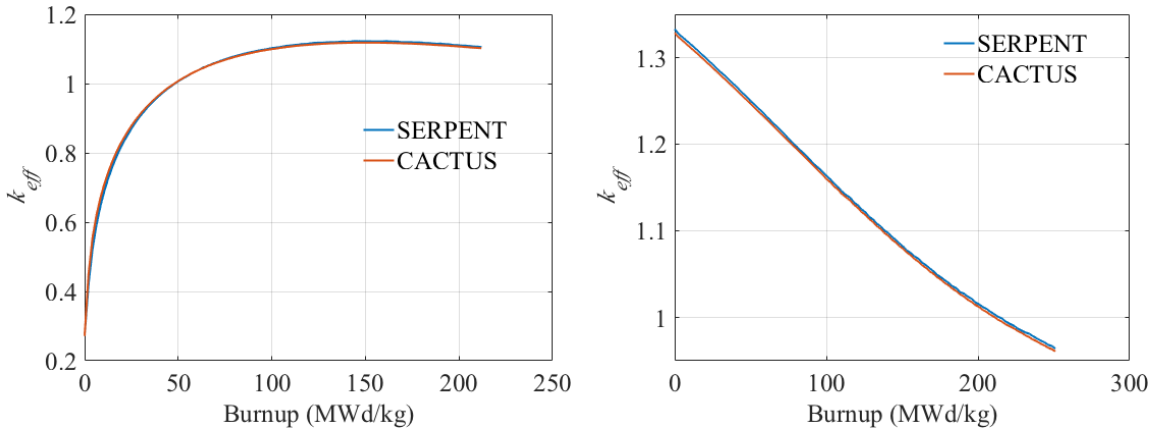

(a) Configuration A: natural U in 5 cm tube (b) Configuration B: 20% enriched U in 1 cm tube

Fig. 5.2 Infinite 2D result

not available in the ECCO library of WIMS 10, it is omitted from the list of ECCO nuclides in the calculation with MONK for both infinite and finite 3D.)

The geometry definition varies slightly between the flux solvers. MONK and CACTUS3D model 1/6 of the hexagonal pin cell, as shown in Figure 5.3. MERLIN can only model one type of geometry at a time, so the fuel, cladding, and coolant are all represented as nested cylinders, such that the volume of the coolant cylinder is equal to the volume of the original hexagonal cell. The equivalent cylinder diameter is listed in Table 5.2.

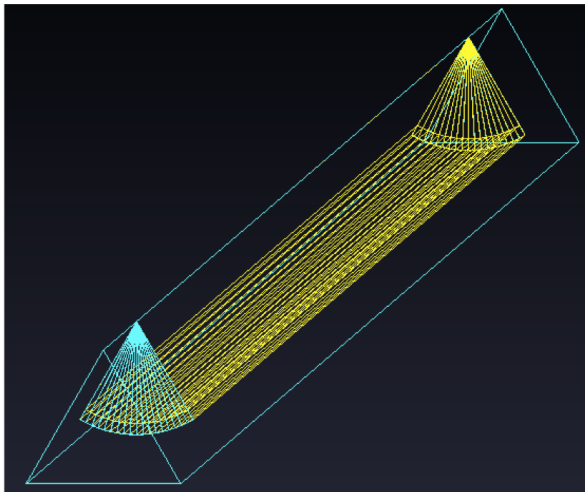

Fig. 5.3 3D pin cell geometry (1/6 symmetry in CACTUS)

The infinite 3D model results differ slightly from the infinite 2D, even though the axial boundaries are reflective, because of the axial heterogeneity with reflective coolant layers above and below the fuel. Figure 5.4a shows reasonable agreement between Serpent and

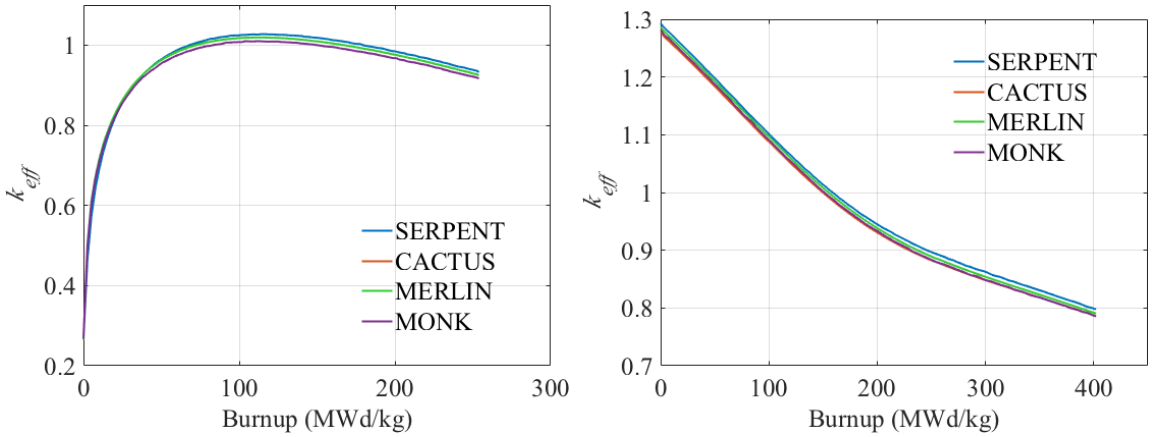

(a) Configuration A: natural U in 5 cm tube (b) Configuration B: 20% enriched U in 1 cm tube

Fig. 5.4 Infinite 3D result

WIMS for fuel Configuration A. The mean error from Serpent is 821 pcm for CACTUS3D, 822 pcm for MERLIN, and 1549 pcm for MONK. Figure 5.4b also shows reasonable agreement between the codes for Configuration B, with a mean error of 1372 pcm for CACTUS3D, 654 pcm for MERLIN, and 1184 pcm for MONK. While this is error is higher than would be expected for an LWR calculation, it is reasonable for the purposes of the design scoping study of BBMSR fuel configurations.

Finite 3D

A finite 3D model with vacuum axial boundaries is calculated in WIMS using HEAD, WIMSECCO, MERLIN, and BURNUP. Since CACTUS3D must use reflective boundaries on all faces, it would require the use of "artificial" materials to mimic a black boundary, which may introduce additional errors, so this method was not explored. The results for Configuration A (Figure 5.4a) show good agreement in the fresh fuel, but the Serpent and ECCO-MERLIN solutions quickly diverge, reaching an unacceptably high mean error of 6489 pcm. The burnup step length is reduced from 25 days to 5 days in both codes, but the mean error remains similar. The Serpent and WIMS–ECCO results for Configuration B (Figure 5.5b) show less divergence than Configuration A, with a mean error of 1523 pcm.

Two alternative WIMS calculation procedures are tested for modelling the finite 3D system. In the first, the subgroup treatment of resonance shielding is used in place of ECCO by executing the routine PRES–CACTUS–RES after HEAD [55]. (The full module sequence is HEAD, PRES, CACTUS, RES, MERLIN, and BURNUP.) In general, the subgroup method becomes exponentially slower as the number of nuclides increases, so only ^{235}U, ^{238}U, and

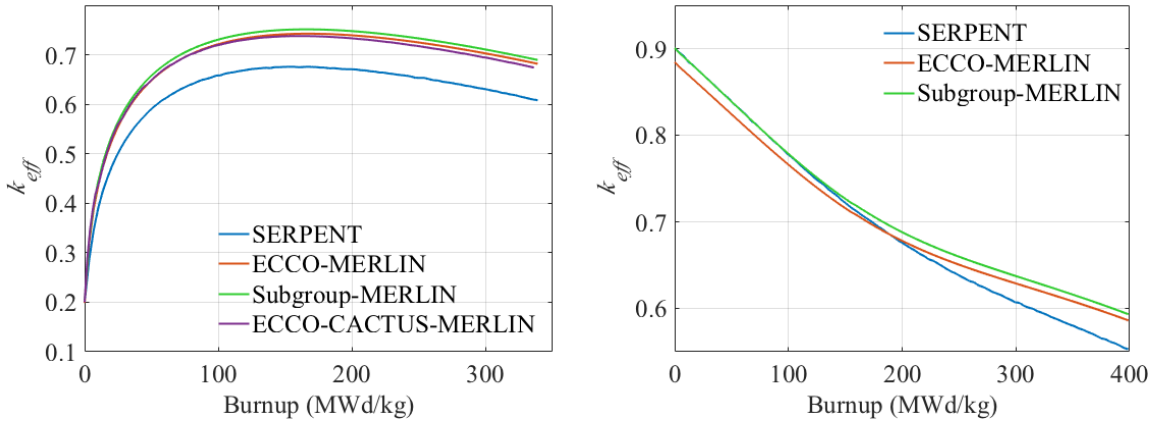

(a) Configuration A: natural U in 5 cm tube (b) Configuration B: 20% enriched U in 1 cm tube

Fig. 5.5 Finite 3D result

^{239}Pu are treated. The subgroup treatment is typically followed by condensation from 172 groups to a smaller number of groups (e.g., 22 groups) to speed up the calculation, but the condensation step is omitted to minimise sources of error for the comparison analysis. The subgroup-MERLIN results for Configurations A and B are included in Figures 5.5a and 5.5b, but they show no notable improvement over the ECCO–MERLIN calculation.

The second alternative WIMS calculation is HEAD–WIMSECCO–CACTUS(2D)–SMEAR–MERLIN, attempted only for Configuration A. CACTUS is used to perform the 2D lattice calculation to account for radial heterogeneity, followed by a 1D model in SP3 to represent the axial heterogeneity and leakage effects. For the 1D model, the fuel, coolant, and cladding are smeared into a single material that is the height of the fuel. The smeared material is bound at the top and bottom by heterogeneous layers of cladding, coolant, and vacuum axial boundaries. The k_{eff} result is obtained from the 1D SP3 model output, while burnup is performed on the 2D CACTUS output. In principle, this method preserves the pin-level detail better than using SP3 alone for the 3D calculation, but the results, included in Figure 5.5a, show very similar performance to the 3D SP3 calculations.

Conclusion of code comparison study

WIMS shows good agreement with Serpent for the infinite 2D pin cell, and could be used as a more computationally efficient alternative for 2D scoping. However, for the finite 3D pin cell with axial leakage, the results from all investigated WIMS methods differ from Serpent by more than 2000 pcm, an unacceptably high error. The source of the error could not be identified within the time limitations of this study.

Serpent is executed in parallel mode on the Cambridge Service for Data Driven Discovery (CSD3), a high performance computing platform. The calculations for comparison with WIMS were performed with 2000 neutrons and 100 burnup steps, which takes around one hour to complete using 16 CPUs. However, through personal communication the developers of Serpent advised that the neutron population size be increased to 20,000 for the 3D pin cell model, for improved parallel performance and accuracy. To compensate for the resulting increased computational requirement, the burnup time step resolution is decreased. Using 15 to 20 total burnup steps (depending on the burnup potential of the configuration) results in negligible loss of accuracy compared to 100 steps. Running in parallel on 32 CPUs on CSD3, a 3D pin cell depletion takes approximately two hours, and the Monte Carlo statistical errors are below 20 pcm. These updated Serpent settings are used for all calculations reported in the following sections.

5.2 Design with Natural Uranium

A B&B-capable fuel tube configuration with natural uranium feed fuel is found by systematically varying the cladding material, fuel diameter, fuel length, reflector material, and coolant length. The influence of each of these parameters on the overall neutronic performance is examined and also used to inform the design of the 5% and 20% enriched versions.

5.2.1 Effect of cladding material

An initial reference fuel configuration is defined with $D = 20$ mm, $L_{fuel} = 300$ cm, $L_{cool} = 100$ cm, 20-cm iron (Fe) axial reflector, and silicon carbide (SiC) cladding and inner wall. The cladding materials natural molybdenum (Mo), low-capture molybdenum-94 (Mo94) (discussed in Section 2.2.4), and stainless steel 310 (SS310) are evaluated against the reference. The neutron balance results in Figure 5.6 show that while none of the configurations with the given geometry establish a positive neutron balance, SiC cladding results in the best neutron economy, while Mo severely impairs breeding performance due to neutron capture. A fourth case uses SiC cladding but no inner wall, and it shows significantly better neutron economy than the reference case, demonstrating the neutronic penalty of the inner wall. This comparison reveals high neutronic sensitivity to the cladding material. While SiC is relatively neutronically transparent, the cladding and inner wall should be made as thin as structural requirements will allow. Since these requirements are not yet known for the BBMSR, the

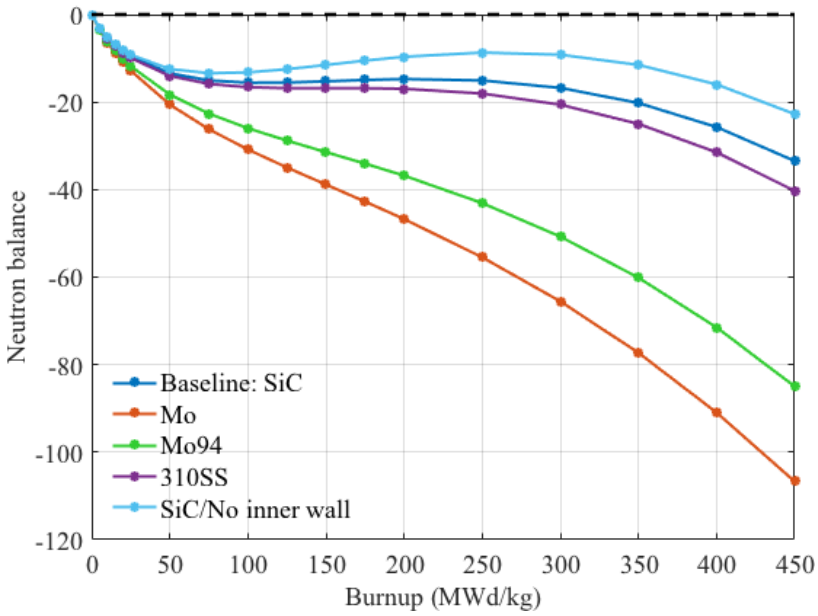

Fig. 5.6 Effect of cladding material

assumed dimensions of 0.5 mm and 0.3 mm thick cladding and inner wall, respectively, are maintained for the remaining analysis, with SiC as the preferred cladding material.

5.2.2 Effect of fuel diameter

The reference configuration used to investigate the influence of fuel diameter is identical to the reference case for the cladding effect, with $D = 20$ mm, $L_{fuel} = 300$ cm, $L_{cool} = 100$ cm, 20-cm axial Fe reflector, and SiC cladding and inner wall. The tube diameter D is varied to 10, 30, and 40 mm, with the results shown in Figure 5.7. Only the 40 mm case establishes a positive neutron balance, but thermal–hydraulic analysis is needed to determine the viability of this configuration. The 10 mm configuration is eliminated due to poor neutronic performance, and the thermal–hydraulic design search program is used to determine the maximum allowable power density for the 20, 30, and 40 mm cases. The corresponding maximum channel power density and ε values required for $\Omega \leq 4.0$ are given in Table 5.3. Based on these results, the 40 mm configuration is eliminated due to its very low power density. The power density of the 30 mm case is also significantly lower than the target value of 100 W/cm^3. Moderately low power density may be worthwhile to enable use of natural uranium fuel, if additional modifications can make it B&B-capable, so the configuration with $D = 30$ mm is carried forward as the new reference case.

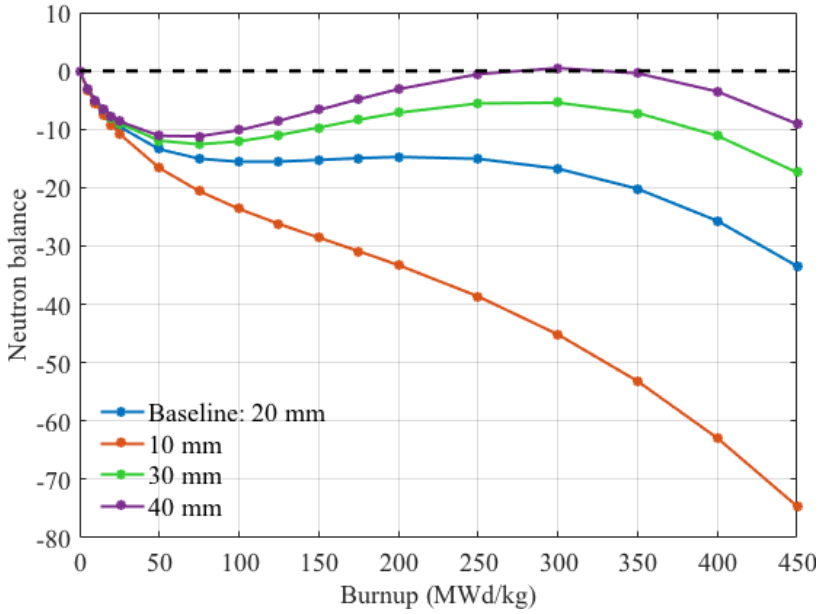

Fig. 5.7 Effect of fuel diameter

Table 5.3 Achievable power densities for fuel diameter comparison

D (mm)	Power density (W/cm^3)	ε
20	121	0.53
30	57	0.73
40	33	0.82

5.2.3 Effect of fuel length

Following the fuel diameter analysis, the new reference configuration has $D = 30$ mm, $L_{fuel} = 300$ cm, $L_{cool} = 100$ cm, 20-cm Fe axial reflector, and SiC cladding and inner wall. The fuel length L_{fuel} is varied to 200 cm and 400 cm. Fuel elements of up to 400 cm length have been manufactured for other reactor designs, so this is assumed to be the practical upper limit of L_{fuel} [52]. Figure 5.8 shows that only the 400-cm tall fuel establishes a positive neutron balance. This configuration, which allows a power density of 64 W/cm^3 with $\varepsilon = 0.68$, is carried forward as the new reference case.

5.2.4 Effect of reflector material

The reference configuration has $D = 30$ mm, $L_{fuel} = 400$ cm, $L_{cool} = 100$ cm, 20-cm Fe axial reflector, and SiC cladding and inner wall. The reflector materials Pb and Zr are evaluated against the reference. A fourth case, included as a lower bound of reflector performance,

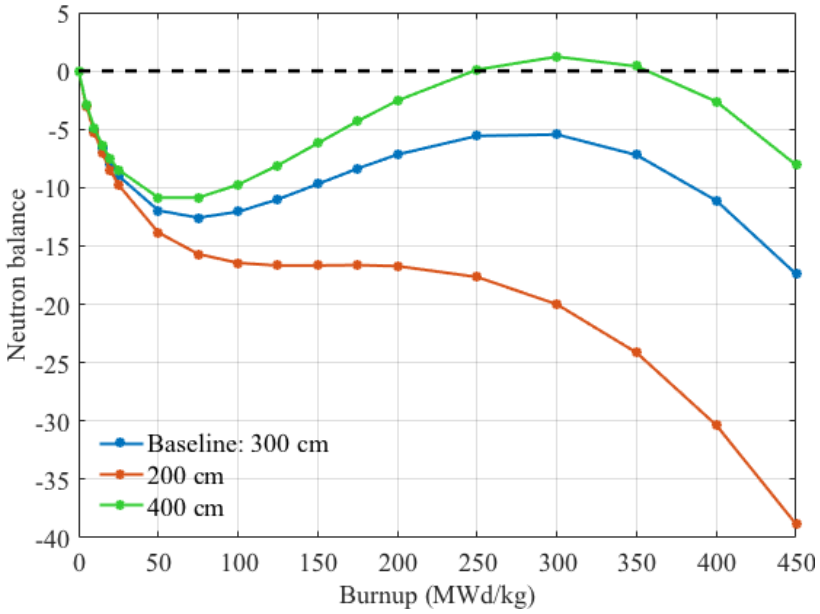

Fig. 5.8 Effect of fuel length

contains only coolant salt in place of a solid reflector, with a total coolant length of 120 cm. The results in Figure 5.9 show that Fe (representing steel) performs only marginally better as a reflector than coolant salt. While Pb is shown to be the best reflector, Zr is nearly as effective and is a more practical material for a high-temperature MSR.

Since the configuration with Zr reflector yields a small neutron balance excess beyond B_{min}, the fuel diameter can be decreased slightly to allow higher power density. It is found that D can be reduced to 28 mm while still achieving a positive neutron balance near $B_{min} =$ 300 MWd/kg, which increases the power density to 73 W/cm^3, so this configuration becomes the new reference.

5.2.5 Effect of coolant plenum length

The sensitivity to length of the coolant plena above and below the core is tested by varying L_{cool} from the current reference of 100 cm, to 50 and 150 cm. The results in Figure 5.10 show that extending L_{cool} from 100 to 150 cm makes virtually no difference. Decreasing it to 50 cm reduces neutron economy very slightly, but the reduction in overall core volume should reduce capital costs, so $L_{cool} = 50$ cm is adopted. The final fuel configuration using natural uranium is summarised in Table 5.4.

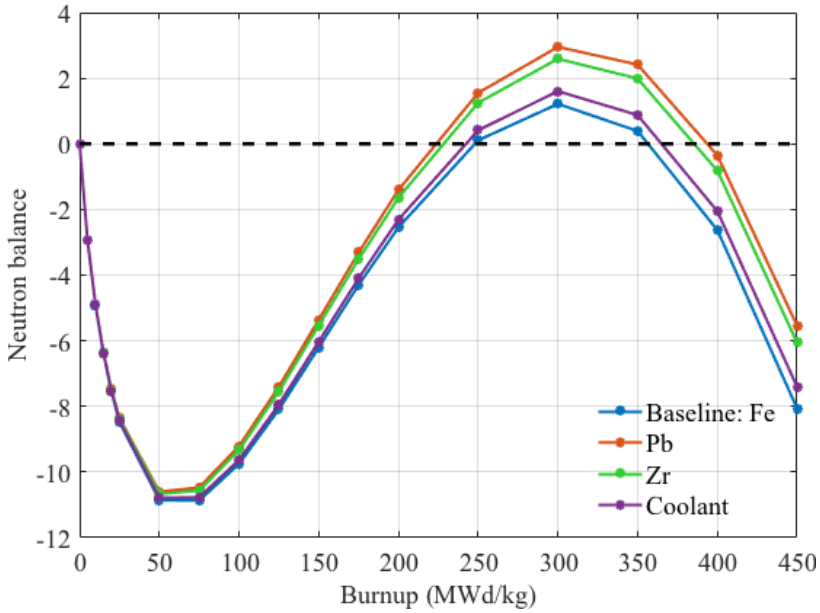

Fig. 5.9 Effect of reflector material

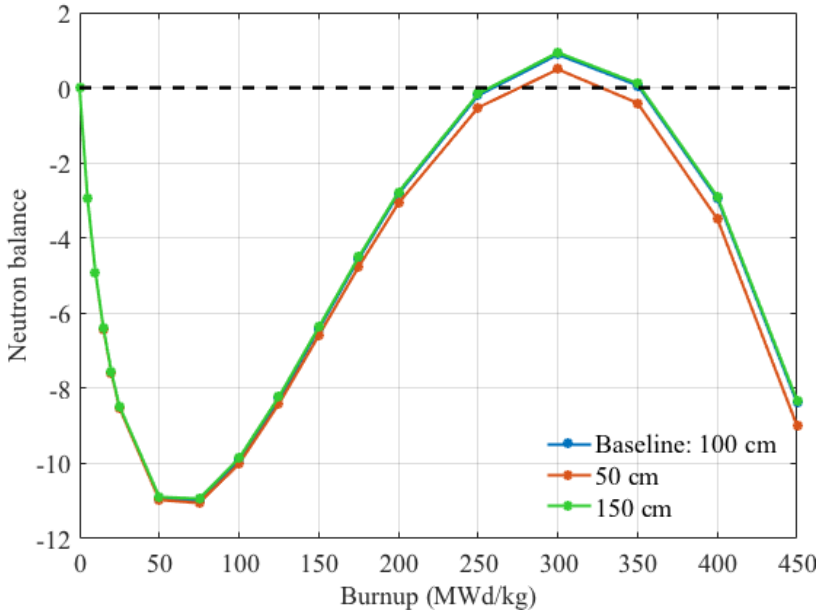

Fig. 5.10 Effect of coolant length

5.3 Design with 5% Enriched Uranium

The neutronic feasibility assessment (Section 2.2) shows that low enrichment in the BBMSR fuel increases the initial k_∞ slightly, though at higher burnup k_∞ converges to nearly the same value as the natural uranium case. The initial reactivity boost results in a less negative neutron balance at low burnup, so a net positive neutron balance can be achieved with a smaller tube diameter, and the power density can be increased. The final configuration identified for natural uranium feed fuel, given in Table 5.4, is used as an initial reference configuration for 5% enriched uranium feed fuel, and the diameter is gradually decreased. Figure 5.11 shows that D can be reduced from 28 mm to 26 mm while maintaining a positive neutron balance at 300 MWd/kg, which allows the channel power density to be increased from 73 W/cm^3 to 86 W/cm^3. The final configuration for 5% enriched feed fuel is summarised in Table 5.4.

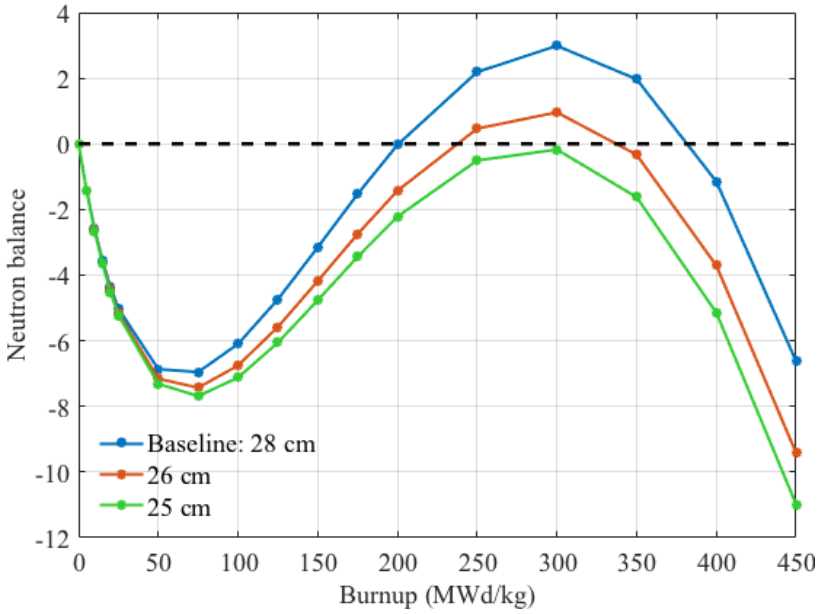

Fig. 5.11 Neutron balance of 5% enriched fuel configurations

5.4 Design with 20% Enriched Uranium

The BBMSR with 20% enriched feed fuel already has a positive neutron balance just after beginning-of-cycle, so the neutron balance method is used to determine the theoretical maximum burnup B_{max}, rather than B_{min}. If fuel utilisation and power density can be significantly improved compared to LWRs, enrichment up to 20% may be justifiable. The trade-off between power density and fuel utilisation is explored by modelling the neutronic

Table 5.4 Fuel configurations with natural and 5% enriched fuel

	Natural (0.7% ^{235}U)	5.0% ^{235}U
Fuel diameter, D (mm)	28	26
P/D	1.054	1.058
ε	0.65	0.61
Fuel length, L_{fuel} (cm)	400	400
Coolant length, L_{cool} (cm)	50	50
Power density (W/cm^3)	73	86
B_{min} (MWd/kg)	277	250
U (MWd/kgU$_{\mathrm{NAT}}$)	300.0	25.5

and thermal–hydraulic performance of fuel diameters between 10 and 20 mm, with $L_{fuel} =$ 200, 300, and 400 cm. Like the natural and 5% enriched versions, all configurations have a 20-cm Zr reflector and $L_{cool} = 50$ cm above and below the fuel element. Figure 5.12 shows neutron balance results for a range of configurations with 20% enriched fuel.

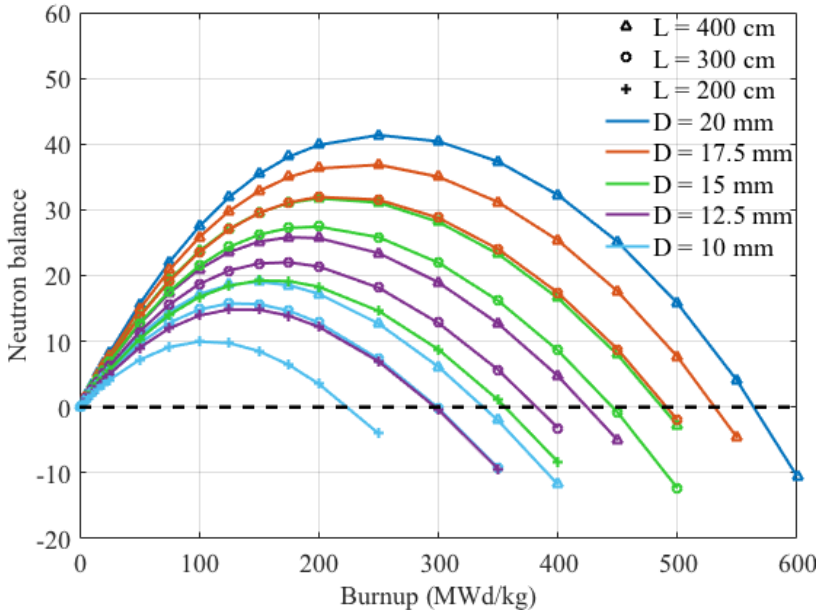

Fig. 5.12 Neutron balance of 20% enriched fuel configurations

B_{max} of each configuration is identified where the neutron balance crosses the axis, and the maximum power densities are calculated using the thermal–hydraulic design search program. Fuel configurations that have a smaller power density than their longer fuel counterparts with the same D have been eliminated, since shorter L_{fuel} always worsens neutronic performance. Table 5.5 gives the calculated power density and B_{max} values of the remaining configurations.

Table 5.5 Thermal–hydraulic & neutronic performance of 20% enriched fuel configurations

L_{fuel} (cm)	D (mm)	Power density (W/cm^3)	B_{max} (MWd/kg)	U (MWd/kgU$_{\mathrm{NAT}}$)
400	20	131	569	11.5
400	17.5	140	531	10.8
300	17.5	142	491	10.0
400	15	145	487	9.9
300	15	150	446	9.1
200	15	152	356	7.2
400	12.5	152	423	8.6
300	12.5	157	382	7.8
200	12.5	162	294	6.0
400	10	163	330	6.7
300	10	169	299	6.0
200	10	175	223	4.5

The relationship between the two parameters is shown in Figure 5.13, revealing a distinct trade-off between power density and B_{max}.

Upon closer inspection of the 20% enriched configuration results, it can be seen that shortening L_{fuel} produces a small power density increase but a significant B_{max} penalty. For example, with $D \leq 15$ mm, shortening from $L_{fuel} = 400$ cm to 200 cm allows a 5% power density increase, but causes 25% reduction in B_{max}. For most of the modelled configurations, an alternative geometry with longer L_{fuel} and smaller D exists that allows similar power density but higher B_{max}. For instance, 10 mm $\times$ 300 cm and 10 mm $\times$ 400 cm both feature better neutronic and thermal–hydraulic performance than 12.5 mm $\times$ 200 cm.

While the neutron balance method estimates the infinite-batch burnup potential, the finite-batch burnup can also be estimated for the 20% enriched fuel using the LRM [9], since k_{eff} is nearly linear with burnup, as Figure 5.14 shows. Where B_1 is the single-batch burnup and n is number of batches, the discharge burnup B_d is calculated as:

$$B_d(n) = B_1 \frac{2n}{n+1} \tag{5.1}$$

To facilitate comparison with the typical 3-batch LWR fuel cycle, $B_d(3)$ is estimated for the 20% enriched BBMSR fuel. In the next section, estimated $B_d(\infty)$ (i.e., B_{max}) and $B_d(3)$ are used to calculate theoretical and more realistic uranium utilisation values, respectively.

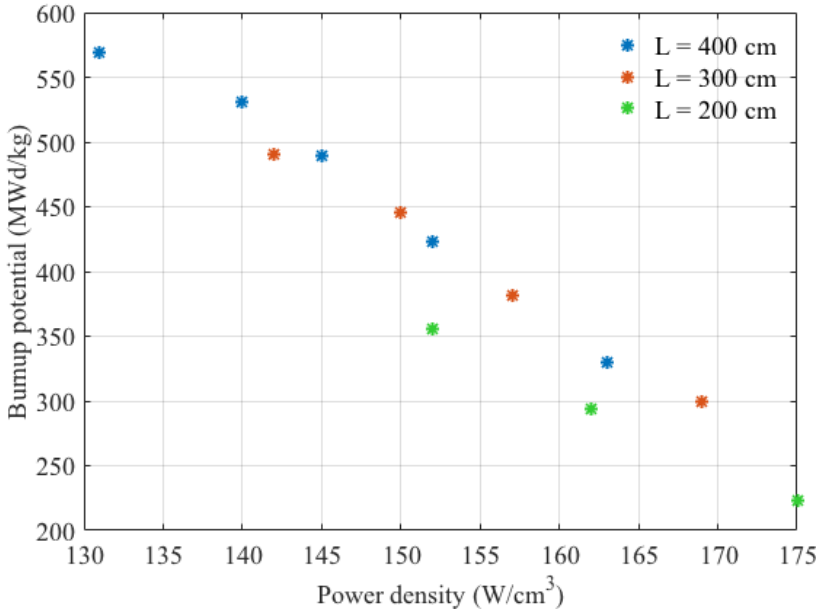

Fig. 5.13 Power density versus burnup potential of 20% enriched fuel configurations

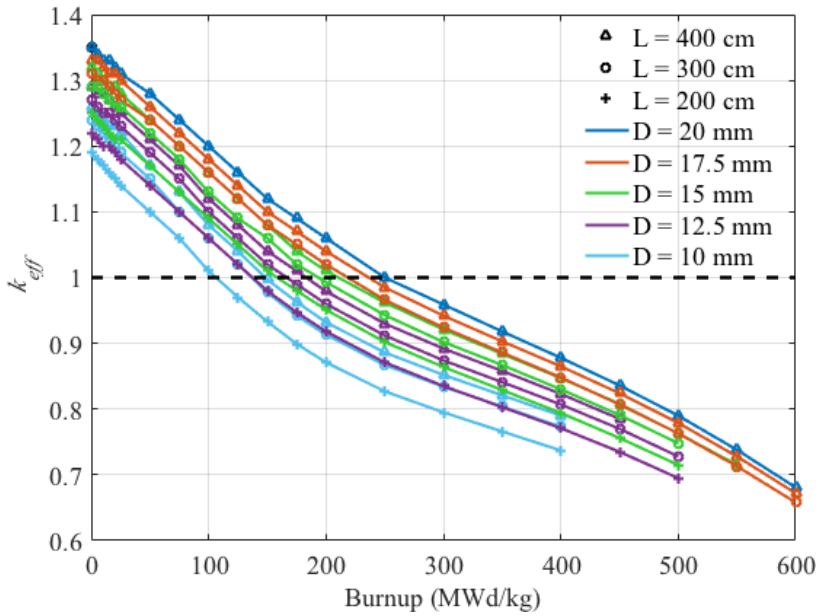

Fig. 5.14 Criticality of 20% enriched fuel configurations

5.5 Uranium Utilisation Analysis

For assessment of resource utilisation efficiency, the estimated BBMSR burnup values cannot be compared directly to LWR burnup, since their uranium enrichments differ. More natural uranium feedstock is consumed to produce higher enrichment levels, so the fuel burnup must be normalised to the mass of natural uranium required [80]. The uranium utilisation index U of each option is calculated based on discharge burnup, B_d, and uranium enrichment:

$$U = B_d \left(\frac{x_f - x_w}{x_p - x_w} \right), \mathrm{MWd/kgU_{NAT}} \tag{5.2}$$

where x_f, x_w, and x_p are the weight percent of ^{235}U in the feed, waste, and product streams of the enrichment process, respectively. The feed is natural uranium, so $x_f = 0.7$, and the waste stream is typically assumed to be $x_w = 0.3$. The product stream is the enriched uranium used in the reactor fuel, with x_p equal to the enrichment percentage.

To calculate U of the final configurations with natural and 5% enriched fuel from Table 5.4, B_{min} is rounded up to 300 MWd/kg. B_{min} of these two fuel options is approximately equivalent by design, so that the 5% version can achieve increased power density. For the natural fuel U is simply 300 $\mathrm{MWd/kgU_{NAT}}$. For the 5% enriched fuel, U is calculated as 25.5 $\mathrm{MWd/kgU_{NAT}}$, nearly an order of magnitude smaller.

Two sets of U are calculated for the 20% enriched fuels: a theoretical U_{max} based on B_{max} from the neutron balance method, and a conservative U_3 based on $B_d(3)$ estimated by the LRM. For the BBMSR, theoretical burnup potential is approximately 1.5 times larger than 3-batch burnup. In comparison, for an LWR with perfectly linear reactivity–burnup behaviour, the LRM predicts a factor of 1.33 difference between infinite-batch and 3-batch burnup. This is because the k_{eff} curves of the 20% BBMSR fuels flatten slightly at higher burnup due to breeding.

In LWRs, the achievable burnup depends to some extent on the reactor design, but it is mainly a function of fuel enrichment [80]. Figure 5.15 shows LWR uranium utilisation as a function of enrichment and various fuel management parameters. (Note that the ordinate must be multiplied by 1.3 to obtain $\mathrm{MWd/kgU_{NAT}}$ [9].) The maximum 3-batch utilisation U_3 is 5.5 $\mathrm{MWd/kgU_{NAT}}$, while the infinite-batch utilisation U_{max} is approximately 7.15 $\mathrm{MWd/kgU_{NAT}}$, both occurring at enrichments between 4–5%. The BBMSR utilisation values can be compared to the corresponding optimal uranium utilisation values of the LWR fuel cycle.

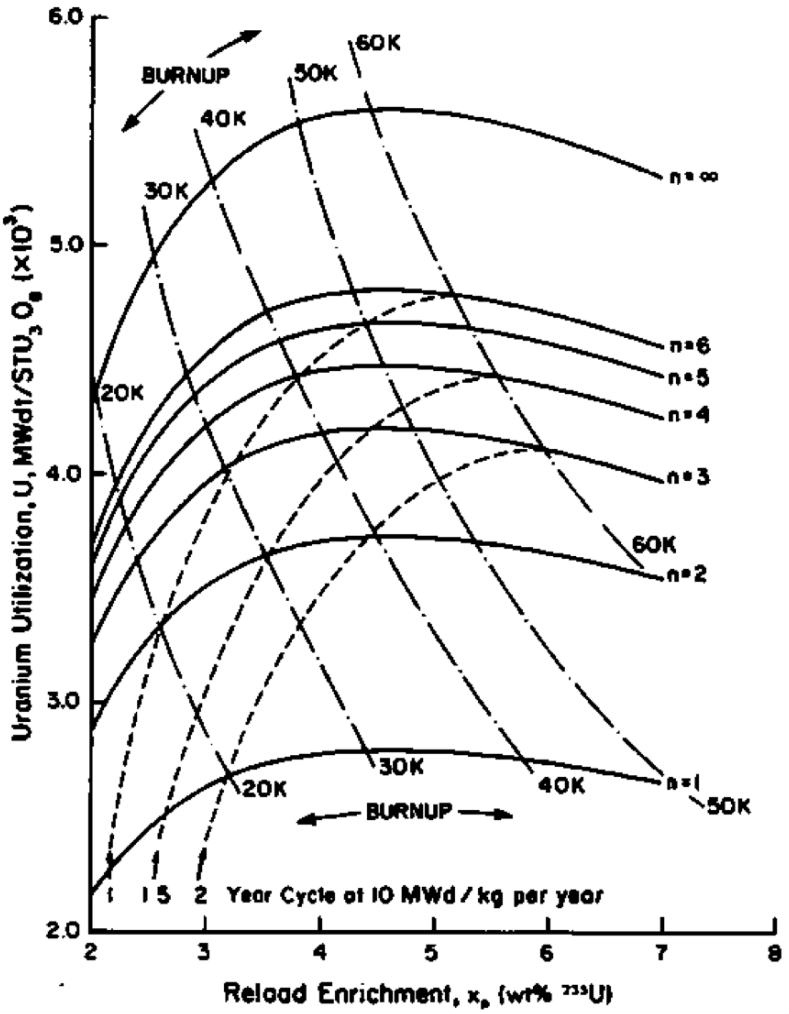

Fig. 5.15 LWR uranium utilisation as a function of fuel management parameters. (Note: Multiply ordinate by 1.3 to obtain $\mathrm{MWd/kgU_{NAT}}$) [9]

The trade-off between fuel utilisation and power density is compared across all BBMSR fuel cycle options, in addition to a typical pressurised LWR with a power density of 104 $\mathrm{W/cm^3}$ [80]. Figure 5.16 shows that natural and 5% enriched BBMSR fuels enable dramatically better fuel utilisation than the LWR cycle, albeit with significant reduction of power density. All of the 20% enriched BBMSR fuel configurations are capable of higher power densities than the typical LWR, and several also enable modest uranium utilisation improvements. Table 5.6 lists the 20% enriched configurations that yield $U_{max} > 8$ and $U_3 > 6\ \mathrm{MWd/kgU_{NAT}}$.

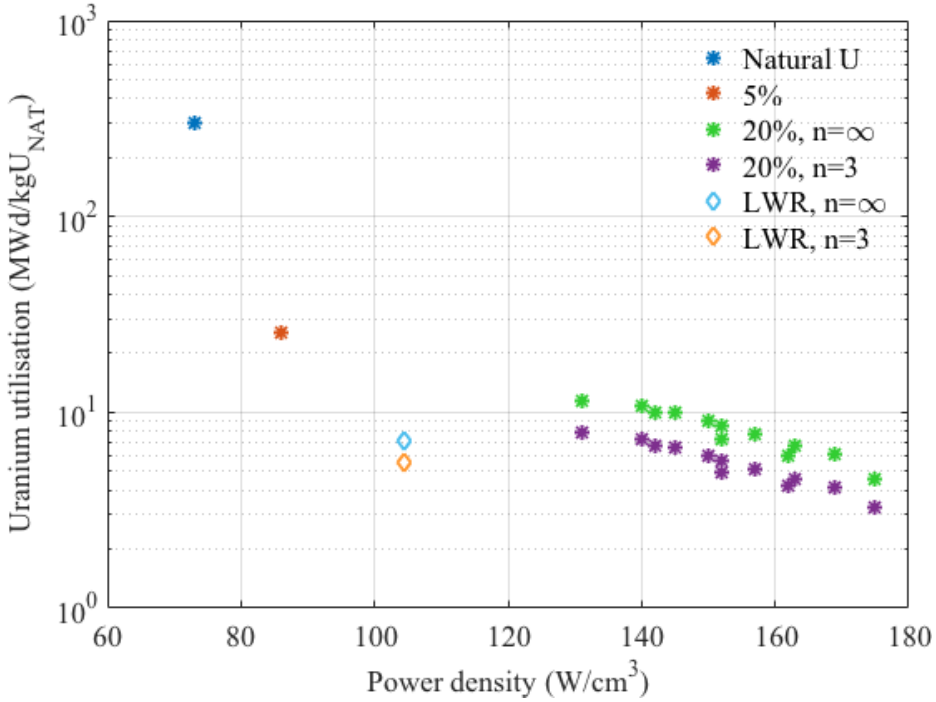

Fig. 5.16 Power density versus uranium utilisation capabilities of BBMSR fuel concepts

Table 5.6 High utilisation 20% enriched fuel configurations

L_{fuel} (m)	D (mm)	Power density (W/cm^3)	U_{max} (MWd/kgU$_{NAT}$)	U_3 (MWd/kgU$_{NAT}$)
LWR		104	7.15	5.5
4	20	131	11.6	7.9
4	17.5	140	10.8	7.3
4	15	145	9.9	6.7
3	17.5	142	10.0	6.6
3	15	150	9.1	6.0

5.6 Summary of BBMSR Fuel Cycle Options

Key metrics are compared for the range of BBMSR fuel enrichment options. The optimal natural uranium and 5% enriched configurations are found in Table 5.4. For 20% enrichment, the case from the last row of Table 5.6 is selected for comparison, representing the BBMSR configuration with the highest achievable power density of those with better uranium utilisation than an LWR. Table 5.7 summarises design and performance attributes of these three BBMSR options, based on each configuration's maximum theoretical discharge burnup with continuous refuelling, and using the adjusted value of ε as described in Section 5.1.4. Calculated values including $GW_e yr$ assume 33% power conversion efficiency for a LWR and 40% efficiency for the BBMSR, based on its high outlet temperature. The critical core dimensions are likely to vary between these options, but the core radius has not been quantified in this study, since all analysis is based on a single channel, and it is assumed that the core size can be scaled as needed by adding fuel assemblies. B&B core sizing must account for numerous neutronic considerations, including neutron leakage, fuel management, and neutronic efficiency. Additional thermal–hydraulic considerations may include the effect of core aspect ratio on pumping power requirements, natural circulation decay heat removal, and target core power rating.

Table 5.7 Key parameters of BBMSR fuel cycle options

	Natural U	5% enriched	20% enriched
Fuel diameter (mm)	28	26	15
Fuel length (m)	4	4	3
Power density (W/cm^3)	73	86	150
B_d (MWd/kg)	300	300	466
U (MWd/kgU_{NAT})	300	25.5	9.1
Actinide loading (kg/MW_{th})	28.6	23.9	11.6
Fuel volume fraction	0.73	0.72	0.61
Coolant volume fraction	0.18	0.19	0.25
SiC volume fraction	0.09	0.09	0.14
Discharged uranium ($kg/GW_e yr$)	1716	1726	857
Discharged TRU ($kg/GW_e yr$)	372	368	244

While the 20% enriched case achieves the lowest uranium utilisation of the selected options, its higher discharge burnup per unit energy produced corresponds to a significantly smaller mass of discharged uranium and TRU per unit of energy produced, which may improve its proliferation resistance and reduce the required repository size. Radiotoxicity

of the discharged fuel is also evaluated as an indicator of radiological hazard and repository requirements. Figure 5.17 compares the ingestion radiotoxicity per unit of energy produced for the three BBMSR fuel cycle options and a typical LWR with discharge burnup 50 MWd/kg. The radiotoxicity of natural uranium required to fuel a typical LWR, 5.9×10^6 $\mathrm{Sv/GW_e yr}$, is included as a reference level [13]. While the discharged fuel of the natural uranium and 5% enriched cases have slightly lower initial radiotoxicity, there is not a notable difference in the long-term characteristics of the compared once-through fuels.

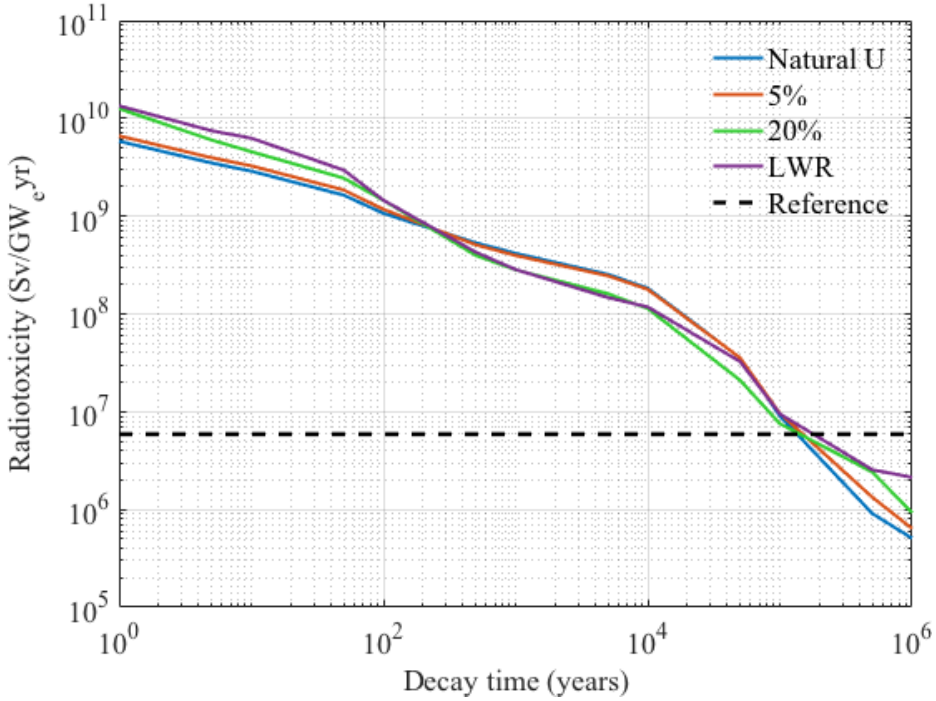

Fig. 5.17 Ingestion radiotoxicity of discharged fuel from BBMSR fuel cycle options

5.7 Conclusions

The fuel design scoping study applies the modelling tools developed in previous chapters to determine the achievable neutronic and thermal–hydraulic performance in the BBMSR fuel. The power densities from the thermal–hydraulic design search model account for the channel volume, calculated as the channel area times the active fuel height. While this formulation of power density is commonly used for comparing and evaluating reactor designs, it is noted that the overall system power density will be lower than the reported values once the height of the solid reflector and coolant plena are included.

A neutron balance calculation allows use of a unit cell model to quickly approximate the minimum burnup needed to sustain criticality. The 3D pin cell models simulated with Serpent include axial leakage but assume zero radial leakage. The actual leakage probability of the reactor will depend on core dimensions, discharge burnup, and fuel shuffling scheme. Additionally, neutron absorption in reactor structural materials and control rods is not accounted for. Losses to control rods in the BBMSR may be quite small, since passive reactivity feedback by thermal expansion of the molten fuel may minimise the need for active reactivity control during reactor operation. Full-core modelling that includes these factors is beyond the scope of this thesis.

Fuel configurations for natural and 5% enriched uranium are developed that maximise power density within the requirements of B&B operation. For 20% enriched uranium the design space can be expanded, and several fuel configurations are identified that range from high power density to high burnup potential. The key results of the design study are captured by comparing the competing objectives of fuel utilisation and power density. Higher uranium enrichment allows fuel diameters to be reduced, which enables higher power densities. However, higher enrichment corresponds to less efficient utilisation of natural uranium, so there is a strong trade-off between utilisation and power density.

The once-through BBMSR fuel cycle can achieve moderate to significant fuel utilisation improvements over the current once-through LWR cycle, with a range of possible power densities. The optimal economic balance between fuel utilisation and power density depends on various market factors such as the price of uranium, price of electricity, and capital costs. While the cost of uranium is currently a negligible contributor to the lifetime-levelised cost of nuclear energy, uranium scarcity and price escalation in the future could shift economic priorities towards high fuel utilisation. The fuel options identified in this chapter demonstrate the flexibility of the BBMSR to respond to these potentially shifting priorities.

Chapter 6

Summary and Conclusions

Less than 1% of mined uranium is fissioned in the once-through LWR fuel cycle. Spent LWR fuel has a high residual energy content that can be recycled into MOX fuel, but the cost of MOX fabrication is high and uranium savings are modest. The Generation IV International Forum has identified the long-term availability and sustainability of nuclear power as being among the top priorities for the next generation of nuclear reactors. In addition, significant reduction of proliferation potential is a key Generation IV objective.

Fast breeder reactors operating in a closed fuel cycle have been developed as a way to consume LWR wastes and extend resource availability. Reprocessed plutonium from LWR spent fuel is used to start up fast reactors, and eventually the fast reactor spent fuel is itself reprocessed and recycled. However, enrichment and reprocessing generate high-level wastes, and also introduce risk of radiation exposure and proliferation during the handling and processing of fissile material.

The once-through B&B fuel cycle can be used to limit the environmental and proliferation risks associated with reprocessing and uranium enrichment, while improving fuel sustainability compared to the LWR once-through cycle. A B&B reactor is a fast reactor variant that uses primarily fertile feed fuel to breed its own fissile fuel, achieving high uranium utilisation comparable to conventional fast reactors. Partially burnt assemblies containing bred fissile material sustain the chain reaction by supplying excess neutrons to regions of fresh fuel containing only fertile isotopes. Enrichment and reprocessing are avoided, so fuel cycle costs, proliferation risks, and environmental impacts are reduced. A significant challenge in existing B&B reactor designs is the lack of available fuel and cladding materials that can withstand the high minimum burnup required to sustain criticality.

The BBMSR with a dual-salt configuration is proposed to meet the Generation IV objectives of improved fuel utilisation, waste management, and proliferation resistance by

integrating the advantages of B&B and MSR technologies. MSRs allow high temperature operation at atmospheric pressures, flexible fuel cycle operation, and inherent safety due to strongly negative reactivity feedback. However, long-term corrosion resistance of structural materials exposed to fuel salt remains to be demonstrated. A BBMSR configuration using two separate salts is based on a design by Moltex Energy, in which a naturally convecting fuel salt is contained in individual fuel tubes, cooled by an external salt. Natural convection of the fuel aids heat transfer to the coolant, and the cladding tubes may be easily replaced to achieve high fuel burnup. This configuration of the BBMSR offers solutions to the significant materials challenges of traditional MSRs and B&B reactors.

In this thesis, the neutronic and thermal–hydraulic feasibility of the BBMSR is investigated. Tailored models have been developed to characterise heat transfer from the naturally convecting fuel, and to identify the maximum allowable power density. Fuel pin designs for natural uranium and LEU versions are developed and assessed compared to the LWR standard for fuel utilisation and power density.

6.1 Concept Description

Potential advantages of the BBMSR compared to previous B&B designs include inherent negative reactivity feedback and ease of cladding replacement to enable high burnup. Natural convection of the BBMSR fuel produces an axially homogeneous fuel composition, which may in practice allow a lower minimum burnup than for a solid fuel with axial burnup peaking.

6.1.1 Comparison of dual-salt and pool-type MSRs

Table 6.1 summarises key differences between the two types of MSR configurations.

Table 6.1 Comparison of dual-salt and pool-type MSR configurations

	Pool-type	Dual-salt
Fuel volume fraction	100%	60–75% (BBMSR)
Core arrangement	Homogeneous fuel salt	Heterogeneous fuel assemblies
Fuel management	Refuelling rate	Shuffling and refuelling
DNP distribution	Drift to external circuit	In-core only
Energy distribution	Direct heating of salt	Heat transfer, fuel to coolant

In a pool-type MSR, a fuel salt volume fraction of nearly 100% enables high fuel density for efficient breeding in B&B mode, which may allow the fuel salt to be diluted with a carrier salt that enhances thermal–hydraulic and chemical performance. However, fuel management is largely limited to the rate of refuelling and fission product removal, since the core contains a homogeneous mixture of low- and high-burnup fuel. A large actinide inventory may be required, since the fuel salt fills the entire reactor vessel and external circuit. All structural and auxiliary components of the reactor in contact with fuel salt are subject to increased rates of corrosion and irradiation damage compared to a clean molten salt. Drift of DNPs to the external circuit reduces the effective delayed neutron fraction, causes neutronic sensitivity to pump speed, and requires shielding of the external circuit.

In contrast, the smaller fuel volume fraction of the dual-salt configuration results in reduced heavy metal density and increased scattering and absorption in non-fuel materials, which reduce neutron economy and soften the neutron flux spectrum. However, the heterogeneous configuration enables the use of traditional fuel management, where assemblies of varying burnup levels can be radially zoned for improved breeding and burning performance. Containment of the fuel in assemblies also reduces irradiation and corrosion damage to non-fuel components, and confines DNPs to the core.

In terms of heat removal, power density is limited in the dual-salt system by the finite rate of heat transfer between fuel and coolant, whereas the pool-type configuration allows fission energy to be deposited directly into the fuel/coolant salt. The heat transfer lag of the dual-salt system may be beneficial for fast-spectrum reactivity feedback, since heating of the fuel may cause it to expand and moderate reactivity before the coolant temperature rises enough to reduce its density and harden the spectrum.

6.1.2 Neutronic feasibility

The neutronic feasibility of B&B operation in the dual-salt BBMSR concept is assessed using burnup calculations of a infinite lattice pin cell model. Beginning from an initial configuration based on the Moltex SSR with ZrF_4–NaF–KF coolant, the heavy metal density is improved by increasing the diameter to 10 mm to 50 mm and the UCl_3 concentration from 40 to 100 mol%. A neutron balance analysis reveals high rates of parasitic capture in Cl, Mo, and Zr. Even using only the lowest-capture isotopes ^{37}Cl, ^{94}Mo, and ^{90}Zr, significant loss of neutron flux occurs at energies above 100 keV, reducing fast fissions in the system. Replacement of the fluoride salt coolant with the chloride salt NaCl–KCl–$MgCl_2$ dramatically hardens the spectrum and yields $k_\infty > 1$ in the BBMSR unit cell. In addition, low enrichment of

uranium can be used to tune the initial reactivity, while long-term burnup behaviour is fairly independent of enrichment. Enrichment in ^{37}Cl for the fuel and coolant salts is needed to avoid excessive parasitic absorption, but enrichment in ^{94}Mo can be avoided by exploring alternative cladding materials, and the chloride coolant composition does not contain Zr.

The high fuel loading and hard spectrum required for B&B operation are achieved using 100% UCl_3 fuel and NaCl–KCl–$MgCl_2$ coolant in a high fuel volume fraction configuration. The properties of the selected fuel and coolant salts are described, and uncertainties in the available data are discussed. Candidate cladding materials are discussed with respect to resistance to corrosion, irradiation, and high temperature. In addition to molybdenum, 310-type stainless steel and silicon carbide are identified for further neutronic analysis.

6.2 Fuel Convection Analysis

Tailored modelling methods are needed to efficiently analyse natural convection in heat-generating fluids. An analytical solution is derived to provide a starting point for more detailed analysis, but it requires a number of simplifications and represents an idealised system without instabilities. By adding an internal wall that divides the fuel element into two concentric sections, the flow regime is altered such that each section experiences mixed convection conditions. Comparison of existing correlations to the actual flow regime in each section shows that turbulent forced convection correlations can provide an adequately conservative estimate of heat transfer in the outer annulus section. However, existing correlations are either too liberal for the inner channel section, potentially overestimating heat transfer, or overly conservative, which would constrain the fuel design excessively.

A new heat transfer correlation is developed, based on the inner channel section, but it is general enough to be applied beyond this thesis also. The CFD package OpenFOAM is used to simulate ascending mixed convection of a heat-generating molten salt over a range of tube diameters and boundary conditions. A new non-dimensional parameter, the IHG-flux number Ω, is defined to describe the system's heat transfer behaviour by relating IHG to the wall heat flux. The Ω values of the CFD-simulated cases are used to identify heat transfer regimes and correlate Nu in the MHT regime. The MHT correlation fits the simulated results with $R^2 = 0.93$, reflecting the distinct trend.

In the MHT regime (Regime I) for small values of Ω, convection and conduction both contribute significantly to removal of the heat gained by IHG, resulting in a radial temperature profile with $T_m > T_w$. In the unstable regime (Regime II) for intermediate values of Ω, the flow is destabilised by an inflection point in the velocity profile, so heat transfer performance

is highly variable. In the insulated regime (Regime III) with large values of Ω, radial conduction at the wall is negligible compared to axial conduction, and the no-slip condition at the wall results in an inverted temperature profile with $T_w > T_m$.

6.3 Thermal–Hydraulic Fuel Modelling

A finite-difference model is developed to model the mixed convection flow of fuel in the inner and outer concentric sections of the BBMSR fuel concept. The MHT correlation based on CFD results is incorporated into the FDM to model heat transfer in the inner channel section. Heat transfer and pressure drop correlations are used to balance energy and momentum terms for each node in the FDM. The model iteratively calculates the coupled temperature–velocity profiles until the mass flow rate converges.

The FDM is used to perform a parametric study of the fuel, showing that the value of Ω corresponds to the shape of the temperature profiles in the concentric sections of the fuel. Nu of the inner channel section flow increases with Ω according to the MHT correlation, but a practical limit of $\Omega \leq 4$ is enforced for the fuel design studies.

A program is developed to enable efficient thermal–hydraulic design of the concentric BBMSR fuel. The program incorporates the FDM to model a given fuel and coolant channel geometry, and iteratively searches for several thermal–hydraulic operational parameters within specified constraints. The program identifies the maximum fuel q''' allowed within these limits and calculates the corresponding channel power density, core temperature rise, and pumping power requirement. Additional thermal–hydraulic characteristics are modelled, including minimum fuel temperature, maximum temperature in the cladding and inner wall, and Ω. With small P/D, power densities well above the target value of 100 W/cm^3 can be achieved for the modelled configurations. Reasonable values for the other thermal–hydraulic characteristics are obtained, except for excessively low minimum fuel temperatures that may lead to fuel freezing.

The fuel performance can be improved by reversing the direction of coolant flow so that it flows from cold inlet at the top to hot outlet at the bottom. With the same inputs and constraints as for the upward flowing coolant, the maximum power densities are increased approximately 10%, and the minimum fuel temperatures are increased so that most configurations are above the melting point of the fuel salt. Values of Ω are also decreased slightly, which helps to allow larger fuel diameters within the valid range of the MHT correlation.

6.4 Neutronic & Thermal–Hydraulic Fuel Design

Fuel designs are developed for natural uranium and LEU feed fuels, satisfying B&B and thermal–hydraulic requirements. For the natural and 5% enriched cases, the design objective is to enable both B&B operation and the highest possible power density, within practical engineering limitations. For the 20% enriched case, the design objective is to maximise both fuel utilisation and power density. Thermal–hydraulic performance is assessed using the design search program, and 3D pin cell geometries are modelled neutronically to assess B&B performance.

6.4.1 Natural uranium

Using the natural uranium fuel, the neutronic effects of cladding material, reflector material, fuel diameter, fuel length, and coolant plenum length are assessed. SiC cladding yields the best neutronic performance, and while the Pb reflector is the most effective, the Zr reflector is neutronically similar and more practical for high-temperature operation. Neutronic performance improves as both fuel diameter and length increase, but the diameter is limited to 30 mm for thermal–hydraulic performance, and the fuel length is limited to 400 cm for manufacturability. A coolant plenum length of 50 cm is found to be adequate for added neutron reflection. The final natural uranium configuration with SiC cladding, Zr reflector, $D = 28$ mm, $L_{fuel} = 400$ cm, and $L_{cool} = 50$ cm allows a power density of 73 W/cm^3. Its discharge burnup is approximately 300 MWd/kg, or 30% FIMA, corresponding to $U = 300$ MWd/kgU$_{\mathrm{NAT}}$.

6.4.2 5% enriched uranium

The 5% enriched fuel has higher initial reactivity compared to the natural uranium case, so its diameter can be reduced to $D = 26$ mm, keeping all other design features the same as the natural uranium case, which allows a power density of 86 W/cm^3. It achieves a discharge burnup of approximately 300 MWd/kg, yielding $U = 25.5$ MWd/kgU$_{\mathrm{NAT}}$.

The waste characteristics of the natural and 5% enriched cases are similar in terms of both discharged actinide mass and ingestion radiotoxicity. The TRU waste per unit of energy produced is relatively large due to the high breeding gain of these fuel options, while their initial radiotoxicity is slightly lower than for a typical LWR. After roughly 500 years the differences in radiotoxicity levels between fuel types become small.

Overall, the natural uranium and 5% enriched configurations perform similarly in terms of power density and waste characteristics, which are also comparable to typical LWR performance. However, the natural uranium version achieves nearly an order of magnitude larger uranium utilisation than the 5% enriched version, which itself is significantly larger than that of the LWR fuel cycle. An LWR with fuel management optimised for uranium utilisation can achieve $U_{max} = 7.15$ MWd/kgU$_{\mathrm{NAT}}$ for $n = \infty$, or $U_3 = 5.5$ MWd/kgU$_{\mathrm{NAT}}$ for $n = 3$.

6.4.3 20% enriched uranium

Using 20% enriched fuel removes the minimum burnup requirement, so a wider range of fuel geometries and resulting power densities can be considered. The candidate configurations display a clear inverse relationship between power density and burnup potential. Several configurations with relatively large D and L_{fuel} can achieve power densities of 130–150 W/cm^3 with $U_{max} = 9$–12 MWd/kgU$_{\mathrm{NAT}}$ and $U_3 = 6$–8 MWd/kgU$_{\mathrm{NAT}}$. Using 20% enriched fuel, moderate uranium utilisation improvements are possible with power densities significantly higher than 100 W/cm^3. This analysis illustrates the flexibility of the BBMSR to satisfy different fuel cycle objectives.

A representative 20% enriched fuel configuration is selected for evaluation of waste characteristics, showing moderate reduction in discharged actinides compared with the lower enriched BBMSR fuels, but higher initial radiotoxicity, similar to a typical LWR.

6.5 Recommendations for Future Work

Feasibility studies and exploratory analyses on a limited set of design options have been performed to demonstrate possible modes of operation of the BBMSR. In the next design stages, additional design options could be considered, such as an inverted fuel design to enable higher fuel volume fractions while satisfying cooling requirements. More detailed models should be developed to reduce simplifications and uncertainties, and to quantify phenomena that cannot be adequately captured in pin cell models.

6.5.1 Improved modelling methods

More advanced modelling methods are needed to reduce simplifications and uncertainties. Whereas neutronic and thermal–hydraulic analyses are only loosely coupled in the present work, fully coupled multi-physics models could be used to characterise the fission power

distribution in the homogeneous fuel mixture, and to investigate the effects of axially varying fuel thermal expansion on neutronic performance. Transient thermal–hydraulic analysis may be necessary to model the melting and freezing of the salt when fresh fuel is inserted and spent fuel is removed, and to determine the time to establish natural circulation in the fuel.

In the present thermal–hydraulic design scoping, the fuel diameter and power are significantly limited by the requirement of $\Omega \leq 4.0$, since at higher values the flow becomes unstable and cannot be quantitatively characterised using the current method. Further studies may enable additional heat transfer correlations to be developed for $\Omega > 4.0$, or full CFD simulations of the concentric fuel could be performed to calculate heat transfer from the fuel with larger diameters and optimal ε. This could expand the design space to allow better fuel economy and higher power density. Eventually, experimental validation will be needed to confirm the heat transfer performance modelled in CFD and using the FDM.

6.5.2 Full-core modelling

Assembly- and core-level neutronic calculations are needed to represent the heterogeneous arrangement of partially burned fissile assemblies and fresh fertile assemblies. An appropriate fuel management scheme must be determined to sustain criticality and to achieve an optimal balance of fuel utilisation and economic reactor operation. The effects of fuel shuffling and power peaking are particularly important in a B&B reactor due to the highly nonlinear reactivity–burnup behaviour. Because of convective mixing in the fuel tube, the axial burnup will be homogeneous, which will produce a different axial power and leakage profile compared to conventional reactors. The advantages and disadvantages of this behaviour must be identified, and innovative fuel shuffling may be needed.

The Doppler coefficient, fuel thermal expansion reactivity coefficient, and coolant temperature reactivity coefficient should be calculated to determine how much additional reactivity control is needed for steady-state operation, transients, and off-normal conditions. Doppler and fuel temperature coefficients are expected to be strongly negative, which will offset a positive contribution from the coolant temperature coefficient. Generation IV reactors are required to ensure robust decay heat removal without external power input [46], so natural circulation of the coolant should be modelled to evaluate whether the tight lattice of the BBMSR allows passive cooling in case of a loss-of-flow accident.

The radial power distribution in the core must be determined and may need to be adjusted such that the heat can be removed effectively. Since fresh fertile assemblies at the periphery will naturally produce low power, it may be possible use larger diameter fuel elements

in these regions to improve breeding and reduce radial leakage. As the fuel accumulates fissile material and is shuffled inwards, it could be transferred to smaller diameter cladding compatible with the higher power density of the inner zone. Design of the power conversion side of the plant is needed to calculate overall power output and thermal efficiency.

6.5.3 Alternative design options

Further work including property characterisation is needed to identify the most feasible combination of isotope enrichment, cladding material, and UCl_3 concentration in the fuel salt. The neutronic analysis in Chapter 2 found that 100% UCl_3 fuel and 50-30-20% NaCl–KCl–$MgCl_2$ coolant make B&B operation possible, but a small concentration of carrier salt in the fuel and alternative coolant compositions could still be explored.

Alternative fuel arrangements may also be explored if necessary to meet the cooling requirements of a B&B configuration. For example, an inverted fuel assembly can be used to maximise the fuel volume fraction. In a tube-in-duct assembly, fuel is contained in a hexagonal duct that allows coolant flow through internal tubes [25]. However, these fuel concepts are designed for solid fuel, so their applicability to a molten salt fuel must be evaluated, and significant modelling effort will be required to model fuel natural convection in these configurations.

6.5.4 Materials considerations

As discussed in Chapter 2, there are many uncertainties and gaps in the current databases of chloride salt properties. Accuracy of the thermal–hydraulic analyses presented in this work would be greatly improved by more reliable thermophysical data. The thermal–hydraulic tools have been developed so that properties and constraints can be updated, and new calculations can be produced relatively easily when new data becomes available.

The cladding and inner wall thickness have been assumed based on specifications from other reactors, but the actual thickness requirement will depend on numerous factors unique to the BBMSR fuel design. Similarly, the maximum temperature limit of the cladding and inner wall must be determined specifically based on the corrosion and irradiation conditions in the BBMSR. Quantifying these requirements may significantly affect the neutronic and thermal–hydraulic performance of the fuel.

An important feature of the BBMSR concept is the ease of replacement of cladding, which allows high fuel burnup and reduces the importance of long-term resistance to corrosion, irradiation, and heat damage. However, frequent cladding replacement may incur high

economic costs, so the cladding lifetime should be estimated based on the fuel residence time and accumulation of DPA in the material. The overall fuel and cladding cost as well as frequency of maintenance outages required for cladding replacement should remain competitive with other reactor designs.

References

[1] Aicher, T. and Martin, H. (1997). New correlations for mixed turbulent natural and forced convection heat transfer in vertical tubes. *International Journal of Heat and Mass Transfer*, 40(15):3617–3626.

[2] Andreades, C., Cisneros, A. T., Choi, J. K., Chong, A. Y. K., Fratoni, M., Hong, S., Huddar, L. R., Huff, K. D., Krumwiede, D. L., Laufer, M. R., Munk, M., Scarlat, R. O., Sweibaum, N., Greenspan, E., and Peterson, P. F. (2014). Mark-1 PB-FHR Technical Description Technical Description of the "Mark 1" Pebble-Bed Fluoride-Salt-Cooled High-Temperature Reactor (PB-FHR) Power Plant. Technical report, Department of Nuclear Engineering, University of California, Berkeley.

[3] ANSWERS (2015). WIMS: A Modular Scheme for Neutronics Calculations - User Guide for Version 10. Amec Foster Wheeler.

[4] Bejan, A. (1995). *Convection Heat Transfer*. Wiley, New York, second edition.

[5] Beneš, O. and Konings, R. J. M. (2008). Thermodynamic evaluation of the NaCl-$MgCl_2$-UCl_3-$PuCl_3$ system. *Journal of Nuclear Materials*, 375:202–208.

[6] Bettis, E. S., Schroeder, R. W., Cristy, G. A., Savage, H. W., Affel, R. G., and Hemphill, L. F. (1957). The Aircraft Reactor Experiment-Design and Construction. *Nuclear Science and Engineering*, 2:804–825.

[7] Buongiorno, J., Corradini, M., John, P., and Petti, D. (2018). The Future of Nuclear Energy in a Carbon-Constrained World. *MIT Energy Initiative*, page 275.

[8] Desyatnik, V., Katyshev, S., Raspopin, S., and Chervinskii, Y. F. (1975). Density, Surface Tension, and Viscosity of Uranium Trichloride-Sodium Chloride Melts. *Atomnya Energiya*, 39(1):70–72.

[9] Driscoll, M. J., Downar, T. J., and Pilat, E. E. (1990). *The Linear Reactivity Model for Nuclear Fuel Management*. American Nuclear Society.

[10] Ellis, T., Petroski, R., Hejzlar, P., Zimmerman, G., McAlees, D., Whitmer, C., Hejzlar, J., Weaver, K., Walter, J. C., McWhirter, J., Ahlfeld, C., Burke, T., Hyde, R., Gilleland, J., Ishikawa, Y., Wood, L., Myhrvold, N., and Gates, W. H. (2010). Traveling-Wave Reactors: A Truly Sustainable and Full-Scale Resource for Global Energy Needs. In *Proceedings of ICAPP 2010*.

[11] Engel, J., Bauman, H., Dearing, J., Grimes, W., McCoy, E., and Rhoades, W. (1980). Conceptual Design Characteristics of a Denatured Molten-Salt Reactor with Once-Through Fuelling. Technical report, Oak Ridge National Laboratory, Oak Ridge, Tennessee.

[12] Feinberg, S. M. (1958). Discussion comment. In *International Conference on the Peaceful Uses for Atomic Energy*, Geneva, Switzerland.

[13] Fiorina, C., Aufiero, M., Cammi, A., Franceschini, F., Krepel, J., Luzzi, L., Mikityuk, K., and Ricotti, M. E. (2013). Investigation of the MSFR core physics and fuel cycle characteristics. *Progress in Nuclear Energy*, 68:153–168.

[14] Foraboschi, F. P. and Di Federico, I. (1964). Heat transfer in laminar flow of non-newtonian heat-generating fluids. *International Journal of Heat and Mass Transfer*, 7:315–325.

[15] Forsberg, C. and Peterson, P. F. (2016). Basis for Fluoride Salt–Cooled High-Temperature Reactors with Nuclear Air-Brayton Combined Cycles and Firebrick Resistance-Heated Energy Storage. *Nuclear Technology*, 196(1):13–33.

[16] Forsberg, C., Peterson, P. F., Hu, L.-W., and Sridharan, K. (2015). Baseload nuclear with variable electricity to the grid. *Nuclear News*, 58:77–81.

[17] Forsberg, C. W., Hu, L.-W., Peterson, P. F., and Sridharan, K. (2014). Fluoride-Salt-Cooled High-Temperature Reactors for Power and Process Heat. *MIT Advanced Nuclear Power Report Series*.

[18] George, N. M., Terrani, K., Powers, J., Worrall, A., and Maldonado, I. (2015). Neutronic analysis of candidate accident-tolerant cladding concepts in pressurized water reactors. *Annals of Nuclear Energy*, 75:703–712.

[19] Greenspan, E. (2012). A phased development of breed-and-burn reactors for enhanced nuclear energy sustainability. *Sustainability*, 4:2745–2764.

[20] Gregg, L. (2018). *Design of a Molten Chloride Fast Spectrum Reactor*. Master's thesis, University of California, Berkeley.

[21] Handwerk, C. S. (2007). *Optimized Core Design of a Supercritical Carbon Dioxide-Cooled Fast Reactor*. PhD Thesis, Massachusetts Institute of Technology.

[22] Heidet, F. (2010). *Maximum Fuel Utilization in Advanced Fast Reactors without Actinides Separation*. PhD Thesis, University of California, Berkeley.

[23] Heidet, F. and Greenspan, E. (2012a). Feasibility of lead cooled breed and burn reactors. *Progress in Nuclear Energy*, 54:75–80.

[24] Heidet, F. and Greenspan, E. (2012b). Neutron Balance Analysis for Sustainability of Breed-and-Burn Reactors. *Nuclear Science and Engineering*, 171:13–31.

[25] Hejzlar, P., Todreas, N. E., Shwageraus, E., Nikiforova, A., Petroski, R., and Driscoll, M. J. (2009). Cross-comparison of fast reactor concepts with various coolants. *Nuclear Engineering and Design*, 239:2672–2691.

[26] Hombourger, B., Krepel, J., Mikityuk, K., and Pautz, A. (2017). On the Feasibility of Breed-and-Burn Fuel Cycles in Molten Salt Reactors. In *International Conference on Fast Reactors and Related Fuel Cycles: Next Generation Nuclear Systems for Sustainable Development*, Yekaterinburg, Russian Federation.

[27] IAEA (2006). Fast Reactor Database 2006 Update. IAEA-TECDOC-1531, International Atomic Energy Agency, Vienna, Austria.

[28] IAEA (2011). Evaluated Nuclear Data File (ENDF). https://www-nds.iaea.org/exfor/endf.htm.

[29] International Molybdenum Association (2013). Molybdenum properties. https://www.imoa.info/molybdenum/molybdenum-properties.php.

[30] Jackson, J., Cotton, M., and Axcell, B. (1989). Studies of mixed convection in vertical tubes. *International Journal of Heat and Fluid Flow*, 10(1):2–15.

[31] Jensen, S. E. and Olgaard, P. L. (1995). Description of the Prototype Fast Reactor at Dounreay. Technical report, Riso National Laboratory, Roskilde, Denmark.

[32] Jeong, Y. S., Seo, S. B., and Bang, I. C. (2018). Natural convection heat transfer characteristics of molten salt with internal heat generation. *International Journal of Thermal Sciences*, 129:181–192.

[33] Joshi, M. V., Gaitonde, U. N., and Mitra, S. K. (2006). Analytical Study of Natural Convection in a Cavity With Volumetric Heat Generation. *Journal of Heat Transfer*, 128:176–182.

[34] Judd, A. M. (2014). *An Introduction to the Engineering of Fast Nuclear Reactors*. Cambridge University Press, New York.

[35] Kazimi, M., Moniz, E. J., and Forsberg, C. W. (2011). The Future of the Nuclear Fuel Cycle. Technical report, Massachusetts Institute of Technology.

[36] Korpela, S. A., Lee, Y., and Drummond, J. E. (1982). Heat Transfer Through a Double Pane Window. *Journal of Heat Transfer*, 104:539–544.

[37] Krepel, J., Hombourger, B., Fiorina, C., Mikityuk, K., Rohde, U., Kliem, S., and Pautz, A. (2014). Fuel cycle advantages and dynamics features of liquid fueled MSR. *Annals of Nuclear Energy*, 64:380–397.

[38] Leefe, S., Jackson-Laver, P., and Scott, I. R. (2015). Computation Fluid Dynamic Modelling of Natural Convection Heat Flow in Unpumped Molten Salt Fuel Tubes. In *Proceedings of the Thorium Energy Conference*, Mumbai, India.

[39] Leppänen, J. (2015). Serpent – a Continuous-energy Monte Carlo Reactor Physics Burnup Calculation Code. VTT Technical Research Centre of Finland.

[40] Lindley, B. A., Fiorina, C., Franceschini, F., Lahoda, E. J., and Parks, G. T. (2014). Thorium breeder and burner fuel cycles in reduced-moderation LWRs compared to fast reactors. *Progress in Nuclear Energy*, 77:107–123.

[41] Martin, B. (1967). Free convection in a vertical cylinder with internal heat generation. *Proceedings of the Royal Society of London*, 301:327–341.

[42] Martin, M., Aufiero, M., Greenspan, E., and Fratoni, M. (2017). Feasibility of a Breed-and-Burn Molten Salt Reactor. In *Transactions of the American Nuclear Society*, volume 116, pages 1174–1176, San Francisco, CA.

[43] Melnik, Y. P., Pilipenko, V. V., Fomin, A. S., Fomin, S. P., and Shulga, N. F. (2009). Study of a self-regulated nuclear burn wave regime in a fast reactor based on a thorium-uranium cycle. *Atomic Energy*, 107(5):352–359.

[44] Moltex Energy (2018). An Introduction to the Moltex Energy Technology Portfolio. Technical report, Moltex Energy.

[45] OECD Nuclear Energy Agency (2011). Potential Benefits and Impacts of Advanced Nuclear Fuel Cycles with Actinide Partitioning and Transmutation. Technical report, Organisation for Economic Cooperation and Development, Paris, France.

[46] OECD Nuclear Energy Agency (2014a). Technology Roadmap Update for Generation IV Nuclear Energy Systems. Technical report, Organisation for Economic Cooperation and Development, Paris, France.

[47] OECD Nuclear Energy Agency (2014b). Uranium 2014: Resources, Production and Demand (Red Book). Technical report, Organisation for Economic Cooperation and Development, Paris, France.

[48] Ottewitte, E. H. (1982). *Configuration of a Molten Chloride Fast Reactor on a Thorium Fuel Cycle to Current Nuclear Fuel Cycle Concerns*. PhD Thesis, University of California Los Angeles.

[49] Perry, A. and Bauman, H. (1970). Reactor physics and fuel-cycle analysis. *Nuclear Applications & Technology*, 8:208–219.

[50] Petroski, R., Forget, B., and Forsberg, C. (2012). Neutronic characteristics of linear-assembly breed-and-burn reactors. *Nuclear Engineering and Design*, 250:364–384.

[51] Petroski, R., Forget, B., and Forsberg, C. (2013). Evaluation of core compositions for use in breed and burn reactors and limited-separations fuel cycles. *Annals of Nuclear Energy*, 55:151–168.

[52] Petroski, R., Hejzlar, P., and Todreas, N. E. (2009). Thermal hydraulic design of a liquid salt-cooled flexible conversion ratio fast reactor. *Nuclear Engineering and Design*, 239:2612–2625.

[53] Petroski, R. C. (2011). *General Analysis of Breed-and-Burn Reactors and Limited-Separations Fuel Cycles*. PhD Thesis, Massachusetts Institute of Technology.

[54] Pini, A., Cammi, A., Cauzzi, M., Fanale, F., and Luzzi, L. (2016). An Experimental Facility to Investigate the Natural Circulation Dynamics in Presence of Distributed Heat Sources. *Energy Procedia*, 101:10–17.

[55] Powney, D. J. and Newton, T. D. (2004). Overview of The WIMS 9 Resonance Treatment. SERCO.

[56] Richard, J. (2012). *Design Optimization and Analysis of a Fluoride Salt Cooled High Temperature Test Reactor for Accelerated Fuels and Materials Testing and Nonproliferation and Safeguards Evaluations*. PhD Thesis, Massachusetts Institute of Technology.

[57] Rouch, H., Geoffroy, O., Rubiolo, P., Laureau, A., Brovchenko, M., Heuer, D., and Merle-Lucotte, E. (2014). Preliminary thermal–hydraulic core design of the Molten Salt Fast Reactor (MSFR). *Annals of Nuclear Energy*, 64:449–456.

[58] Schlichting, H. and Gersten, K. (2000). *Boundary-Layer Theory*. Springer, Berlin, eighth edition.

[59] Scott, I. (2015). Gaseous and Volatile Fission Produce Release From Molten Salt Nuclear Fuel. In *Proceedings of the Thorium Energy Conference*, Mumbai, India.

[60] Scott, I. (2017a). Stable salt fast reactor. In *Molten Salt Reactors and Thorium Energy*, pages 571–580. Elsevier.

[61] Scott, I. (2017b). Static liquid fuel reactors. In *Molten Salt Reactors and Thorium Energy*, pages 475–494. Elsevier.

[62] Scott, I., Abram, T., and Negri, O. (2015). Stable Salt Reactor Design Concept. In *Proceedings of the Thorium Energy Conference*, Mumbai, India.

[63] Sehgai, B. R., Dinh, T. N., and Nourgaliev, R. R. (1996). Analysis of Natural Convection in Volumetrically-heated Melt Pools. Technical report, Swedish Nuclear Power Inspectorate and US Nuclear Regulatory Commission, Stockholm, Sweden.

[64] Sekimoto, H., Ryu, K., and Yoshimura, Y. (2001). CANDLE: The New Burnup Strategy. *Nuclear Science and Engineering*, 139:306–317.

[65] Serp, J., Allibert, M., Beneš, O., Delpech, S., Feynberg, O., Ghetta, V., Heuer, D., Holcomb, D., Ignatiev, V., Kloosterman, J. L., Luzzi, L., Merle-Lucotte, E., Uhlíř, J., Yoshioka, R., and Zhimin, D. (2014). The molten salt reactor (MSR) in generation IV: Overview and perspectives. *Progress in Nuclear Energy*, 77:308–319.

[66] Shwageraus, E., Hejzlar, P., and Driscoll, M. J. (2009). Liquid salt cooled flexible conversion ratio fast reactor: Neutronic design. *Nuclear Engineering and Design*, 239:2626–2645.

[67] Siahpush, A. and Crepeau, J. (2011). Scale Analysis of Convective Melting with Internal Heat Generation. In *Proceedings of the ASME/JSME 2011 8th Thermal Engineering Joint Conference*, Honolulu, HI. ASME.

[68] Snead, L. L., Nozawa, T., Katoh, Y., Byun, T.-S., Kondo, S., and Petti, D. A. (2007). Handbook of SiC properties for fuel performance modeling. *Journal of Nuclear Materials*, 371:329–377.

[69] Taube, M. and Ligou, J. (1974). Molten plutonium chlorides fast breeder reactor cooled by molten uranium chloride. *Annals of Nuclear Science and Engineering*, 1:277–281.

[70] TerraPower (2016). MCFR Solutions: Nuclear Innovation for New Options in American Industry. http://terrapower.com/technologies/mcfr.

[71] The Economic Modeling Working Group Of the Generation IV International Forum (2007). Cost Estimating Guidelines for Generation IV Nuclear Energy Systems. Technical report, Organisation for Economic Cooperation and Development.

[72] The OpenFOAM Foundation (2017). OpenFOAM v5 User Guide.

[73] Thoma, R. E. (1959). Phase diagrams of nuclear reactor materials. Technical report, Oak Ridge National Laboratory, Oak Ridge, Tennessee.

[74] Thyssenkrupp Materials (2017). Stainless Steel 310 - 1.4845 Material Data Sheet. https://www.thyssenkrupp-materials.co.uk/media/material_data_sheets/stainless_steel_1/stainless_steel_1-4845.pdf.

[75] Todreas, N. E. (2009). Thermal-Hydraulic Challenges in Fast Reactor Design. *Nuclear Technology*, 167:127–144.

[76] Todreas, N. E., Hejzlar, P., Nikiforova, A., Petroski, R., Shwageraus, E., Fong, C. J., Driscoll, M. J., Elliott, M. A., and Apostolakis, G. (2009). Flexible conversion ratio fast reactors: Overview. *Nuclear Engineering and Design*, 239:2582–2595.

[77] Todreas, N. E. and Kazimi, M. S. (1990). *Nuclear Systems Volume I: Thermal Hydraulic Fundamentals*. Taylor & Francis.

[78] Vitillo, F., Todreas, N. E., and Driscoll, M. J. (2011). A Vented Inverted Fuel Assembly Design for an SFR. Technical report, Center for Advanced Nuclear Energy Systems at MIT.

[79] Xing, Z. and Shwageraus, E. (2017). Design Space Exploration Studies of an FHR Concept Leveraging AGR Technologies. In *Proceedings of ICAPP 2017*, Fukui and Kyoto, Japan.

[80] Xu, Z. (2003). *Design Strategies for Optimizing High Burnup Fuel in Pressurized Water Reactors*. PhD Thesis, Massachusetts Institute of Technology.

[81] Xu, Z., Driscoll, M. J., and Kazimi, M. S. (2002). Neutron Spectrum Effects on Burnup, Reactivity, and Isotopics in UO_2/H_2O Lattices. *Nuclear Science and Engineering*, 141:175–189.

[82] Yarsky, P. (2005). *Core Design and Reactor Physics of a Breed and Burn Gas-Cooled Fast Reactor*. PhD Thesis, Massachusetts Institute of Technology.

[83] Yueh, K. and Terrani, K. A. (2014). Silicon carbide composite for light water reactor fuel assembly applications. *Journal of Nuclear Materials*, 448:380–388.

[84] Zentner, M., Coles, G., and Talbert, R. (2005). Nuclear Proliferation Technology Trends Analysis. Technical report, Pacific Northwest National Laboratory.

[85] Zhang, L., Luo, S., Zhang, Y., Tian, W., Su, G., and Qiu, S. (2018). Large eddy simulation on turbulent heat transfer in reactor vessel lower head corium pools. *Annals of Nuclear Energy*, 111:293–302.

Appendix A

OpenFOAM input

Table A.1 lists the *p_rgh*, T, and U boundary and initial conditions for the fuel inner channel model. The *p_rgh* term is referred to in OpenFOAM documentation as the "pseudo-hydrostatic pressure," since it is equivalent to the static pressure p minus the hydrostatic pressure $\rho \cdot g \cdot h$ [72]. Case-specific boundary conditions are provided for *p_rgh*, while p is simply calculated by adding the hydrostatic term to *p_rgh*. Pressure is relative in the simulation of an incompressible fluid, so the atmospheric pressure can be defined arbitrarily and here the *p_rgh* outlet (open to the atmosphere) is fixed at 0. In a simple pipe flow case without buoyancy, the floor and walls would be assigned the *zeroGradient* condition; *fixedFluxPressure* replaces *zeroGradient* to adjust the gradient in situations where body forces such as gravity are present [72].

T_{in} from the FDM is the fixed, uniform inlet temperature condition, and zero gradient at the outlet corresponds to an adiabatic condition. The fixed, uniform q''_{wall} along the walls is defined using the pre-built OpenFOAM boundary condition *externalWallHeatFluxTemperature*, which supplies a heat flux condition for temperature on an external wall. (q''_{wall} is given in units of W/m^2, and its sign is negative for heat lost from the domain.) *externalWallHeatFluxTemperature* uses the fuel thermal conductivity κ, a defined constant.

The velocity boundary conditions used for the fuel inner channel model follow the standard settings for a typical pipe flow, with a fixed and uniform inlet velocity, zero gradient outlet, and no-slip (zero velocity) walls. The internal field initially has zero velocity, and the steady-state velocity profile develops according to the inlet velocity and other model conditions, including the buoyancy effect.

Table A.1 Boundary & initial conditions

	Pressure, p_rgh	Temperature, T	Velocity, U
Inlet	fixedFluxPressure: uniform 0	fixedValue: uniform T_{in} [K]	fixedValue: uniform (0 0 v_{in})
Outlet	fixedValue: uniform 0	zeroGradient	zeroGradient
Walls	fixedFluxPressure: uniform 0	externalWallHeatFluxTemperature: uniform q''_{wall}	fixedValue: uniform (0 0 0)
Internal Field	uniform 0	uniform T_{in} [K]	uniform (0 0 0)

Algorithm

The buoyantBoussinesqPimpleFoam solver employs the transient algorithm PIMPLE, which merges the steady-state algorithm SIMPLE and the explicit transient algorithm PISO. The result is a semi-implicit algorithm that iterates over the equations to find the steady-state solution for each time step. Whereas PISO requires a Courant number (Co) less than one to maintain stability, PIMPLE allows $Co > 1$ so that longer time steps can be used to achieve faster convergence without loss of stability. However, $Co = 0.9$ has been conservatively used in this study.

For the fuel inner channel simulation, convergence is further encouraged by running the first half of the simulation with $\beta = 0$ so that buoyancy is not modelled. After the model converges to steady state for this condition, β is set to its physical value to activate buoyancy for the second stage of the simulation. To detect steady state with the transient solver, the results were viewed at consecutive time steps as the solution progressed to see when it converged. 50 seconds was found to be sufficient for convergence in each stage of the simulation, without and then with buoyancy. All buoyant-IHG inner fuel channel results reported in Chapter 3 have been obtained at the end of the second stage, at 100 seconds.

***fvSolutions* dictionary file:**

```
solvers
{
    p_rgh
    {
        solver          PCG;
        preconditioner  DIC;
        tolerance       1e-7;
        relTol          0.01;
    }

    p_rghFinal
    {
        $p_rgh;
        relTol          0;
    }

    "(U|T)"
    {
        solver          PBiCGStab;
        preconditioner  DILU;
        tolerance       1e-7;
        relTol          0.001;
    }

    "(U|T)Final"
    {
        $U;
        relTol          0;
    }
}


PIMPLE
{
```

```
    momentumPredictor on;
    nOuterCorrectors 1;
    nCorrectors     2;
    nNonOrthogonalCorrectors 0;
    pRefCell        0;
    pRefValue       0;
}

relaxationFactors
{
    equations
    {
        "(U|T|k|epsilon|R)" 1;
        "(U|T|k|epsilon|R)Final" 1;
    }
}
```

***fvSchemes* dictionary file:**

```
ddtSchemes
{
    default         Euler;
}

gradSchemes
{
    default         Gauss linear;
}

divSchemes
{
    default         none;

    div(phi,U)      Gauss limitedLinear 1;
    div(phi,T)      Gauss limitedLinear 1;
    div((nuEff*dev2(T(grad(U))))) Gauss linear;
}

laplacianSchemes
{
    default         Gauss linear corrected;
}

interpolationSchemes
{
    default         linear;
}

snGradSchemes
{
    default         corrected;
}
```

Appendix B

Coolant channel equations

Coolant velocity:

Given a fixed pressure drop limit $\Delta p_{channel}$ and variable combination fuel diameter D, length L, and pin pitch P, a coolant inlet velocity can be determined.

Hexagonal channel coolant flow area, A_{hex}:

$$A_{hex} = 2\sqrt{3}P^2 - \frac{\pi}{4}D^2 \tag{B.1}$$

Subchannel equivalent hydraulic diameter, D_e:

$$D_e = \frac{4A_{hex}}{\pi D} \tag{B.2}$$

Coolant Reynolds number, Re_m:

$$Re_m = \frac{G_m D_e}{\mu_m} \tag{B.3}$$

where G_m is the coolant mass flow rate per unit area. Coolant friction factor, f_m:

$$f_m = 0.184\,(Re_m)^{-0.2} \tag{B.4}$$

Channel pressure drop:

$$\Delta p_{channel} = \frac{f_m G_m^2 L}{2D_e \rho_m} \tag{B.5}$$

All variables in Equation B.5 are known except for f_m and G_m, which must be found for the given combination of P and D. Combining and rearranging Equations B.3–B.5,

$$f_m G_m^2 = 0.184 \left(\frac{G_m D_e}{\mu_m} \right)^{-0.2} G_m^2 \tag{B.6}$$

$$G_m = \left[\frac{f_m G_m^2}{0.184} \left(\frac{\mu_m}{D_e} \right)^{-0.2} \right]^{1/1.8} \tag{B.7}$$

The coolant velocity and mass flow rate can then be determined:

$$v_m = \frac{G_m}{\rho_m} \tag{B.8}$$

$$\dot{m}_m = G_m A_{hex} \tag{B.9}$$

Most realistic channel configurations will have turbulent coolant flow ($Re_m > 2300$), so the Dittus-Boelter correlation is used to find the coolant Nusselt number Nu_m and heat transfer coefficient h_m:

$$Nu_m = 0.023 \, Re_m^{0.8} Pr_m^{0.4} \tag{B.10}$$

$$h_m = \frac{Nu_m \kappa_m}{D_e} \tag{B.11}$$

Coolant and cladding temperatures:

Average volumetric power density is converted to linear heat rate, q':

$$q' = q''' \cdot \frac{\pi}{4} D^2 \tag{B.12}$$

Bulk coolant temperature T_m as a function of z:

$$T_m(z) = T_{in} + \frac{q'}{\dot{m}_m c_{P,m}} \frac{L_e}{\pi} \left(\sin \frac{\pi z}{L_e} + \sin \frac{\pi L}{2L_e} \right) \tag{B.13}$$

Outer cladding temperature, $T_{co}(z)$, with outer cladding radius r_{co}:

$$T_{co}(z) = T_m(z) + \frac{1}{2\pi r_{co} h_m} \cdot q' \cos \frac{\pi z}{L_e} \tag{B.14}$$

Inner cladding temperature, $T_{ci}(z)$, with inner cladding surface r_{ci}:

$$T_{ci}(z) = T_{co}(z) + \frac{1}{2\pi\kappa_{clad}} \ln\left(\frac{r_{co}}{r_{ci}}\right) \cdot q' \cos\frac{\pi z}{L_e} \tag{B.15}$$

The axial temperature profiles are discretised according to the number of nodes N used, and the discretised T_{ci} is used as input to the FDM to solve for temperatures within the fuel.